UNIVERSITÀ DEL SALENTO

FACOLTÀ DI SCIENZE MM. FF. NN.

DOTTORATO DI RICERCA IN FISICA - XX CICLO

IMPLEMENTATION AND PERFORMANCE OF THE MUON EVENT FILTER OF THE ATLAS EXPERIMENT

Candidato:
Dott. Giovanni SIRAGUSA

Coordinatore:
Prof. Gilberto LEGGIERI

Tutore:
Dott.ssa Stefania SPAGNOLO

Co-tutore:
Dott. Andrea VENTURA

Alla mia famiglia.

Ringraziamenti

La ricerca descritta in questa tesi è stata l'occasione di un'esperienza scientifica e umana intensa e gratificante. Di questo devo ringraziare le persone che, in questi tre anni, mi hanno seguito, spronato e dato fiducia, i professori e ricercatori dell'Università del Salento e della sez. INFN di Lecce, con i quali ho avuto modo di confrontarmi e collaborare, tutti i miei colleghi, con i quali ho condiviso fruttuose discussioni e piacevoli giornate.

Innanzitutto ringrazio i miei tutori, la Dott.ssa Stefania Spagnolo e il Dott. Andrea Ventura, per la dedizione con cui, giorno per giorno, mi hanno guidato, andando ben al di là del loro impegno di tutoraggio. Il tempo e la pazienza che mi hanno dedicato e il bagaglio di conoscenze che mi hanno trasmesso sono un patrimonio che spero di aver meritato almeno in parte. A loro va tutta la mia riconoscenza e la mia stima.

Un ringraziamento speciale va alla Dott.ssa Margherita Primavera per il suo supporto e la sua fiducia, per aver seguito con attenzione il mio lavoro e la mia formazione e per la generosità con cui guida il nostro gruppo di ricerca.

Voglio poi ringraziare i responsabili della sez. INFN di Lecce per avermi consentito di perfezionare la mia ricerca presso i laboratori del CERN. In particolare il Dott. Franco Grancagnolo per i suoi preziosi consigli e la stima che mi ha voluto dimostrare e il Professor Edoardo Gorini per l'attenzione che ha sempre dimostrato verso di me e le altre "giovani leve" del nostro gruppo.

Ancora vorrei ringraziare la Dott.ssa Gabriella Cataldi per avermi aiutato a districare ingarbugliati problemi di software, il Dott. Gabriele Chiodini per avermi introdotto al lavoro hardware sugli RPC e tutti i colleghi del *Muon Slice Working Group* per la loro proficua collaborazione, che ha reso possibile il presente lavoro. Infine vorrei ringraziare i miei amici e colleghi, Iris, Sergio e Gianfranco, per essermi stati vicini ed avermi aiutato e consigliato sempre.

Contents

Introduction

First proton-proton collisions at the Large Hadron Collider (LHC) are expected by the next summer. It will be an exciting moment for all the physicists involved in the accelerator and detector design and construction, and for the whole High Energy Physics community, which is waiting important answers to the open questions of the Standard Model from the LHC data. During last three years, the ATLAS detector, located at one interaction point of the LHC, has been installed in its experimental cavern and all sub-systems are reaching the final operating configuration through an extensive process of commissioning. At present, all the sub-detectors are able to record cosmic data and several combined cosmic runs have been performed, demonstrating the overall functionality.

Trigger is a big challenge at the LHC, where the high luminosity and the large proton-proton total cross section determine an unprecedented event rate ($\sim$1 GHz) which has to be compared with the limited data storage capability ($\sim$100 Hz). Moreover, the cross sections of interesting events are highly suppressed compared to the total cross section (by factors greater than 10^6), which results in the requirement of high selection efficiency and strong rejection power. Therefore, a three level trigger in ATLAS has been chosen to achieve this goal.The third level, the Event Filter (EF) is very

close in performance and implementation to the offline reconstruction, which produces the final event representation in terms of particles used by physics analyses.
High-p_T muons in the final states are one of the most important and clear signatures of interesting physics processes, ranging from Standard Model phenomena (e.g. EW bosons, top and B physics) to many of the theoretical new physics scenarios envisaged. Thus the proper operation of the muon selection has a strong impact on the entire LHC physics program.

This thesis illustrates how the entire muon trigger chain is implemented and how it works, with focus on the EF. In particular, after a general introduction of the physics reach of a facility exploring the sub-TeV energy scale in Chapter 1, the overall ATLAS detector concept and the expected performance are illustrated in Chapter 2. Special emphasis is dedicated to the Muon Spectrometer and to the Trigger and Data Acquisition systems. Chapter 3 reviews the muon trigger configuration in its most recent implementation, through the three Trigger levels. The last Chapter analyses in detail the muon selection performance by means of dedicated simulations in the framework of the official ATLAS data challenge. After discussing the main sources of muon rates and their uncertainty, Trigger resolutions and efficiencies for the EF algorithms are estimated from large Monte Carlo data samples over a wide range of transverse momentum. Then a study is presented for the Trigger selection of muons coming from in-flight decay of light mesons. Finally the muon Trigger rates are discussed and estimated for the three Trigger levels and different luminosity scenarios.

Chapter 1

Physics at the LHC, the Standard Model and beyond

1.1 Introduction

Four fundamental interactions, gravitational, electromagnetic, weak and strong, are enough to describe the physics at all the scales experimentally explored. All these interactions can be described in terms of gauge theories, in particular they can be derived from a general principle introduced by Weyl in 1929 [1], the *gauge principle*. Despite this common aspect, there are substantial differences between these interactions, in particular between the gravitational and the others. In any case, the gauge theory of interactions is an important step to reach a unified theory of all forces. This fundamental simplifying require has been demonstrated to be satisfied in the case of electromagnetic and weak interactions; strong interaction as well is one of the topics of grand unification theories. There exist experimental indications and compelling theoretical arguments that allow to suppose that strong interactions will fit along with the electroweak interactions in a unified theory.

Far more complex is the final step of including in a coherent overall picture gravity.

The unification principle has guided physicists to formulate the Standard Model (SM) of elementary particles, which is, at present, the best mathematical description of the interactions between matter and three of the four known forces. This theory accounts for the widest range of experimental data in the field of High Energy Physics, successfully describing them at the smallest scales (10^{-18} m) and the highest energies ($\sim$ 200 GeV) accessible to the current experiments. It has been shown only recently that the evidence of neutrino oscillations has clearly shown that the SM, in its minimal formulation (which assumes the neutrino to be massless), is not sufficient to describe data . Nevertheless, other theoretical problems affect the SM, from parameter fine tuning up to the inability to describe the gravitational force. For these reasons in the last few decades a wide range of new theories has been proposed, all of them constrained to reproduce the SM in low energy regime. These theories present interesting features and a very rich new phenomenology which is likely to be probed at the Large Hadron Collider (LHC) (Sec. 2.1.1).

1.1.1 The Standard Model

The Standard Model (SM) [2, 3, 4] is a quantum field theory which describes all matter components and forces in terms of fundamental point-like particles. These particles do carry internal angular momentum, which is characterised by the *spin* quantum number s. The matter component of the theory consists of particles which have s half integer (*fermions*), the forces between them are mediated by particles with s integer (*bosons*). The bosons are a consequence of local gauge invariance applied to the fermion fields and are a manifestation

of the group symmetry of the theory, i.e. SU(3)×SU(2)×U(1) [5, 6, 7].

In addition to the particles shown in the table 1.1, each fermion has a cor-

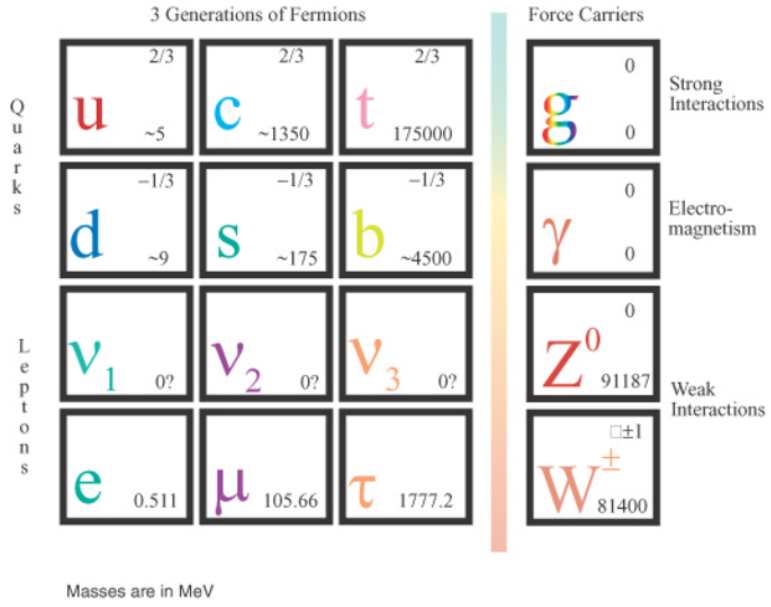

Figure 1.1. *Standard model elementary particles. Masses are reported at the bottom and charge (normalised to the absolute value of the electron charge) at the top of each box.*

responding anti-particle with same mass and spin but opposite charge. The fermions can be divided into two families, according on whether or not they interact via the strong nuclear force. Those which respond to the nuclear force are known as *quarks*, and are confined by it in more complicated objects known as *hadrons*. The other fermions, known as *leptons*, have only weak-nuclear and electromagnetic charges, and therefore can exist as free particles.

As shown in Fig. 1.1, there are three generations of fermions, each generation identical except for mass: the origin of this structure and the breaking of generational symmetry (*flavor symmetry*), is not explained in the context

of the SM. There are three leptons with electric charge -1, the electron (e), the muon (μ), the tau (τ) and three electrically neutral, the neutrinos ν_e, ν_μ and ν_τ. Similarly, three quarks have charge 2/3, up (u), charm (c) and top (t), and three have charge $-1/3$, down (d), strange (s) and bottom (b). The quarks are triplets under SU(3) group and thus carry an additional charge, referred to as *colour*.

In the lepton sector the $W^{\pm}$ bosons couple to leptons of the same family but in the quark sector they do not couple to the quark mass eigenstates q, but to linear combinations q$'$ of the quarks. Hence there is mixing between the three generations of quarks, which is parametrised by the Cabibbo-Kobayashi-Maskawa (CKM) matrix [8, 9]. The CKM matrix is parametrised by three angles and a phase. This phase can be chosen to be non-zero in order to accommodate CP-violation in weak interactions, as it has been observed both in the kaon system and in the B mesons system.

The number of massless (or almosta massless) neutrino types, and hence the number of lepton families, was confirmed to be three from precision measurements of the Z^0 line shape at LEP (CERN, Geneva) [10]. Moreover various cosmological considerations strongly this evidence. Similarly, the number of quark colours has been experimentally verified to be three. The completeness of the 3 family scheme of fermions predicted by the SM has also been verified experimentally through the long story of accelerator physics in the last century, with the latest achievement of the discovery of the top quark at CDF in 1995 [11, 12]. The structure of the electroweak (EW) interaction is nicely described by the local invariance under the Lie group SU(2)×U(1). Moreover the full symmetry of the Lagrangian and of the vacuum implies massless gauge bosons The idea of massive force mediators was argued because of the short-range of the interaction, and demonstrated in 1983 by the direct ob-

servation of the vector bosons $W^{\pm}$ and Z^0 at UA1 experiment [13]. In order to introduce mass terms for vector bosons, which carry the electroweak interaction, without spoiling the symmetry and the renormalizability of the theory, the existence of two Higgs fields [14] was postulated. Imposing to the Higgs scalar field a non-zero expectation value in the ground state breaks spontaneously the EW symmetry and generates mass terms for the $W^{\pm}$ and Z^0 gauge bosons. The generation of a neutral scalar boson H_0, the so-called Higgs boson, is the price paid to such symmetry breaking. The search of this particle, which is presently unobserved, is one of the experimental challenges of the Particle Physics research.

The masses of the SM fermions are generated from Yukawa couplings to the Higgs doublet field, with the values of each coupling proportional to the masses.

The strong interaction in the high energy regime is best described by *Quantum Chromo Dynamics* (QCD), based on a Lagrangian gauge invariant under the non-abelian Lie group $SU(3)$. The symmetry structure entails the existence of eight vector bosons, the gluons, that carry colour charge themselves and are thus self-interacting. This implies that the QCD coupling α_s is small for large momentum transfers (*asymptotic freedom*), but large for small momentum transfers, and leads to the confinement of quarks inside colour-neutral hadrons.

Moreover, the running of α_s implies that perturbative methods cannot be used at low energies, where prediction for strongly interacting systems are based on effective theories or other approximate symmetries. The only sector of the SM that has no experimental evidence is the Higgs sector. The Higgs boson mass is not theoretically predicted, thus the only information available can be derived from indirect constrains. The requirements on the

stability of the EW vacuum and the perturbative validity of the SM allows to set upper and lower bounds depending on the energy cutoff value chosen for the energy scale Λ, up to which the SM is assumed to be valid (Fig. 1.2). If the cutoff value is chosen at the Planck mass, which means that no new physics appears up to that scale, the Higgs boson mass is required to be in the range between $130 < m_H < 190$ GeV [1]. This bound becomes weaker if new physics appears at lower mass scales. If the cutoff is chosen to be 1 TeV, the Higgs boson mass is constrained to be in the range $50 < m_H < 800$ GeV. Direct Higgs boson searches at LEPII (CERN, Geneva) excluded a mass below 114.1 GeV at confidence level of 95% [15] (as shown in Fig. 1.3).

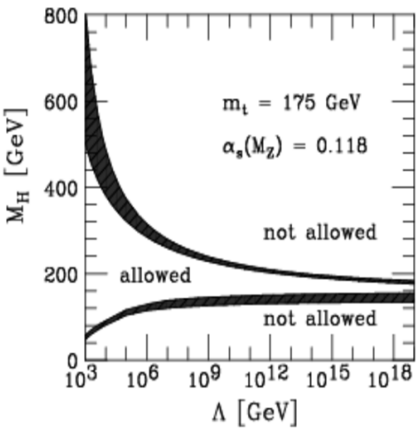

Figure 1.2. *Theoretical Higgs boson mass bounds of the electroweak theory.*

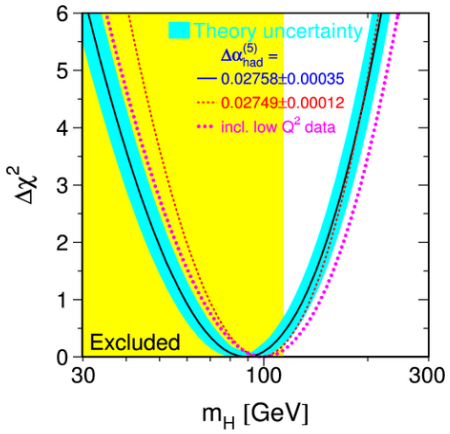

Figure 1.3. χ^2 *of the fit to the SM precision measurements as a function of Higgs boson mass.*

[1] The speed of light will be indicated in natural units $c = 1$.

1.1.2 Shortcomings of the Standard Model

At present, there are several reasons to imagine that SM is an effective description of a more fundamental theory. Perhaps the most obvious missing element is the gravity, which is not addressed by SM at all, in spite of being the most important long range force, whose effects determine the evolution of all the universe. On the other side, the strong interaction, although well described, is not unified with the electroweak interaction. These last two aspects violate the natural idea of Grand Unification Theory (GUT), which foresees, at higher energy scales, the unification of all forces. In addition there is no explanation for the 19 free parameters of the theory, neither for the number of fermion families. Finally, the recent experiments confirm neutrino oscillation, which is not accounted in the theory. Regarding the Higgs sector, it has been observed that the EW symmetry breaking is not a natural consequence of the theory.

To conclude this section it is useful to describe the "naturalness" problem (also known as "hierarchy" problem), which concerns the renormalisation of the Higgs boson mass. In a renormalisable theory the radiative corrections to the scalar mass, due to the boson and fermion loops, diverge quadratically with the cutoff on the loop momenta Λ. If this cutoff were to be placed at 10^{14} GeV (a rough estimation of the GUT scale), then the bare Higgs boson mass would be forced to the same scale. In this case, to reproduce the masses of Z and W bosons, the Higgs boson mass would be tuned to about 12 decimal places. On the basis of all these, and even more sofisticated considerations, many theories have been proposed. One of these, Supersymmetry (SUSY), will be shortly described in next section and later analysed in terms of possible experimental hints.

1.2 Discovery potentials of the LHC

1.2.1 Higgs search

As the mass of the Higgs boson is unknown, it is also not known under which conditions it will be produced. Direct Higgs searches performed so far have excluded values of the Higgs boson mass lower than 114 GeV by comparing expected production rates for some sensitive final states and existing data. A number of properties of the Higgs boson need to be measured, e.g. mass, spin, parity, couplings, branching ratios and width, but the most important property remains the mass, since that determines the coupling to other particles.

SM Higgs production

The most relevant Feynman diagrams describing Higgs production in pp collisions are shown in Fig. 1.4. The Higgs coupling to other particles depends on their mass, thus it is clear that the production processes should involve massive elementary particles. Moreover, for each channel, production cross section depends on the Higgs boson mass. The most important production mode is gluon fusion. Massive vector boson fusion is an order of magnitude in most of the interesting mass range for the Higgs boson, but becomes comparable to gluon fusion at very high values of m_H. Moreover, it is interesting because of the distinctive rapidity gaps that would be observed in the final states. The Higgs boson production cross sections are reported in Fig. 1.5 as functions of the Higgs boson mass. The complexity of the calculation gives rise to high (theoretical) uncertainties on the production processes and the reported values have to be considered only rough estimates. As reported in [16], specialised calculations and studies on some of these processes

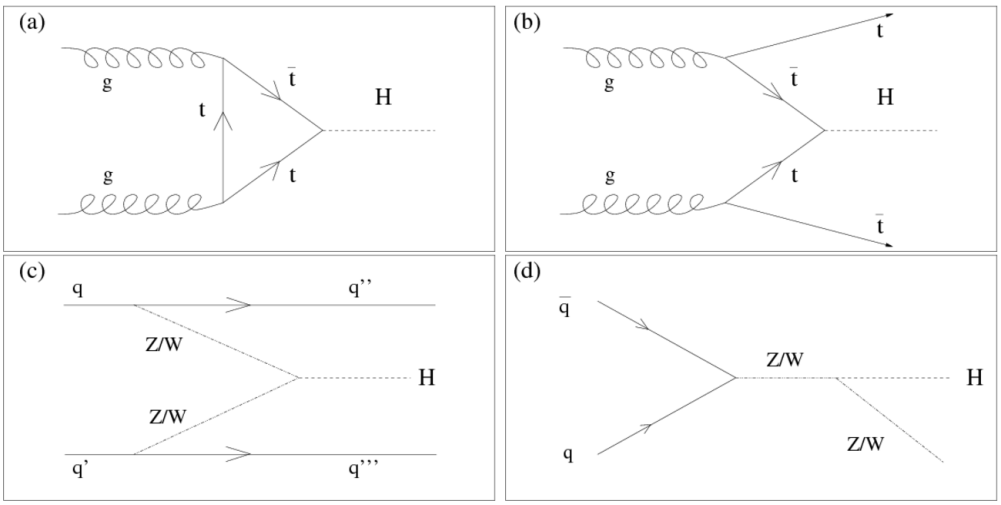

Figure 1.4. *Feynman diagrams corresponding to typical Higgs boson production processes at the LHC. (a) gluon fusion, (b) associated gluon fusion, (c) vector boson fusion and (d) associated quark fusion. The associated fusion production processes are often referred as Higgs strahlung or Higgs radiation.*

have yielded large correction factors (of the order of 100%), using higher order Feynman diagrams with respect to previous estimates obtained using PYTHIA.

Fig. 1.5 shows that Higgs boson production through gluon fusion dominates over the full mass range. This channel is characterised by a shoulder above $m_H \approx 2m_t \approx 340$ GeV due to a real top quark loop contribution (Fig.1.4-a). Despite the major attention is usually focused on gluon fusion and massive vector boson fusion production processes, a non negligible number of Higgs boson are expected to be produced through other processes (Fig.1.5, right scale). In this sense LHC has to be considered an "Higgs boson factory" with approximately 10^5 (expected) events per pb^{-1}.

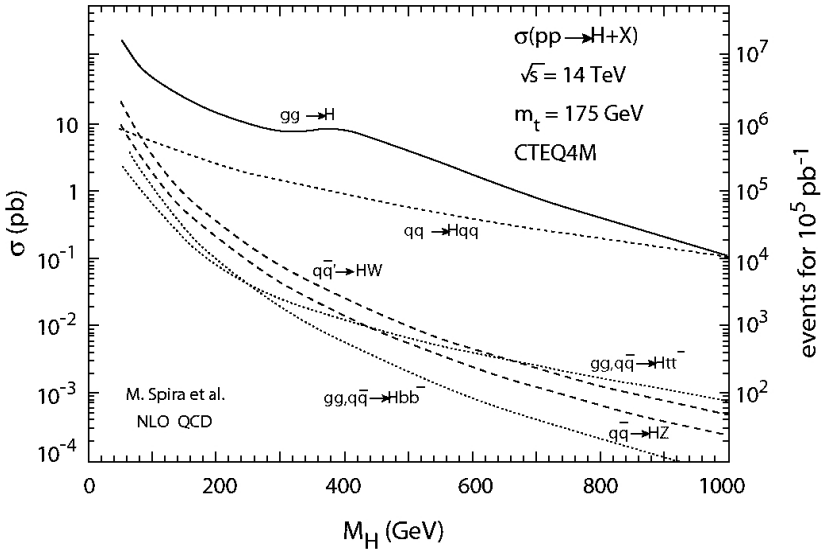

Figure 1.5. *Higgs boson cross sections expected at the LHC for the main production processes.*

SM Higgs decays

Like many other particles, the Higgs boson is not stable and it is expected to decay immediately after having been produced. As it happens in the production processes, also in the decay processes the largest coupling is obtained with the particles of highest mass. In Fig. 1.6 the branching ratios are represented as a function of the Higgs boson mass. We can divide the Higgs boson search in three mass ranges, each one characterised by some peculiar signatures.

Low mass range

In the mass region 80 $GeV < m_H < 130$ GeV the most important decay channels are:

$$H \to \gamma\gamma; \quad H \to b\bar{b} \tag{1.1}$$

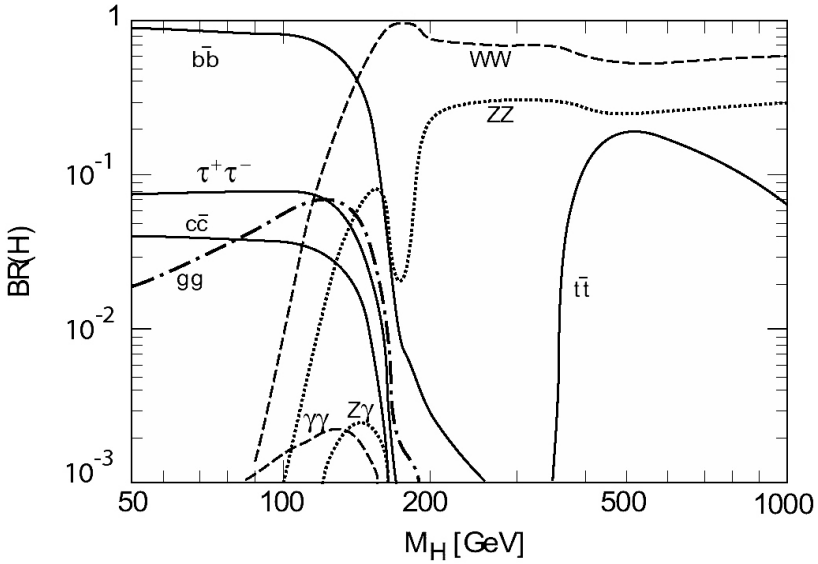

Figure 1.6. *Branching ratios of all possible Higgs boson decays as a function of the mass.*

The observation of $H \to \gamma\gamma$ puts several constraints on the performance of the calorimetry (Sec. 2.2.3), for which excellent energy and angular resolution are required to observe the narrow mass peak above the irreducible prompt $\gamma\gamma$ background. Furthermore misidentified jet from QCD background, electron/photon conversion and the Z resonance (if $m_H \approx m_Z$) will influence the precision of the measurement.

The rare decay in two photons, with a cross section of about 50 fb, has a high signal-to-background ratio S/B$\approx 10^{-3}$ and is considered the "golden channel" in the low mass range.

In contrast, the branching ratio for $H \to b\bar{b}$ is essentially 100% in the mass range below the threshold for the processes $H \to WW$ and $H \to ZZ$, since the b quark is the heaviest accessible particle. Unfortunately, despite the expected cross section is really high (about 20 pb), it will be hard to trigger on this decay channel because of the large $pp \to b\bar{b}$ cross section at the LHC.

Only in presence of a tag lepton (from the associated production WH, ZH and $t\bar{t}H$) it will be possible to trigger on this channel. The expected signal-to-background ratio in this case is S/B$\approx 10^{-5}$.
There is also possibility to detect the $H \rightarrow \tau^+\tau^-$ decay by tagging the vector boson fusion with one or two forward jets [17].

Intermediate mass range

In the mass range 130 $GeV < m_H <$ 180 GeV the decay channel

$$H \rightarrow ZZ^* \rightarrow 4l \tag{1.2}$$

provides a rather clean signature. Its branching ratio is larger than the $\gamma\gamma$ channel and increases up to 150 GeV, but the expected cross sections are quite small and the background sources are substantial. Good mass resolution and lepton isolation are required in order to find the signal. A pronounced dip in branching ratio is present between 150 $GeV < m_H <$ 180 GeV, due to the opening of the $H \rightarrow WW^* \rightarrow l\nu\ l\nu$ channel.

High mass range

With a Higgs boson mass between $2 \cdot m_Z < m_H <$ 600 GeV the channel

$$H \rightarrow ZZ \rightarrow 4l \tag{1.3}$$

is the most reliable for the discovery of a SM Higgs boson at the LHC. The background is dominated by the continuum production of Z boson pairs, which is expected to be smaller than the signal. The average momenta of the leptons in the final state are high and their measurements do not put severe requirements on the detector performance. In this channel the Higgs signal appears as a clear peak in the four lepton invariant mass on top of

the background. To obtain a clean reconstruction only electrons and muons are required in the final state. In conclusion, the four-lepton signal should be observed easily above the continuum background with only 10 fb^{-1} of collected data, expected in a year of running at 10^{33} $cm^{-2}s^{-1}$. Significant rejection of the continuum ZZ background can be achieved by requiring that the transverse momentum p_T^{max} of the harder Z is larger than a given value $(m_H/3)$.

If the Higgs boson mass is larger than 600 GeV, other decay channels with larger branching ratio must be considered. Three of such decays are: $H \rightarrow ZZ \rightarrow ll\nu\nu$, $H \rightarrow WW \rightarrow l\nu jj$ and $H \rightarrow ZZ \rightarrow lljj$, respectively with a rate of 6, 150 and 25 times larger than the four-lepton mode. Moreover, for Higgs boson with very large mass, these channels would be observable only requiring two jets in the forward region $(2 < |\eta| < 5)$. With this technique a SM Higgs boson could be observed up to 1 TeV.

1.2.2 Supersymmetry

Described in very general terms, Supersymmetry (SUSY) proposes the existence of another symmetry of nature, yet undiscovered, which links fermions and bosons. Many supersymmetric models have been proposed, a review may be found in [18].

From a phenomenological point of view, the effect of requiring supersymmetry in a Quantum Field Theory is that for each fermion (or boson) with assigned quantum numbers (except than mass and spin quantum numbers), there exist a boson (or fermion) with the same quantum numbers. Each of these new particles is known as "superpartner" of the SM corrispective (Fig. 1.7). SUSY particles got their names according to following rules:

- Fermionic superpartners of SM bosons got suffix "ino": gauge boson→gaugino

(e.g. photon→photino, W boson→Wino, Higgs boson→higgsino);

- Scalar superpartners of SM fermion got prefix "s": squarks, sleptons, sneutrinos (e.g. top quark→stop squark).

As in the SM, it is possible to consider "exact" the supersymmetry if SM particles and superpartners are degenerate in mass. It is supposed that SUSY particles have masses larger than SM counterparts because they are yet undiscovered.

The contribution to the consistency of the SM given by the introduction of these new particles is evident looking at the hierarchy problem in SUSY models. For each loop diagram in SM, supersymmetry requires another where the new loop particle is the superpartner of the SM one (see Fig. 1.8). Because of the Feynman rule, that requires a factor -1 to be inserted for each fermion loop, the leading terms in the cutoff in such diagrams will have a relative minus sign, and so these leading corrections to the Higgs boson mass will cancel out exactly.

When supersymmetry is broken to allow the supersymmetric particles to be

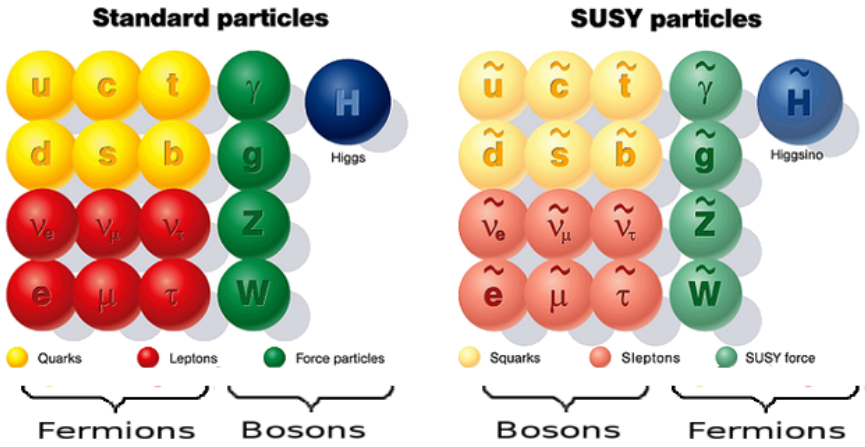

Figure 1.7. *SUSY particles.*

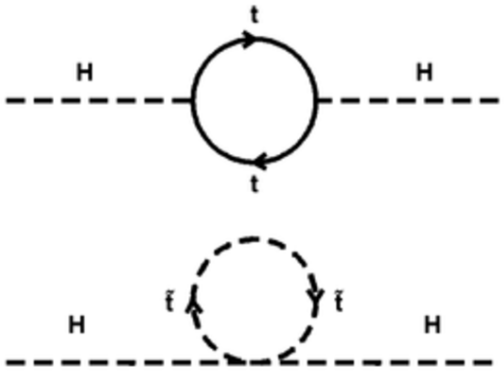

Figure 1.8. *One loop contribution to the Higgs boson mass from top quark and its super-partner (stop).*

heavier than the SM counterparts, one of the constrains on the allowable supersymmetric breaking interactions will be that they do not spoil this leading term cancellation. This is known as "soft" supersymmetry breaking. The remaining corrections to the Higgs boson mass in the unbroken theory are of the order of $|g_f^2|\ \mathrm{m}_f^2 \ln(\Lambda/\mathrm{m}_f)$, where Λ is the cutoff on the loop momentum, g_f is the coupling of the fermion to the Higgs boson and m_f is the fermion mass. This solves the hierarchy problem, reducing the correction to the Higgs boson mass from the Λ^2 of the SM to a more achievable $\mathrm{m}_f^2 \ln(\Lambda/\mathrm{m}_f)$. In particular, the correction to the Higgs boson bare mass is given by the so called m_{soft}, that is the difference in mass between the SM particle and the corresponding superpartner. If supersymmetry will be discovered up to 1 TeV it will solve the hierarchy problem, otherwise, also supersymmetry will require even finer tuning of the Higgs boson bare mass.

Since SUSY doesn't distinguish between quark/lepton fields and Higgs field, the barionic and leptonic numbers can be violated, as it has never been observed. In order to consider this effect, a new quantum number has been

introduced, the R-parity, $R = (-1)^{3B+L+2S}$, where B, L and S are the Barionic number, the Leptonic number and the Spin.
Therefore SUSY models can be divided in two classes: R-parity conserving ($R_P C$) and R-parity violating ($R_P V$). $R_P V$ theories allow SUSY particles to be produced singly and allow them to decay entirely in SM particles. If R-parity is conserved, in contrast, SUSY particles can be produced only in pairs. Furthermore R-parity conservation requires that the lightest supersymmetric particle (LSP) is stable. In this case the characteristic of an event is that the final state will contain exactly two LSPs and a number of SM decay products.
Other consequences of the $R_p C$ theories are that the proton is stable and the LSP is the main candidate to explain dark matter. Events are also characterised by high missing transverse energy (E_T^{miss}) because the LSP have large mass and are weekly interacting. The simplest SUSY model is the Minimal Supersymmetric extention of the Standard Model (MSSM). Other SUSY models are SUGRA (or SuperGravity), SGUT or (Supersymmetric Grand Unified Theories) and many more.

The MSSM model

The MSSM is the simplest SUSY model, in the sense that it introduces the minimal number of sparticle and is also an $R_P C$ model; clearly SM particles represent a subset of its particle content. The first stage in the construction of such a theory is to introduce "supermultiplets", in which all the (*unbroken*) SM particles are placed. Each supermultiplet is a two-component object which contains bosonic and fermionic fields, whose spins differ by one-half of a unit, and which may be related one to each other via a supersymmetric transformation. These two components are equivalent under the theory and

they must have a common representation under the gauge groups.
In this model the Supersymmetry is explicitly broken to allow the superpartners to become heavier than the SM counterparts, because they are not observed in the energy range currently accessible to experiments. The symmetry braking is obtained adding to the Lagrangian all the possible terms that do not break the gauge symmetry SU(3)×SU(2)×U(1), and furthermore that do not spoil out the cancellation of the leading terms of the radiative corrections to the Higgs boson mass. For this reason the terms added to the Lagrangian are usually indicated as "soft terms".
The broken MSSM (as all the SUSY theories) has a large number of free parameters, generated mainly from the symmetry breaking. A careful analysis reveals 105 free parameters (masses, phases and mixing angles) in the MSSM, that introduce a tremendous arbitrariness to the Lagrangian.

1.3 Precision Physics

1.3.1 Top physics

The top quark, discovered in 1995 at CDF [11, 12], is the only known fundamental fermion with a mass at the electroweak scale. Twelve years after its discovery still quite little is known about its production and decay mechanism, which can give significant hints on the study of electroweak symmetry breaking and possible new physics.
Next-to-leading order (NLO) predictions on the $t\bar{t}$ production cross section at the LHC gives $\sigma(t\bar{t})$=883 pb, that implies a production of more than 8 million $t\bar{t}$ pairs per year at low luminosity ($10^{33} cm^{-2} s^{-1}$). For this reason the LHC is usually considered a "top quark factory", where a very large variety of studies on top physics will be possible. In addition, the LHC will be an

excellent place to search for the possible existence of fourth generation quarks and leptons, considering that in one year at low luminosity approximately 1000 events would be produced for a quark mass of 900 GeV/c^2.
There are several reasons to study in detail the top quark physics:

- within the Standard Model, an accurate measurement of top mass (m_t) helps constrain the mass of the Higgs boson;
- the large value of m_t indicates that top studies may give a good probe of the EWSB, of fermion mass generation and of possible existence of other massive particles;
- top quark events represent the dominant background in many searches of new physics at the TeV scale and therefore detailed measurements of production rate and event properties are needed to improve the sensitivity to new physics events;
- the decay channel W→jj in top quark events provides an important *in situ* calibration source for the detector calorimeters.

Particular attention will be given to the measurement of the top quark mass, that is one of the fundamental parameters of the Standard Model.

Selection criteria

At the TeV scale the largest source of top quark is the production of $t\bar{t}$ pairs from gluon-gluon fusion. The decays, according to the SM, happen almost always in the Wb channel, thus the final states depend on the decay mode of the W bosons. Approximately in the 65.5% of the events both the W bosons decay hadronically via $W \to jj$, or at least one decays via $W \to \tau\nu$. These events are difficult to extract above the large QCD multi-jet background and

are therefore considered less interesting. A more clean signature is given by W decaying leptonically with an electron or muon in the final state. These events are characterised by a high-p_T lepton and by large $E_T{}^{miss}$, due to the escaping neutrino. The presence of a isolated fermion of high-p_T is a good trigger signature, allowing a high trigger efficiency, and a powerful handle to reject multi-jet background. The leptonic events represent the 34.5% of all $t\bar{t}$ events and can be divided in "single lepton plus jet" and "double lepton" samples, depending on whether only one or both the W's decay leptonically, following:

$$t\bar{t} \rightarrow WWb\bar{b} \rightarrow (l\nu)(jj)b\bar{b}, \tag{1.4}$$

$$t\bar{t} \rightarrow WWb\bar{b} \rightarrow (l\nu)(l\nu)b\bar{b}. \tag{1.5}$$

In ATLAS one expects, for an integrated luminosity of 10 fb^{-1}, 2.5 million events with only one lepton in the final state. Requiring for these events one b-tagged jet, reduces the sample to the 60% of the total because of the b-tagging efficiency, but increases the background rejection by a factor 100. Detailed studies [19] have shown that for $L_{int} = 10$ fb^{-1}, requiring an isolated lepton with $p_T > 20$ GeV, $E_T{}^{miss} > 20$ GeV and at least four jets with $p_T > 20$ GeV, including one b-tagged jet, reduces the sample to $\sim 8 \cdot 10^5$ events. In Fig. 1.9 are shown the lepton p_T and jet multiplicity distributions for lepton plus jet events, requiring the lepton p_T exceeding 20 GeV. For the same integrated luminosity $\sim 4 \cdot 10^5$ di-lepton events are expected. The largest sample of $t\bar{t}$ consists of six-jet events from the fully hadronic decay

$$t\bar{t} \rightarrow WWb\bar{b} \rightarrow (jj)(jj)b\bar{b}. \tag{1.6}$$

which roughly correspond to $37 \cdot 10^5$ events for $L_{int} = 10$ fb^{-1}.
The multi-jet sample suffers from a very large background and is really difficult to trigger. Requiring six jets in the final state, including two identified b-

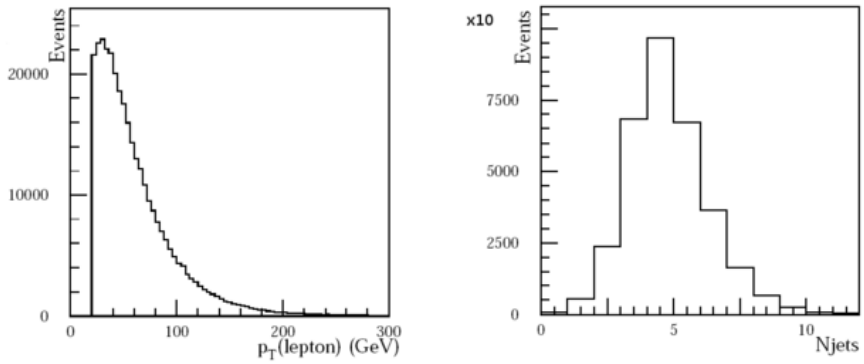

Figure 1.9. *Left: lepton p_T distribution for single lepton plus jet events with a lepton $p_T > 20$ GeV, normalised to an integrated luminosity of 10 fb^{-1}. Right: distribution of jet multiplicity (threshold at $p_T > 20$ GeV) for single lepton plus jet events with a lepton $p_T > 20$ GeV, normalised to an integrated luminosity of 10 fb^{-1}.*

jets, gives a signal-to-background ratio $S/B \approx 1/57$, that can be improved to $S/B \approx 1/8$ by imposing additional constraints on the W mass ($\chi^2_W \leq 7$) and on the difference between reconstructed top and anti-top masses ($\chi^2_W \leq 3.5$). In general the jet rates and topology suffer from large theoretical errors; a factor three or even larger has been estimated comparing data simulated with PYTHIA [20] and NJETS [21].

Measurement of the top quark mass

The top quark mass has been measured in the lepton+jets, di-lepton and all-jet channel by both CDF and $D\varnothing$. At the present, the most precise measurements come from the lepton+jets channel containing four or more jets and large E_T^{miss}. Its value is 174.2 $\pm$ 2.0 $\pm$ 2.6 GeV [22].
Since it is well known, radiative corrections in the SM relate the masses of the top quark and of the W to the SM Higgs boson mass (Fig. 1.10).

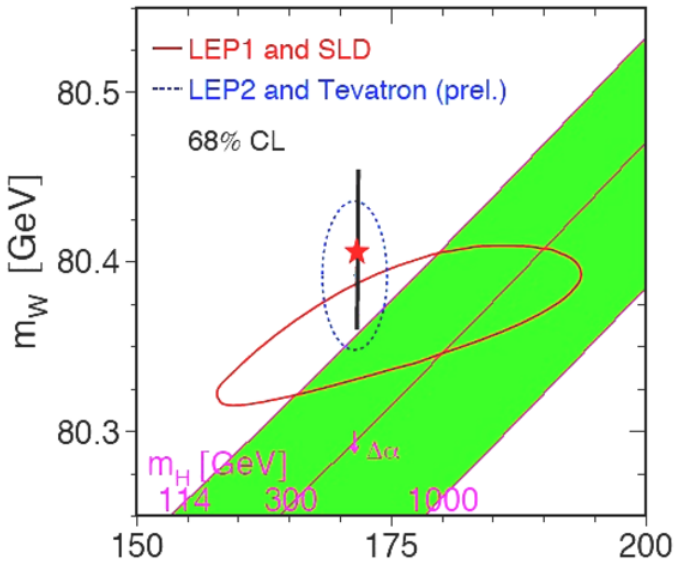

Figure 1.10. *Top vs W mass.*

Assuming that m_W is measured with an accuracy of 20 MeV, a determination of m_t with a precision of 2 GeV would be required to match that from m_W and theoretical uncertainties. Other models beyond the SM will profit from an uncertainty $\delta m_t \approx 1$ GeV. Given the large number of top events that will be available at the LHC, the uncertainty on the measurement of m_t will be dominated by systematic errors. Several different data samples and methods, with somewhat different sensitivities to systematic errors, can be used, and the resulting measurements can then be combined for an optimal precision. The process reported in (1.4) provides a large sample of top quark events, featuring a high-p_T isolated lepton providing an efficient trigger. The lepton and missing E_T give a large suppression of backgrounds from QCD and $b\bar{b}$ production. The major sources of background are associated production of W plus jet with $W \to l\nu$ decay, and Z plus jet with $Z \to ll$. Some constraints and assumptions are required to close the event and calculate the

top mass because of the permutation of the 4 jets (24 combinations) and because the neutrino is unrevealed.

In principle to calculate the $p_z(\nu)$ one can assume:

$$m_\nu = 0, \quad E_T(\nu) = E_T^{miss}, \quad m_{l\nu} = m_W, \tag{1.7}$$

while the top mass can be computed with a three-constraint fit:

$$m_{jj} = m_W, \quad m_{jjb} = m_{l\nu b} = m_t. \tag{1.8}$$

In practice this method is strongly correlated to the modelling and understanding of the E_T^{miss} distribution and resolution, thus suffers from big systematic errors.

What is usually preferred (this technique is used at CDF and $D\varnothing$) is to exploit the lepton and missing E_T to tag the event, and to calculate m_t as the invariant mass of the three-jet system arising from the hadronic top quark decay. With this method the signal-to-background ratio is expected to be $S/B \approx 65$. The W mass is calculated using the two jets invariant mass and a first sample is selected requiring $\delta m_W < 20$ GeV. The major background in this case is given by wrong combinations in the $t\bar{t}$ events themselves. To choose the right b-jet to be combined with the W, different methods have been studied using Monte Carlo simulations. By choosing the b-jet that maximises the reconstructed top quark p_T, the statistical error is $\delta m_t(stat) = 0.070$ GeV and can be reduced to $\delta m_t(stat) = 0.042$ GeV by relaxing the b-tagging criterion (at least one b-jet in the event) [19].

Given the high statistics available, it is possible to apply very tight cuts, accepting samples with lower statistical error. For example, requiring that the top and anti-top have both a high-p_T, they will be produced back-to-back, therefore reducing the combinatorial background and avoiding to select which jets have to be combined to reconstruct the correct mass. The price paid in

this case is that the systematic uncertainty on the jet energy scale and the theoretical uncertainty from gluon final state radiation will strongly influence the measurement.

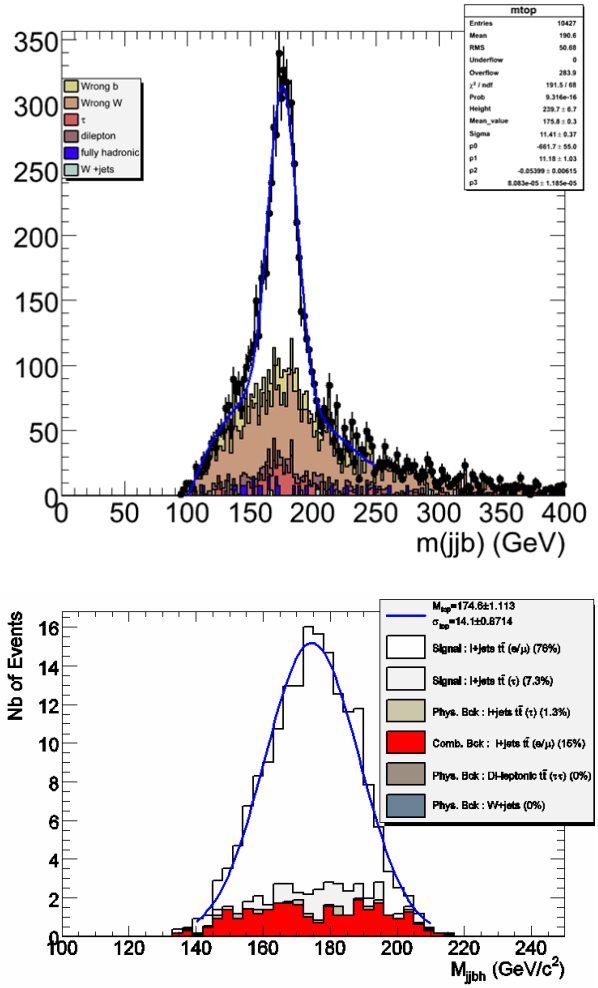

Figure 1.11. *Top: hadronic top mass distribution for an integrated luminosity of 1 fb^{-1} requiring the trigger signatures e25 or mu20. Bottom: additional cuts: M(hadronic W, leptonic b)>* 200 *GeV, M(leptonic top)<* 160 *GeV. Distributions obtained from MC simulations for the ATLAS detector.*

1.3.2 B physics

The rate of B-hadron production at the LHC is very large, with one collision in every hundred producing a $b\bar{b}$ pair [19]. The ATLAS B-physics trigger is based on the requirement of a muon of $p_T > 6$ GeV triggered at Level-1, and on a partial reconstruction of selected channels at Level-2 (typically $J/\psi \to \mu^+\mu^-$ or $J/\psi \to e^+e^-$). After the Level-1 muon trigger requirement, at the initial low luminosity of 10^{33} cm^{-2}s^{-1}, about 25% of the 23 kHz Level-1 rate will contain $b\bar{b}$ pairs. Typically, they are located in the central rapidity region and are characterised by high-p_T.

With the exception of the searches for rare decay modes, the physics potential discussed in the following is based on the expectation of three years of low luminosity running. In these conditions, the pile-up of several primary interactions in single triggered bunch crossings is not expected to induce major degradations of the performance. Extending the general B-physics studies into the high-luminosity data-taking is instead limited by trigger constraints. The most important subsystem in ATLAS for B-physics is the Inner Detector (Sec. 2.2.2). Electron identification is performed by the Transition Radiation Tracker (that will be described later in Sec. 2.2.2) and using the Electromagnetic Calorimeter (Sec. 2.2.3). Muon identification is performed using the Muon Spectrometer and the energy deposited in the last two layers of the Tile Calorimeter.

Most studies require information on the produced flavor of the B-hadron (i.e. if it containes a b-quark or a b-antiquark): this is achieved by tagging, i.e. measuring the charge of the lepton triggered at LVL1 which gives the flavor of the parent B meson and, hence, the flavor the other B meson decaying in the final state under study. The tagging is not perfect, and mistagging introduces a dilution in the observed asymmetries; the dilution is $1 - 2w_{tag}$,

where w_{tag} is the wrong-tag fraction. The tag cannot always be formed for each event, which leads to an inefficiency. Typically, lepton tags give a low efficiency but little dilution, whereas hadronic tags give high efficiency but large dilution.

CP violation studies

CP violation introduces time-dependent asymmetries:

$$A(t) = \frac{N(\overline{B^0} \to f)(t) - N(B^0 \to f)(t)}{N(\overline{B^0} \to f)(t) + N(B^0 \to f)(t)} \quad (1.9)$$

$$= a\cos(\Delta m \cdot t) + b\sin(\Delta m \cdot t) \quad (1.10)$$

where a is the direct CP-violation amplitude, b is the mixing-induced CP-violation amplitude and Δm is the $B^0 - \overline{B^0}$ mass difference. The angles in the unitarity triangle (α, β, γ) are usually determined from such asymmetries. It should be noted that in a pp collider such as the LHC, there is an inherent asymmetry at production; however, this is believed to be less than 1% within the ATLAS acceptance.
The measured asymmetries are degraded by the effects of incorrect tagging, backgrounds and the proper time resolution.

The β angle. The decay $B_d \to J/\psi K_s$ is easily triggered and reconstructed; moreover it is a very clear channel for the study of CP-violating parameters. For this reason, it is referred to as the 'Golden Channel' from both theoretical and experimental point of view. The signal events are isolated using combinatorial mass fits using both direction and mass constraints. Additional cuts are applied to the decay length transverse to the beam, on the fitted mass, and on the B_d^0 p_T and proper decay time. The J/ψ is reconstructed in both the μ^+ μ^- and e^+ e^- modes, and in the latter case refits

to the track are performed to account for bremsstrahlung. In signal events passing the Level-1 trigger, 80% of $J\psi \to \mu^+\mu^-$, 50% of $J\psi \to e^+e^-$ and 40% of $K_s^0 \to \pi^+\pi-$ are reconstructed.
The backgrounds are dominated by direct J/ψ production combined with K_s^0 from other B modes, fragmentation and fakes. The background induces an uncertainty estimated lower than 10%.
The time-dependent CP asymmetry can be written in a fairly simple form

$$A(t) = \frac{N(\overline{B_d^0} \to J/\psi K_s^0)(t) - N(B_d^0 \to J/\psi K_s^0)(t)}{N(\overline{B_d^0} \to J/\psi K_s^0)(t) + N(B_d^0 \to J/\psi K_s^0)(t)} \quad (1.11)$$

$$= a - \sin(2\beta) + \sin(\Delta m \cdot t) \quad (1.12)$$

Hence, from the observed signal events and tag information, $\sin(2\beta)$ can be determined.

The systematics can be controlled using the channels $B^+ \to J/\psi(\mu\mu)K^+$ and $B_d^0 \to J/\psi(\mu\mu)K^{*0}$; the former has good statistical precision but requires model assumptions to translate to the neutral B_0^d decay and to account for mixing, while the latter has lower statistics but includes the mixing and is less model dependent. The $B^\pm$ decays can be used to directly control charge biases in the tagging (which would introduce an apparent CP asymmetry), as well as the production asymmetry (assuming no CP violation in the decay). The overall expected accuracy on $\sin(2\beta)$ is $\delta(\sin 2\beta) = 0.012(\text{stat})+0.005(\text{syst})$.

Measuring α using $B_d \to \pi^+\pi^-$. The interpretation of the CP asymmetry in the decay $B_d \to \pi^+\pi^-$ is more complex due to the interplay between tree and penguin diagrams. The time-dependent asymmetry has the form $A(t) = a\cos(\Delta m \cdot t) + b\sin(\Delta m \cdot t)$, where a and b are related to the strong phase δ, the ratio of penguin to tree amplitudes A_p/A_t and the unitarity angle α. As δ is not calculable, the three unknowns are underconstrained,

and A_p/A_t must be taken from theory to determine α. The situation is made more difficult by the relatively low magnetic field in ATLAS and the rather poor track-by-track particle identification for hadrons. This leads to the signal being accompanied by backgrounds from many two-body B hadron decays (which may have their own CP asymmetries) and from the decay of the Λ_b.

This challenging problem is met with a likelihood fit which uses the dE/dx information in the TRT for each decay track, as discussed in more detail in [24], along with the proper decay time and the fitted mass to assign a probability for each combination fitted under the different decay hypothesis.

Analysis of the decay $B_d^0 \to D^0 K^{0*}$. The use of the decay amplitudes of several neutral B_d^0 decays to determine the angle γ as suggested by Dunietz [25] has been investigated. The following relations should hold:

$$A(B_d^0 \to \overline{D^0} K^{0*}) = A(\overline{B_d^0} \to D^0 \overline{K^{0*}}) \quad (1.13)$$

$$A(B_d^0 \to D^0 K^{0*}) = A(\overline{B_d^0} \to \overline{D^0 K^{0*}}) \quad (1.14)$$

$$A(B_d^0 \to D_{CP}^0 K^{0*}) \neq A(\overline{B_d^0} \to D_{CP}^0 \overline{K^{0*}}) \quad (1.15)$$

where the D^0 and K^{0*} decay into $K\pi$ and where D_{CP}^0 indicates a decay into a CP eigenstate (KK, $\pi\pi$). Unfortunately, some of the assumed branching ratios currently used by the LHC experiments are very low, e.g. $B_d^0 \to \overline{D^0 K^{0*}}$ which is of the order of 10^{-6}. After only trigger and acceptance requirements approximately 60 events per year would be retained in the rarest decay mode; the Level-2 trigger would also have to impose additional high-p_T thresholds on the decay hadrons to reject the combinatorial background. It can therefore be concluded that the measurement of all six decay modes will not be possible if the Standard Model branching ratios are correct.

Measurements with $B_s \to J/\psi\phi$. The $B_s \to J/\psi\phi$ decay is analogous to the $B_s \to J/\psi K_s^0$ decay, and the time-dependent CP-violating asymmetry can be measured with good accuracy. However, to interpret this in terms of quantities of physics interest, there are unknown parameters that must be controlled. This may be achieved by performing a full angular analysis [26]. A likelihood fit is performed to determine the difference in widths of the CP eigenstates the difference in the strong phases involved, and the CP violation amplitudes. If the current Standard Model predictions hold, the expected precision on the weak phase would only be $\sim 70\%$ after three years of low luminosity running, but still it would be possible to investigate deviations from that model.

Chapter 2

The ATLAS experiment at the LHC

2.1 Introduction

There are hints that new physics could be discovered at energies around the scale of the TeV. Search for such new physics is one of the goals of the Large Hadron Collider (LHC) [27]. This machine is being built in the existing 27 km LEP tunnel at CERN (Geneva) and will use the most advanced superconducting magnet and accelerator technologies ever employed. It will collide proton beams with energies of 7+7 TeV at a design luminosity of 10^{34} cm^{-2}s^{-1}, providing the experiments with very high interaction rates. It will also collide beams of heavy ions such as Pb with a total collision energy in excess of 1,250 TeV, about thirty times higher than the Relativistic Heavy Ion Collider (RHIC) at Brookhaven (USA).

2.1.1 The LHC collider

A complex system of accelerators will be used, to allow the proton beams to reach the final energy of 7 TeV. The new accelerator machine will use the former accelerator system operating at CERN. LHC will be supplied with protons from the injector chain Linac2 - Proton Synchrotron Booster (PSB) - Proton Synchrotron (PS) - Super Proton Synchrotron (SPS) as shown in Fig. 2.1. All these machines have been upgraded to meet the LHC demands. The energy of the Proton Synchrotron Booster has been increased from 1 GeV to 1.4 GeV. The beam brightness (intensity/emittance) of the PS machine is now almost twice the previous one and provides beams of 26 GeV of energy. The SPS is the last step before LHC, where beams are accelerated from 26 GeV to 450 GeV before extraction via two special transfer lines connecting the SPS and the LHC ring tunnel. During the years, many changes have been brought to the original plan, mainly due to the decision to close the CERN west experimental area, the modifications of proton bunch patterns and the approval of the CERN Neutrino to Gran Sasso (CNGS) facility, which shares the new SPS east extraction channel with LHC ring. To transport the protons beams at 450 GeV/c and the ions beams from the SPS to the LHC two new transfer lines have been built with a total length of 5.6 Km. The LHC machine comprises 1232 main dipole magnets and 392 main quadrupole magnets, which allow to keep protons beams at 7 TeV in two adjacent beam cavities. Superfluid helium cooling will provide the operational temperature of 1.9 K necessary to the superconductive magnet dipole to generate the B field strengths of 8.4 T needed to bend the proton beams. Beams collide in four interaction point at nominal centre of mass energy of 14 TeV. The number of interaction/second generated in the LHC at an interaction point (IP) is given by $N_{int} = \mathscr{L}\sigma_{total}$, where σ_{total} is the total cross section and $\mathscr{L}$

the instantaneous luminosity at the collision point.

The LHC is planned to have the first pilot run in the summer of 2008. In this phase 43 single bunches of protons will be transferred from PS to LHC via SPS. With 43 bunches per beam there will be no parasitic crossing and in order to provide collisions in the LHCb experiment IP bunches will be displaced by 75 ns. In 2008 and for the next three years, operation will be at 75 ns and subsequently at 25 ns bunch spacing. In the 75 ns mode, each beam will contain 936 bunches instead of 2808 as expected for final configuration. In the first run period the total current stored in a beam cannot exceed half the nominal value, this will limit the initial luminosity to $\mathscr{L} = 2 \times 10^{33}\text{cm}^{-2}\text{s}^{-1}$ until the 2010 run, when the accelerator machine should be ready to reach the final luminosity of $\mathscr{L} = 1 \times 10^{34}\text{cm}^{-2}\text{s}^{-1}$.

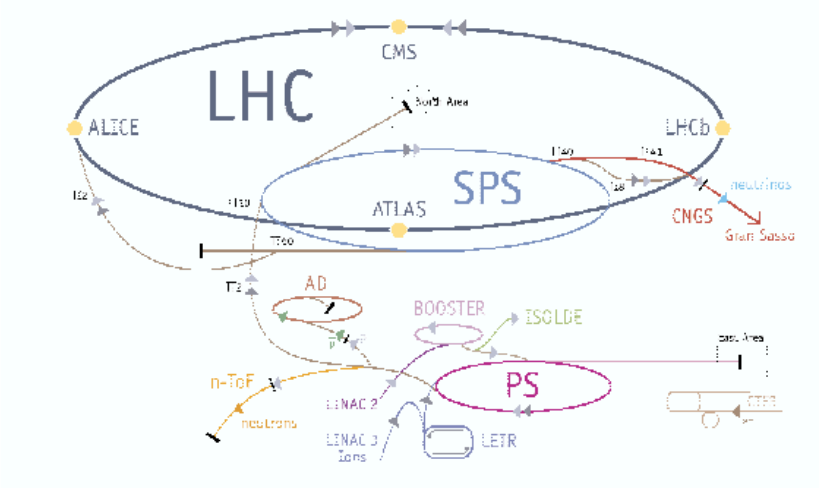

Figure 2.1. *CERN accelerator system.*

2.1.2 The ATLAS project

The ATLAS project consists of the design, construction and use of a particle detector named "A Toroidal LHC ApparatuS" (Fig. 2.2). It is one of the five experiments to be performed at the LHC and has been designed to cover the largest possible range of physics at TeV energies, from the search of new phenomena to the high precision measurements of SM processes.
ATLAS was conceived in 1992 from the merging of the EAGLE (Experiment for Accurate Gamma, Lepton and Energy measurements) and ASCOT (Apparatus with Super COnducting Toroids) collaborations [28] and announced with a Letter of Intent [29], followed in 1994 by a Technical Proposal [30].
The project quickly entered the design phase with the publication of the Technical Design Reports (TDR) for all the detector subsystems: Calorimeters [31, 32, 33], Inner Tracking Detector [34], Muon Spectrometer [35], Magnet Systems [36, 37, 38, 39], Level-1 Trigger [40] and Pixel detector [41].
The expected physics performance of the detector was documented in 1999 by a two-volume TDR [19], while the High Level Trigger [42] design and the Computing Model [43] were defined in 2003 and 2005, respectively.

At present, the ATLAS detector is completely installed in its experimental hall and is able to collect data from cosmic events. The integration of all the subsystem is reaching its final shape and the collaboration is working hard to be ready to study the first collisions expected for the summer 2008.

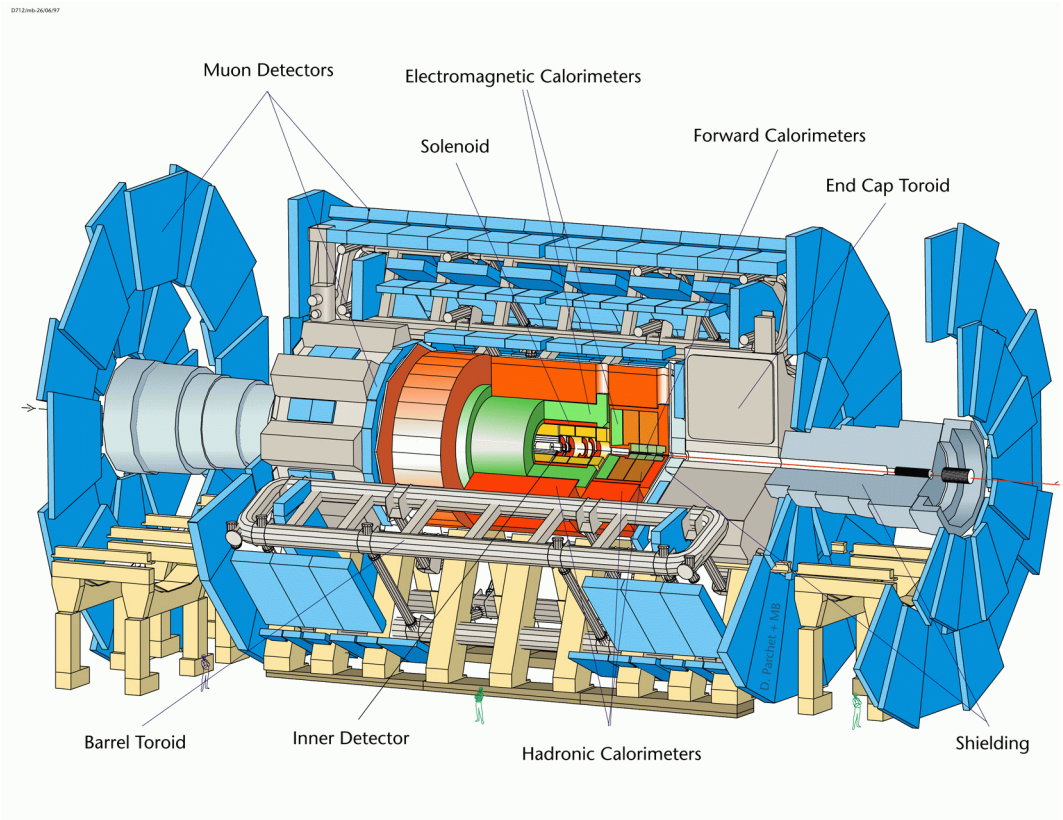

Figure 2.2. *Cut-out view of the ATLAS detector, showing all the subdetectors and the magnet system.*

2.2 Detector design and requirements

2.2.1 Magnetic Field

ATLAS uses a hybrid magnetic system composed by four large superconducting magnets. Overall, the system is 22 m in diameter and 26 m in length and has 1.6 GJ of stored energy. It is made up of a solenoidal axial field of 2 T for the Inner Detector provided by a thin solenoid that minimises the amount of material in front of the calorimeter system, and by a toroidal field of approximately 1 T for the muon detectors, composed by one barrel and two end-cap toroids.

In the Inner Detector (Sec. 2.2.2), the systematic error affecting the momentum measurement of charged particles is dominated by the relative alignment of detector components and by bending-power uncertainties, the former being the more demanding. A high-precision measurement of the W boson mass is clearly the most challenging goal for such measurements: a lepton from a W boson decay carries typically a transverse momentum of 40 GeV, resulting in a sagitta of approximately 1 mm as the lepton traverses the ID cavity. The systematic alignment uncertainties in the ID are unlikely to improve beyond the 1 μm level or 0.1% of the sagitta. This suggests setting a target of $\sim 5 \times 10^{-4}$ for the fractional bending power uncertainty, so that it remains negligible in the determination of the absolute momentum scale. Such stringent requirements can only be achieved reliably by *in-situ* mapping, using dedicated instrumentation inside the ID cavity, with all the relevant magnetic materials in place and just before the final installation of the ID itself. Eventual long-term drifts of the absolute scale will be detected to a much higher accuracy using permanently installed NMR probes [44].

In the Muon Spectrometer (Sec. 2.2.4), the expected sagitta is approxi-

mately 0.5 mm for a muon with a momentum of 1 TeV. The extraction of the momentum from the Monitored Drift Tube (MDT) chamber measurements requires a precise knowledge of the integral field between consecutive chambers along the muon trajectory. Because the field gradient can reach 1 mT/mm, local bending-power uncertainties translate into fluctuations of the momentum scale from one region in space to another, adding in quadrature to the overall momentum resolution. In addition, the interpretation, in terms of spatial coordinates, of the drift time measured in the MDT's is sensitive to the local electric and magnetic fields experienced by the ionisation electrons in each tube.

For a given muon trajectory, three sources of uncertainty affect the measured curvature: the field measurement errors, the accuracy on the relative position of muon chambers and magnet coils, and the trajectory measurement errors, in particular along the direction of the MDT wires.

For the purpose of setting specifications, it has been required (somewhat arbitrarily) that the combined effect of these sources degrade the momentum resolution by no more than 5% in relative terms; each source should then contribute to no more than $\sim$3% of fractional resolution degradation, anywhere in the MS volume.

In-situ mapping of the spectrometer by conventional techniques would have been impractical because of the rapidly-varying field and the very large volume. On the contrary, the muon system is equipped with a total of 1840 Hall probes; their readings are compared with magnetic simulations and used for reconstructing the field in space. This strategy was shown to meet the field-map specifications above, provided the B-sensor readings, after correcting for perturbations induced by magnetic materials (see Fig. 2.3) and by coil deformations (see Fig. 2.4), are accurate to $\sim$1 mT (absolute)

and the field direction is measured to within ±3 mrad.

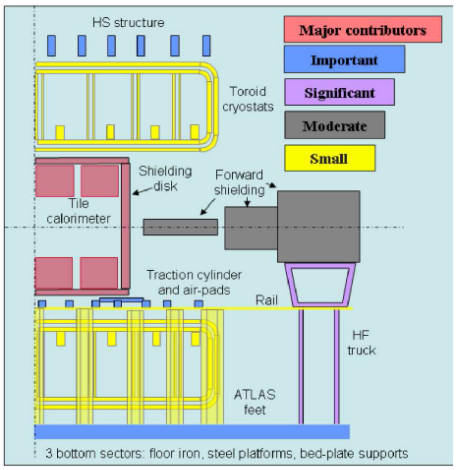

Figure 2.3. *Sources of magnetic perturbations induced by metallic structures in or near the muon spectrometer.*

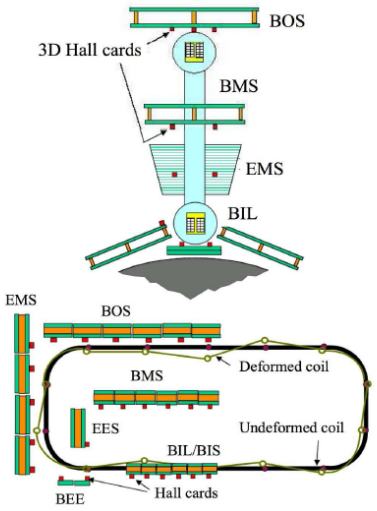

Figure 2.4. *Schematic representation of the magnetic-sensor layout and coil deformation model, used to reconstruct the magnetic field inside a barrel octant.*

Central Solenoid. The central solenoid [45] is shown in Fig. 2.5. It is designed to provide a 2 T axial field at the nominal operational current of 7.730 kA. To achieve the desired calorimeter performance, the layout was carefully optimised to keep the material thickness in front of the calorimeter as low as possible: the central solenoid contributes, in total, with ~ 0.66 radiation lengths at normal incidence. This target was achieved, in particular, using common vacuum vessel for the LAr calorimeter and the solenoid windings. A high-strength Al-stabilised $NbTi$ conductor has been specially developed to achieve a high field while optimising thickness.

The inner and outer diameters of the solenoid are 2.46 m and 2.56 m and

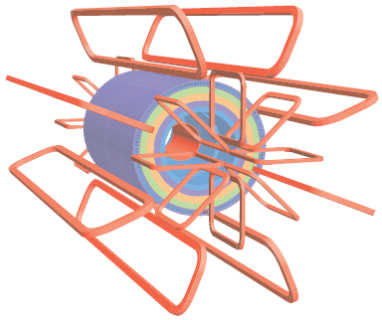

Figure 2.5. *Geometry of the magnet windings and tile calorimeter steel. The eight barrel toroid coils, with the end-cap coils are visible. The solenoid windings lies inside the calorimeter volume. The Tile calorimeter is modelled by four layers with different magnetic properties, plus an outside return yoke.*

its axial length is 5.8 m. The coil mass is 5.4 tonnes and the stored energy is 40 MJ. The stored-energy-to-mass ratio of only 7.4 kJ/kg at nominal field clearly demonstrates successful compliance with the design requirement of an extremely light-weight structure. The flux is returned by the steel of the ATLAS hadronic calorimeter and its girder structure.

The solenoid is charged and discharged in about 30 minutes. In the case of a quench, the stored energy is absorbed by the enthalpy of the cold mass which raises the cold mass temperature to a safe value of 120 K maximum. Re-cooling to 4.5 K is achieved within one day.

The coil was manufactured and pre-tested in a factory [46], came to CERN for integration in the LAr cryostat, underwent an on-surface acceptance test in its semi-final configuration [47], and was installed in its final central position in ATLAS in October 2005. The one week cool-down and a commissioning test up to nominal field were successfully completed in the summer of 2006 [48]. The solenoid is now ready for detector operation.

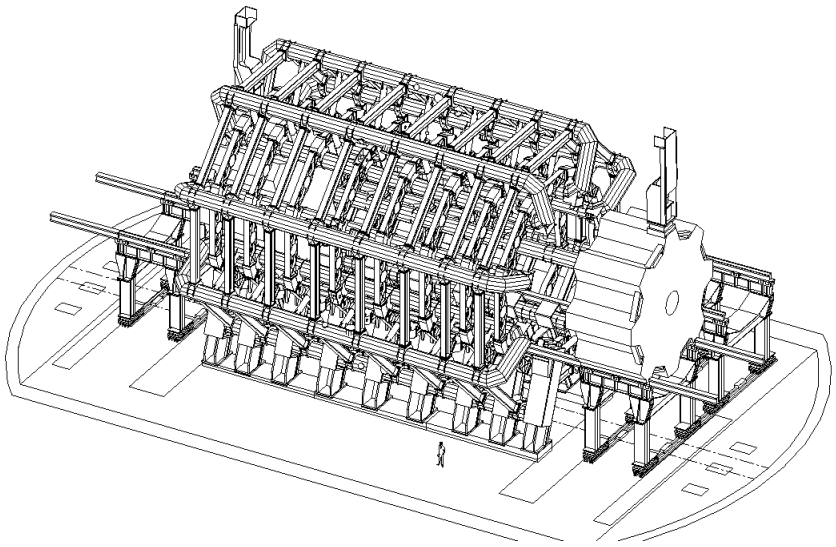

Figure 2.6. *Three-dimensional view of the superconducting air-core toroid magnet system. The right-hand end-cap magnet is shown retracted from its operating position.*

Toroids. The cylindrical volume surrounding the calorimeters and both end-cap toroids is filled by the magnetic field of the **Barrel Toroid** (Fig.2.6), which consists of eight coils encased in individual racetrack-shaped, stainless-steel vacuum vessels. The coil assembly is supported by eight inner and eight outer rings of struts. The overall size of the barrel toroid system as installed is 25.3 m in length, with inner and outer diameters of 9.4 m and 20.1 m, respectively.

The conductor and coil-winding technology is essentially the same in the barrel and end-cap toroids; it is based on winding a pure Al-stabilised $Nb/Ti/Cu$ conductor [49] into pancake-shaped coils, followed by vacuum impregnation.

The cold-mass and the cryostat integration [50] were performed at CERN over a period of approximately three years, and were completed in summer 2005. In parallel, all coils successfully underwent on-surface acceptance test

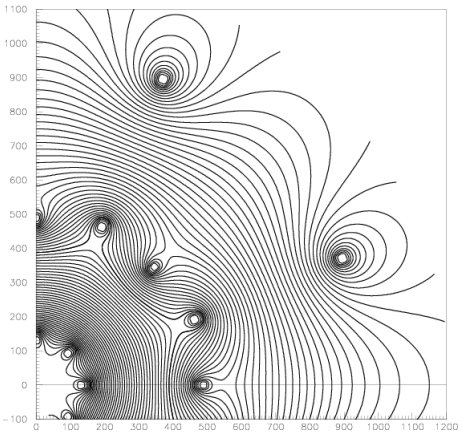

Figure 2.7. *Magnetic field map in the transition region between barrel and endcap toroids in a plain perpendicular to the beam axis. The interval separating consecutive lines is 0.1 Tm. Individual barrel and endcap coils are visible. Scales are in cm.*

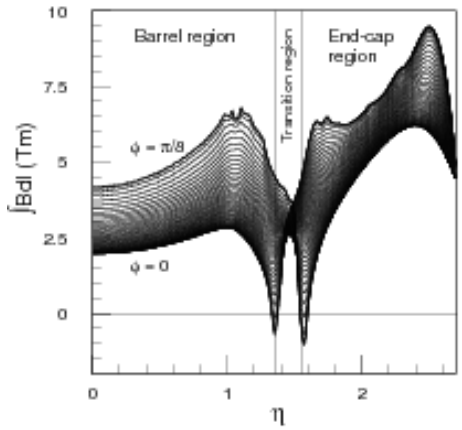

Figure 2.8. *Toroid bending power $\int B \cdot dl$ of the azimuthal field component, integrated between the first and the last muon chamber, as a function of pseudorapidity η. The curves correspond to azimuthal angles equally spaced between the BT and ECT coil planes.*

procedures [51]. Cool down and testing of the barrel toroid in the cavern took place in 2006 [52]. The cool down of the 360-tonne cold mass to 4.6 K takes five weeks. The test programme included normal ramps, up to nominal current (in 2 hours) followed by either a slow dump (in 2 hours) or a fast dump (in 2 minutes) in the case of a provoked quench.

The net Lorentz forces of approximately 1400 tonnes per coil directed inwards and the selfweight of the toroids are counteracted by the warm structure of *Al*-alloy struts mounted in between the eight coils. However, the barrel toroid structure still deflects significantly under its own weight. After release of the temporary support structure and systematic loading of the toroid with its own weight of 830 tonnes and the additional 400 tonnes of weight of the

muon chambers, the final shape of the toroid bore was designed to be cylindrical. The toroid coils were installed in calculated positions on an oval, longer by 30 mm in the vertical direction, to allow for structure deflection during load transfer from the temporary support structure. Since the release and removal of the installation supports, the upper edge of the toroid moved down by about 26 mm, which demonstrates that the design values had been well established and that the installation was precise to within a few millimetres. The installation of the barrel toroid in the ATLAS cavern commenced in October 2004. It took about 11 months to install the complete toroid. The overall structure design and installation experience are reported in [53].
The **End Cap Toroids** generate the magnetic field required for optimising the bending power in the end-cap regions of the muon spectrometer system. They are supported off and can slide along the central rails, which facilitates the opening of the detector for access and maintenance. Each end-cap toroid consists of a single cold mass built up from eight flat, square coil units and eight keystone wedges, bolted and glued together into a rigid structure to withstand the Lorentz forces. Design details are given elsewhere [54], and the production in industry of the coil modules and vacuum vessels is described in [55]. The cold masses were assembled and inserted into their cryostats at CERN. A crucial step in the integration process is the adjustment of the cold mass supports [56]. The weights of cold mass and vacuum vessel are 140 and 80 tonnes respectively. With the exception of windings, coil supports, and bore tube, the entire structure is made of *Al* alloy. With a weight of 240 tonnes, the end-cap toroids were some of the heaviest objects to be lowered into the cavern.
The end-cap-toroid cold masses will each be subject to a Lorentz force of 240 tonnes, pushing them against the stops mounted on the eight barrel toroid

coils. Achieving the correct sharing of the forces in the axial tie-rods has therefore been a critical design goal. Prior to their installation in the cavern in summer 2007, both end-cap toroids passed tests at 80 K to check the magnet mechanics and electrical insulation after thermal shrinkage. Once the end-cap toroids are powered in series with the barrel toroid, the peak stress in the barrel-toroid windings, in the areas where the magnetic fields overlap, will increase by about 30% before they were powered in combination with the barrel toroid. After a four-week cooldown, both end-cap toroids were successfully tested at half current, even if one at a time and in stand-alone mode. The final tests at full field will take place in the spring of 2008, after the installation of the shielding disks and with the end-cap calorimeters at their nominal position.

2.2.2 Inner Detector

The requirements on the performance of the ATLAS Inner Detector are more stringent than for any tracking detector ever built for operation at a high-luminosity hadron collider: the harsh environment at the LHC requires unprecedented speed of response and radiation-hardness of all its components. Large pile-up effects are also unavoidable at high-luminosity. In addition, access to the detector itself will be very limited. The high segmentation implies the presence of a high number of Front End and Control electronics, therefore the amount of material in the active volume of the Inner Detector is much larger than that of previous tracking detectors.

The ATLAS ID layout is shown in Fig. 2.9. The high occupancy of the detector dictates the granularity required to separate nearby tracks, while the precision on the momentum measurement sets the minimum number of precision hits per track.

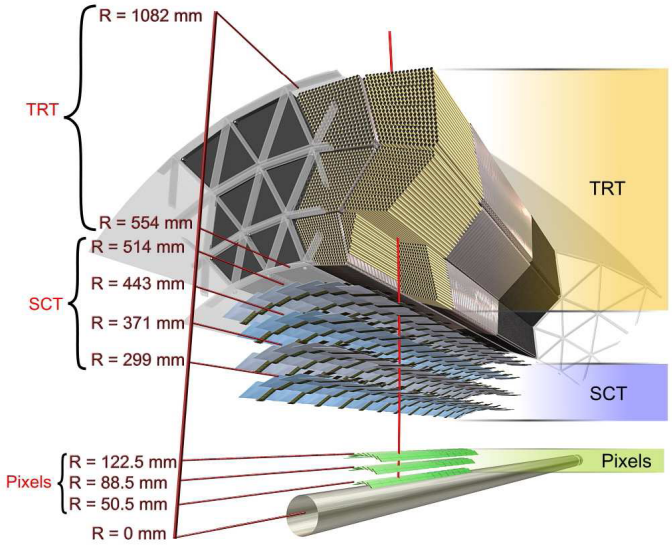

Figure 2.9. *The sensors and structural elements are traversed by a charged track of 10 GeV p_T in the barrel inner detector ($\eta = 0.3$). The track traverses successively the beryllium beam-pipe, the three cylindrical silicon pixel layers with individual sensor elements of size 50×400 μm^2, the four cylindrical double layers (one axial and one with a stereo angle of 40 mrad) of barrel SCT sensors of pitch 80 μm and finally approximately 36 axial straw tubes of 4 mm diameter contained in the barrel TRT modules within their support structure.*

The ID consists of three subdetectors covering the range $|\eta| \leq 2.5$. The inner subdetector consists of three layers of pixel detectors (Pixel), with a layer at a radius of 4 cm, called B-layer, which is crucial for good vertexing. Each pixel is 50 μm wide (in $R - \phi$) and 300 μm long (in z). The Silicon Central Tracker (SCT) is composed by four double layers of silicon strips. Each double layer consists of sensor with strips aligned in the longitudinal direction on one side and strips rotated by a 40 mrad stereo angle with respect to the first set on the other side. The strip pitch is 80 μm, the length of the wafers is 12 cm. The Pixel and SCT subdetectors are jointly referred to as the

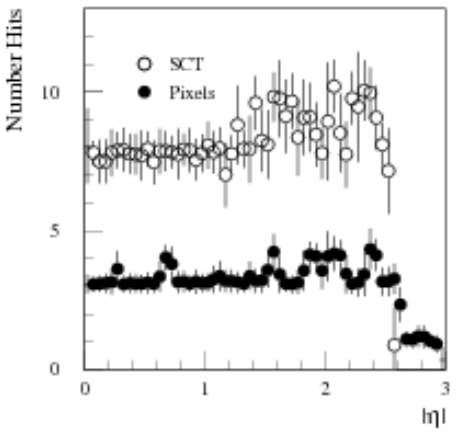

Figure 2.10. *Number of ID precision hits as a function of η.*

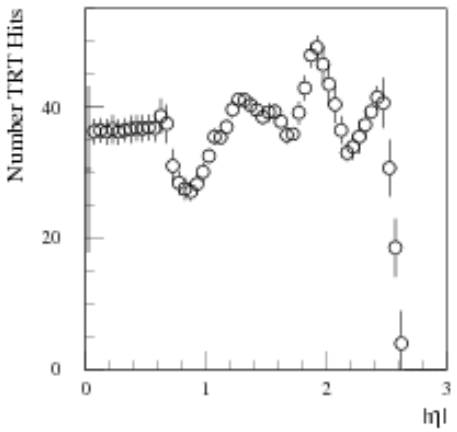

Figure 2.11. *Number of TRT hits as a function of η.*

Precision Tracker. The outer subdetector, the Transition Radiation Tracker (TRT), consists of 36 layers of 4 mm diameter straw tubes with resolution $\sim$200 μm, interspersed with a radiator to stimulate transition radiation (TR) from electrons. The detector is quoted with two thresholds for the recording of the signal at the output of the Front End electronics: the lower threshold is generically selecting signals from ionisation over background while the high threshold is intended to identify tracks associated with large energy deposition induced by TR photons. The ID design ensures fine-granularity in the region of the Precision Tracker, where the number of measurement layers is limited in order to contain the material amount and the costs (see Fig. 2.10). On the other hand the TRT guarantees a large number of tracking points (see Fig. 2.11), thus ensuring good p_T resolution and the identification of vertexes from the decay of long lived neutral particles (usually indicated as V_0 in ATLAS).

Pixel Detector

Three Pixel measurements over the full acceptance are crucial for a good impact parameter resolution and for short-lived particles detection. The two-dimensional segmentation requires advanced electronic techniques and interconnections for readout, while the high radiation environment requires radiation-hard chips. Each Pixel sensor is a 16.4×60.8 mm^2 wafer of silicon, composed by 46,080 pixels, 16 Front End chips (FE) and one Module Control Chip (MCC). In total the Pixel detector is composed by 1744 modules, that sum up to 80 millions channels in a cylinder 1.4 m long and 0.5 m in diameter. The modules are identical for both barrel and endcap. The major heat source are the FE chips, that absorb $\sim$15 kW, and are therefore provided with dedicated cooling systems. The small distance from the Impact Point exposes the Pixel to high radiation fluxes. It will be expected, during the overall operational period, to be 10^{15} 1 MeV-equivalent-neutrons/cm^2, with a subsequent signal reduction (about 1/4 of the initial pulse height after ten years of operation).

Silicon Central Tracker

The SCT provides four precision measurements in the intermediate radial range. It contributes to improve resolution in measurements of momentum, impact parameter, vertex position and pattern recognition. It is made of four barrel layers in the radial range 30 cm$<$R$<$ 52 cm and by nine disks in the forward and backward directions in the radial range 26 cm$<$R$<$ 56 cm. The estimated spatial resolution is 16 μm in Rϕ and 580 μm in z, that can help to separate tracks as close as $\sim$200 μm. Substantial upgrades with respect to LEP and Tevatron collider's silicon detectors include better signal-to-noise ratio and fast signal processing thanks to parallel pipelines transport.

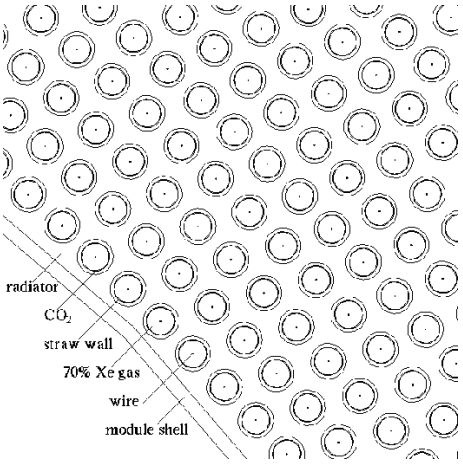

Figure 2.12. *Schematic view of one Transition Radiation Tracker barrel module ($R-\phi$ view).*

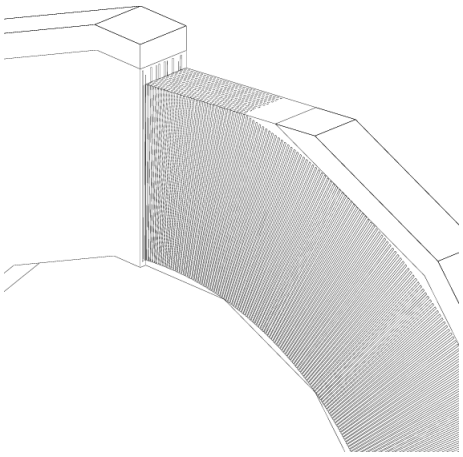

Figure 2.13. *Schematic view of one Transition Radiation Tracker end-cap module*

This allows to distinguish subsequent bunches and to use SCT data at LVL2 trigger. Each SCT layer is composed by modules of four single-sided silicon detectors with active area 61.6×62.0 mm^2. On one side 768 strips with 80 microns pitch are aligned precisely along the beam direction. The back-side detector part is identical, but rotated by 40 mrad. The small-angle stereo strips provide z-measurement capability and reduce ghost hits near a real track in high-multiplicity events. This choice ensures $R-\phi$ measurement in case of detector inefficiencies.

Transition Radiation Tracker

The Transition Radiation (TR) phenomenon [57] can be used to discriminate e^- from hadrons in the momentum range between 1 GeV and 1 TeV. The ATLAS TR Tracker (TRT) consists of straw tubes as active detectors and of radiators. In the barrel the straw tubes are parallel to the z axis and are organised in layers (see Fig. 2.12). There are 64 layers in the region

$|z| < 40$ cm and 73 in the region $|z| > 40$ cm. The straw layers are separated by ∼6.8 mm of radiator and are staggered in ϕ so that a stiff track will pass through 32 straws in average.

The end-cap (see Fig. 2.13) is composed by 14 short wheels and 4 long wheels, containing several radial straw planes: the short (long) layers contain 768 (576) straws.

Layers are staggered to guarantee a minimum number of hits on a track.

In total the TRT is made up of ∼372,000 straw tubes, with internal diameter 4 mm and thickness of 85 μm of kapton and 50 μm of CO_2 to ensure mechanical clearance between straw and radiator. The straws are filled with a mixture of 70% Xe, 20% CF_4, 10% CO_2 at atmospheric pressure. The central copper wire is 25 μm thick and each straw is broken in two electrically isolated halves at $z = 0$.

2.2.3 Calorimetry

The tasks of the calorimeters are the accurate measurement of the energy and impact point of electrons and photons and the measurement of the energy and direction of jets; henceforth they have a fundamental role in the measurement and of the missing transverse momentum of the event. Moreover they help the task of particle identification, for instance separation of electrons/photons from hadrons/jets, and of τ hadronic decays from jets.

The ATLAS calorimeters (shown in a schematic view in Fig. 2.14) will play a leading role in the reconstruction of the most important physics channels. The above requirements are complicated by the LHC environment: high resolution is required over a very wide energy range, extending from few GeV up to the TeV region, and it has to be achieved in high luminosity conditions.

The benchmark channels that have guided the design are the decay channels $H \rightarrow \gamma\gamma$, $H \rightarrow 4e$, and the search for heavy vector bosons (W',Z') with masses up to 5-6 TeV, through the decays $W' \rightarrow e\nu$ and $Z' \rightarrow e^+e^-$.

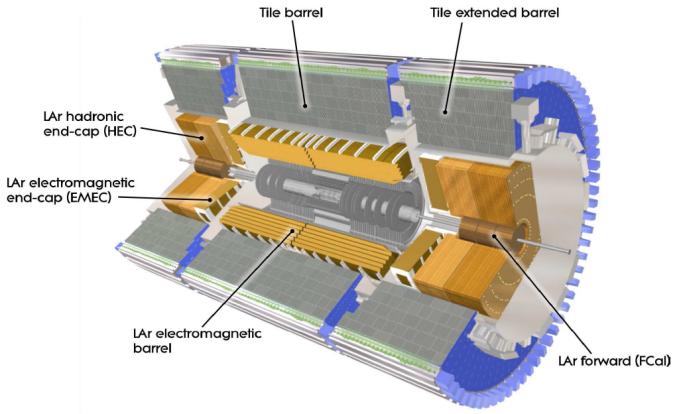

Figure 2.14. *A view of the ATLAS Calorimetric system.*

Electro-Magnetic calorimeter requirements

The EM calorimeter is designed to cover the widest possible range in rapidity and to maximise the physics reach of the experiment. As an example, the significance of the $H \rightarrow \gamma\gamma$ signal increases approximately with the square root of the EM calorimeter rapidity coverage. The precision electron and photon physics is limited by the ID coverage, thus up to $|\eta| < 2.5$ the best possible granularity is needed. In the range up to $|\eta| = 5$ a coarse granularity is acceptable to ensure a good measurement of the missing transverse energy and high efficiency in jet tagging. The electron reconstruction capability is required in a wide energy range: the identification of 1-2 GeV electrons from semileptonic decay of b-quarks increases the performance of b-jet tagging by about 10% (compared to using only vertex tagging). At

the same time, electrons up to ∼5 TeV are expected in the decay of heavy bosons. Excellent energy resolution is required in the range 10-300 GeV. The needed energy scale precision is of the order of 0.1%, while a linearity response better than 0.5% up to 300 GeV, and a shower direction resolution in θ ∼50 mrad/$\sqrt{E(GeV)}$. Finally, the high efficiency for $\gamma/e/\tau$ detection has to be balanced with the need to reduce as much as possible the combinatorial background from misidentified jets. The expected resolution of the ATLAS Liquid Ar/Pb accordion calorimeter is:

$$\Delta E = \frac{10\%}{\sqrt{E}} \oplus 0.4\% \oplus \frac{0.3}{E}. \tag{2.1}$$

Hadron calorimeter requirements

In terms of rapidity coverage, the requirements for the hadron calorimeter are very similar to those imposed to the electro-magnetic calorimeter. In practice, the jet detection capability has to extend up to $|\eta| = 5$ in order to allow an efficient tagging of forward jets associated to the production of the Higgs boson via vector boson fusion (see 1.2.1), as well as for a good missing p_T resolution. The most stringent requirement on the granularity comes from the W→jet-jet decay at high-p_T up to $|\eta| = 3$, where $\Delta\eta \times \Delta\phi = 0.1 \times 0.1$ is needed, while at larger η, $\Delta\eta \times \Delta\phi = 0.2 \times 0.2$ is sufficient. The segmentation in the radial direction is driven by particle identification, and by the possibility of achieving better energy resolution. Three samplings have been chosen for this purpose. The design resolution is set to provide jet reconstruction, jet-jet invariant mass reconstruction and missing p_T measurement for physical processes of interest [30]:

$$\frac{\Delta E}{E} = \frac{50\%}{\sqrt{E}} \oplus 3\% \qquad -3 < \eta < 3 \tag{2.2}$$

$$\frac{\Delta E_T}{E_T} = \frac{100\%}{\sqrt{E}} \oplus 10\% \qquad 3 < |\eta| < 5 \tag{2.3}$$

Quark compositness studies set the most stringent requirements on the linearity of the energy response, which is expected to be within 2% up to the energy of 4 TeV. The total thickness of about 10 interaction lengths is required for shower containment and good shielding of the μ chambers from the background.The time resolution of few nanoseconds allows bunch-crossing identification, and the peaking time of $\sim$40 ns is required to reduce the total noise, due to electronics and pile-up.

Detector Layout and Performance

The EM calorimeter covers the region up to $|\eta| < 3.2$. The presampler, installed immediately behind the cryostat cold wall, covers the region $|\eta| < 1.8$ and allows to correct for the energy lost in the material upstream of the calorimeter (inner detector, cryostat, coil). The hadronic calorimeter is segmented in a barrel (covering $|\eta| < 1.7$) and two end-cap sections ($1.5 < |\eta| < 3.2$). The forward calorimeters cover $3.1 < |\eta| < 4.9$.

The EM calorimeter is a lead-Liquid-Argon (LAr) detector with accordion geometry; its barrel part is contained in the barrel cryostat that shares the vacuum vessel with the Inner Detector solenoid. Two end-cap cryostats house the end-cap EM and hadronic calorimeters, as well as the integrated forward calorimeter. The hadronic barrel calorimeter is a cylinder divided into three sections: the central barrel and two extended barrels. It is based on a sampling technique with plastic scintillator plates (tiles) embedded in an iron absorber. At larger rapidities, where higher radiation resistance is needed, the intrinsically-hard LAr technology is used for all the calorimeters: the hadronic end-cap calorimeter, a copper-LAr detector with parallel plate geometry, and the forward calorimeter, a dense LAr calorimeter with rod electrodes in a tungsten matrix. The barrel and extended barrel Tile calorimeters

form an outer support cylinder, which also acts as the main solenoid flux return. The gap between the barrel and the end-cap calorimeters is filled with cables and services for the inner detector as well as power supplies and services for the barrel liquid-argon calorimeter. At the outer radius of the detector, a reduced section of a standard tile-calorimeter sub-module, the plug, provides additional coverage in this region and significantly reduces the neutron flux from the inner-detector volume into the muon system. The total weight of the calorimeters is ∼4000 tons.

The goal for ATLAS is to achieve a constant term of 0.7% or smaller over the full calorimeter acceptance. Non-uniformities of the response on the tested modules [58] do not exceed 0.7% and do not exceed even 0.5% in the case of the barrel modules. The overall constant term in the energy resolution ranges between 0.5% and 0.7% and therefore meets well the calorimeter design performance goals.

2.2.4 Muon Spectrometer

High-momentum final-state muons are amongst the most promising and robust signatures of physics at the LHC. To exploit this potential a high-resolution Muon Spectrometer (MS) [35] has been designed with stand-alone triggering and momentum measurement capability over a wide range of p_T, pseudorapidity, and azimuthal angle. The spectrometer must meet many demanding specifications in terms of operation, precision and realisation. It must operate reliably for many years in a never explored high-rate and high-background environment, setting stringent requirements on the possible chamber aging and on the detector segmentation, which is needed to deal with the high occupancy. The measurement accuracy must be commensurated with the physics requirements, that is ensured by the large air-core

magnetic field and by the precision chamber resolution.

Layout

The ATLAS Muon Spectrometer (Fig. 2.15) is a large apparatus of approximately cylindrical symmetry. The natural symmetry is broken by the feet structures supporting the detectors and by the apertures for access and services, such as cables and cryogenic pipe lines. It has been designed to provide a precise reconstruction of three track-segments in the bending plane. It measures ~ 40 m in length and ~ 11 m in radius and is divided into three main parts: the barrel, that covers the rapidity range $-1 \leq \eta \leq 1$, and two endcaps, that cover the rapidity range $1 < |\eta| \leq 2.7$. The trigger chambers are present up to $|\eta| = 2.4$.

The barrel is instrumented with Monitored Drift Tubes (MDT) that perform the precise track measurement, and with Resistive Plate Chambers (RPC) that are used for muon triggering, second coordinate measurement and bunch crossing identification. As shown in Fig. 2.16, in the barrel region the MDT are arranged in three cylindrical layers of stations, called 'Inner', 'Middle' and 'Outer', placed approximately at 5, 7.5 and 10 m from the Impact Point respectively. The Middle and Outer stations are instrumented also with RPC chambers, each one providing two independent $\eta \times \phi$ measurements (double-gap RPCs). The three RPC planes (two on both sides of the Middle station, one on the Outer station) are usually indicated (in order, starting from the innermost) as 'Low-p_T', 'Pivot' and 'High-p_T' planes, this naming scheme will be more clear in the section dedicated to the Muon Trigger (Sec. 3.2).
The endcap is usually subdivided in three regions: EC1 ($1 < |\eta| \leq 1.5$), EC2 ($1.5 < |\eta| \leq 2$), EC3 ($2 < |\eta| \leq 2.7$), where muon chambers form large wheels, perpendicular to the z-axis and located at distances of $|z| \approx 7.4$ m,

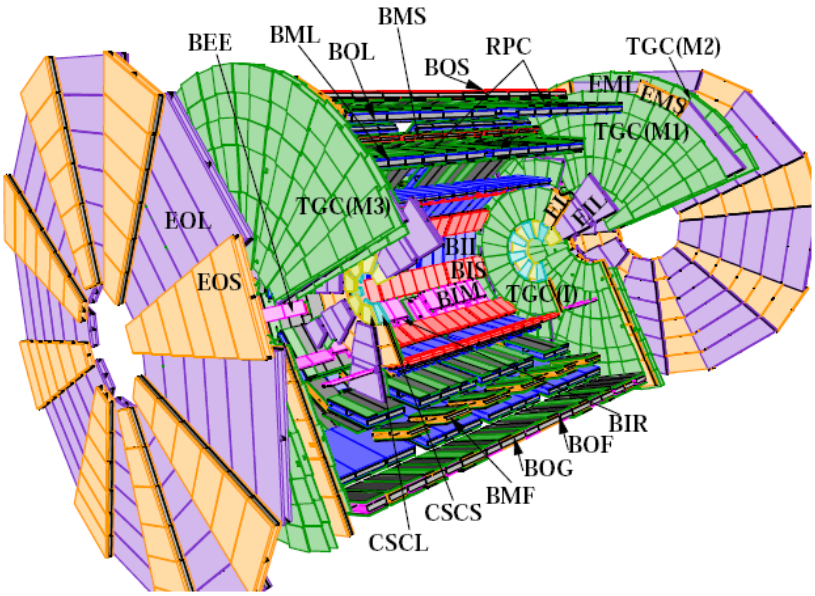

Figure 2.15. *Initial configuration of the Muon Spectrometer with its four chamber sub-system.*

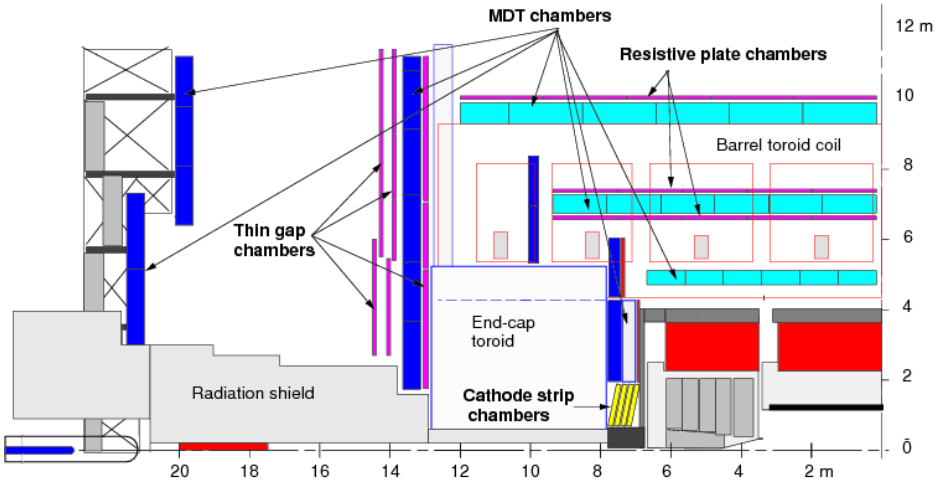

Figure 2.16. *Section of the Muon Spectrometer, showing the technologies used for muon track measurement and trigger.*

10.8 m, 14 m. The region indicated as EC1 is the barrel-endcap transition region and is affected by the magnetic field in-homogeneity. Similarly to EC1, the EC2 region is instrumented with MDTs for precision tracking and has a more homogeneous and well-controlled magnetic field. The region EC3 is characterised by very-high occupancy and, for this reason, Cathode Strip Chambers (CSC) have been chosen for the innermost layer of precision trackers.

Over all the end-cap regions Thin Gap Chambers (TGC) provide the LVL1 muon trigger up to $|\eta| = 2.4$. They are arranged in nine layers of gas volumes grouped into four planes in z. Three TGC planes are located in front and behind the second MDT wheel, while the fourth plane is located in front of the innermost tracking station. The TGC inner station (I) at $|z| \sim 7$ m consists of one plane of doublet units. At $|z| \sim 14$ m seven layers are arranged in one plane of triplet chambers (M1, closest to the interaction point) and two planes of doublet chambers (M2, M3). The doublet forming the plane farthest from the interaction point in each end-cap (M3) is referred to as the 'Pivot' plane, and its chamber layout and electronics are arranged such that, to a good approximation, there are no overlaps or holes in this plane.

Muon measurement

In the MS the tracks are defined by *superpoints* located midway along the local track segment between the chamber multilayers. These superpoints specify the location of the track segment along the z (axial) and along R (precision or radial) coordinates. The track curvature provides a measurement of the particle momentum. It is convenient to express the curvature in terms of a 'sagitta', which is the distance from the point measured in the

middle station to the straight line connecting the points in the inner and outer stations. A muon with a momentum of 1 TeV/c has a sagitta of about 500 μm, and the target momentum measurement precision of 10% translates into a sagitta precision of 50 μm . The actual precision depends not only on the local precision of the points measured in the muon chambers, but also on the relative positions of the three stations. These positions therefore need to be known with an accuracy that is comparable to the individual chamber point measurement precision. The target total contribution of the chamber point measurements to the sagitta precision is 40 μm. It is impossible to keep the geometry of the chambers stable to such precision. Permanent alignment systems are therefore needed to monitor the relative chamber positions with high accuracy, where the displacements in the sagitta direction are of primary importance. Each station of muon chambers does not only provide a point in space, but also a direction. This allows an angle-angle momentum measurement in addition to the sagitta measurement. Although this is less accurate, it allows a momentum measurement in case only two out of the three stations are hit by the muon and also, it improves the resolution for muons with low momentum. The toroidal magnetic field is perpendicular to the muon momentum direction at all rapidities, thus ensuring full bending power even at high rapidities.

The muon spectrometer is designed for a momentum resolution

$$\Delta p_T/p_T < 10^{-4} \times pc/\text{GeV}, \quad \text{for} \quad p_T > 300\text{GeV}/c \tag{2.4}$$

at smaller momenta the resolution is limited to a few per cent by multiple scattering in the magnet and detector structures, and by energy loss fluctuations in the calorimeters.

Precision tracking chambers

MDT. The basic detection element of the MDT chambers are aluminium tubes of about 30 mm diameter and 400 μm wall thickness, with a 50 μm diameter $W - Re$ central wire. The tubes operate with a non-flammable 93%-7% mixture of Ar-CO_2 gas at the pressure of 3 bar. The envisaged working point provides for an approximately linear space-time relation with a maximum drift time of $\sim$ 700 ns (as shown in Fig. 2.17) and good aging properties due to small gas amplification. To improve the resolution of a chamber beyond the single-wire limit and to achieve adequate redundancy for pattern recognition, the MDT chambers are constructed from 2×4 monolayers of drift tubes for the inner and 2×3 monolayers for the middle and outer stations. Each chamber has two multi-layers on both sides of a rigid support structure. A schematical drawing of an MDT chamber is shown in Fig. 2.18. When a muon passes through an MDT chamber, it hits six (or eight) drift tubes. The measured drift times are combined to reconstruct a track segment in the chamber. Effectively two parameters are determined for a track segment: the translation perpendicular to the track direction with a resolution between 28 and 32 μm, and the track angle with resolution between 0.16 and 0.50 mrad, where the ranges cover the various numbers of tube layers (2×3 or 2×4) and spacer heights. For more details on the MDT performance see [59].

CSC. The background rate in the $2 < |\eta| < 2.7$ region of the inner end-cap station is so large that it requires the use of precision detectors with higher granularity than MDTs (the limit for safe operation of MDTs is a counting rate of 150 Hz/cm^2). For this purpose Multi Wire Proportional Chambers (MWPC) with strip read out, called Cathode Strip Chambers (CSC), are

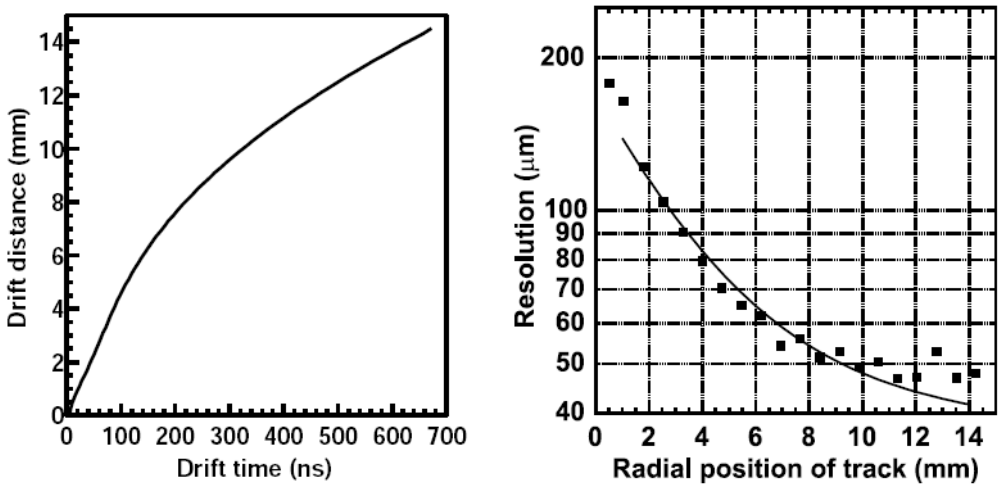

Figure 2.17. *Left: measured relation between drift distance and drift time for the ATLAS operating point. Right: resolution of an MDT as a function of the track position for the ATLAS operating point. Points show the measurements and the line shows a GARFIELD simulation.*

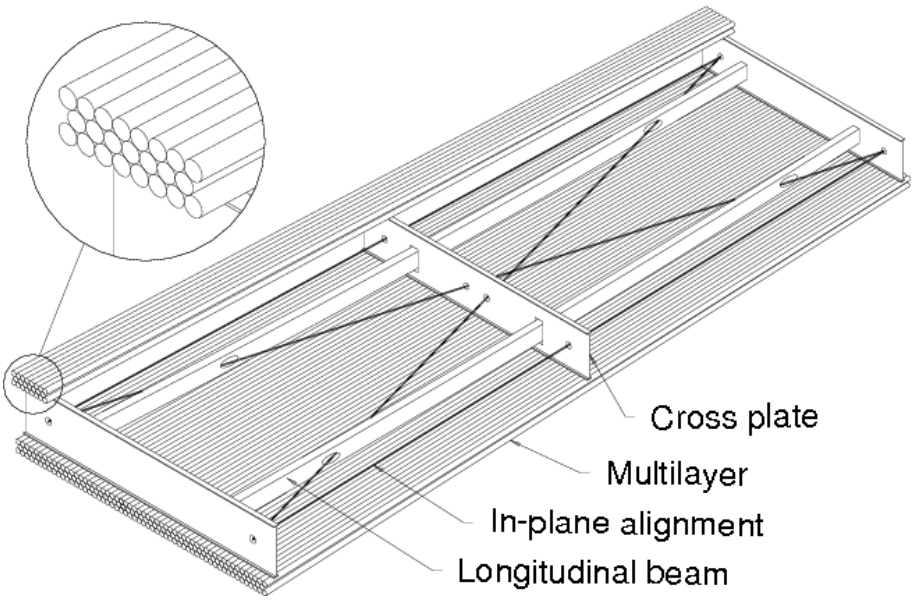

Figure 2.18. *Schematic view of an MDT chamber.*

used to cover this spectrometer region. CSC operation is considered safe up to 1 kHz/cm^2, which is sufficient to cope with the occupancy up to the forward boundary of the muon system at $|\eta| = 2.7$. In Fig. 2.19 are shown

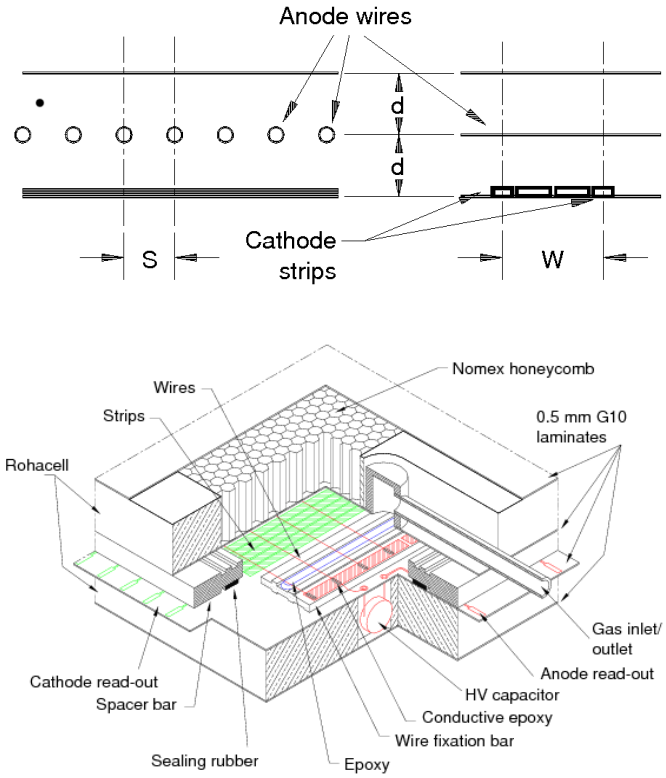

Figure 2.19. *Two schematic views of the CSC detector. On top the geometrical parameters of the detector: "d" is the distance between anode wires and cathode strips, "S" is the wire spacing, "W" the readout strip distance. Bottom: cut-out view of the detector components.*

two schematical views of the ATLAS CSC detectors. The sense wire pitch (S) is 2.54 mm, while the pitch of the read out strip (W) is 5.08 mm. The cathodes are segmented into two sets of strips, one orthogonal and the other parallel to the anode wires. Due to avalanche effects around the anode wire, charge is induced on the cathode and by charge interpolation between neigh-

boring strips, a high precision measurement can be accomplished. The track resolution in the bending plane is 60 μm for each CSC plane. The chambers are operated with a non-flammable 80%-20% mixture of Ar-CO_2 gas. Advantages of the CSC are small electron drift times, good time resolution, good two-tracks separation and low neutron sensitivity.
The whole CSC system consists of two disks with eight chambers each. Each chamber contains four CSC planes resulting in four independent measurements in η and ϕ along each track.

Trigger chambers

RPC. The RPC is a gaseous parallel electrode-plate (i.e. no wire) detector. Two resistive plates, made of phenolic-melaminic plastic laminate, are kept parallel to each other at a distance of 2 mm by insulating spacers. The electric field between the plates of about 4.9 kV/mm allows avalanches to form along the ionising tracks towards the anode. The signal is read out via capacitive coupling to metallic strips, which are mounted on the outer faces of the resistive plates. The gas used is a mixture of $C_2H_2F_4$/Iso-C_4H_{10}/SF_6 (94.7%/5%/0.3%) which combines relatively low operating voltage (due to the low SF_6 concentration), non-flammability and low cost, while providing a comfortable plateau for safe avalanche operation. A detailed presentation of the RPC system is given in [60]. RPCs can be operated both in avalanche and in streamer mode. In the high background environment encountered at the LHC, the avalanche mode offers the benefit of higher rate capability and rate-independent time resolution and has therefore been selected as the operation mode. At the nominal operating voltage of 9.8 kV, a signal with a width of about 5 ns is generated by the track with a streamer probability of less than 1%. Each RPC unit is thus made of two detector layers (i.e. gas

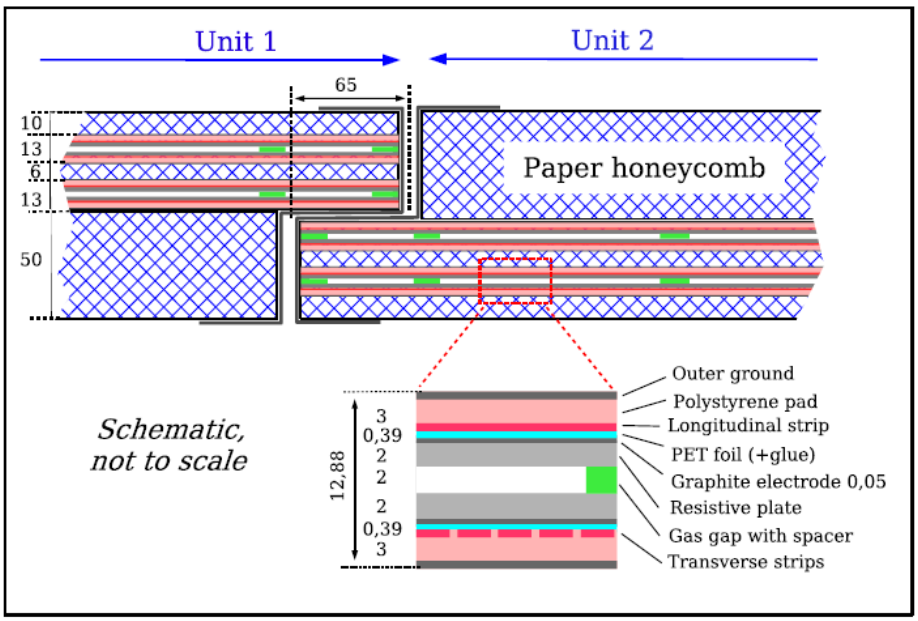

Figure 2.20. *Cross-section through a RPC, where two units are joined to form a chamber. Each unit has two gas volumes, supported by spacers, four resistive electrodes and four readout planes, reading the transverseand longitudinal direction. The sandwich structure, hashed, is made of paper honeycomb. The ϕ strips are in the drawing plane and the η strips perpendicular to it. Dimensions are given in mm.*

volumes) and four readout strip panels, two in η and two in ϕ, with a size between 25 and 35 mm. RPCs can safely operate at a rate of 1 kHz/cm^2, their operating parameters are discussed in detail in [61, 62, 63].

TGC. TGCs are Multi Wire Proportional Chambers with the characteristic that the wire-to-cathode distance (1.4 mm) is smaller than the wire-to-wire distance (1.8 mm), see Fig. 2.21. With a highly quenching gas mixture of CO_2 and $n - C_5H_{12}$ (n-pentane), this cell geometry allows for operation in a quasi-saturated mode, i.e. with a gas gain of $\sim 3 \times 10^5$. This relatively

low gas gain, compared to previous uses does not allow to make full use of its independence to the primary ionisation. Some of its characteristics are still kept, even at such a low gas gain. In particular the highly quenching gas prevents the occurrence of streamers in all operating conditions and the pulse height observed in the interaction of low energy neutrons (10 MeV) is only a factor 30 larger than for a minimum ionising particle.

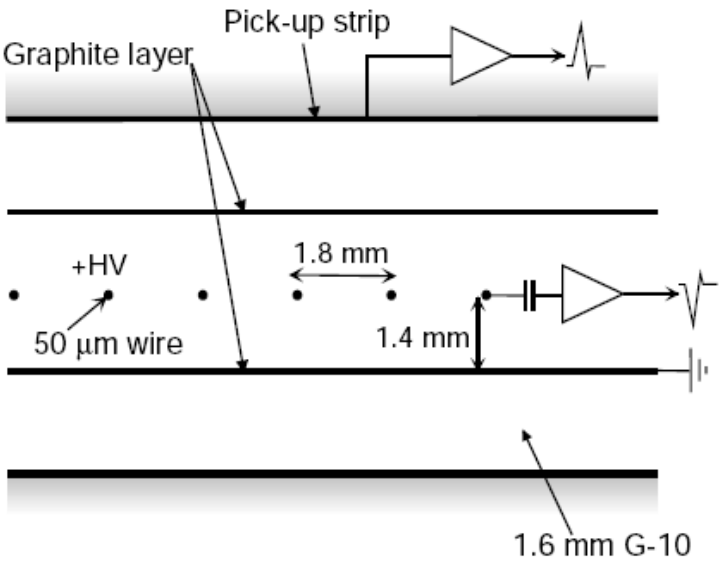

Figure 2.21. *TGC structure showing anode wires, graphite cathodes, G-10 layers and a pick-up strip, orthogonal to the wires.*

2.3 Trigger and DAQ

The LHC design instantaneous luminosity, $\mathscr{L} = 10^{34}$ cm^{-2}s^{-1}, will result in 23 inelastic proton-proton collisions per bunch crossing in average. Since the bunch crossing frequency is 40 MHz, the expected event rate is $\sim$ 1 GHz. On the other hand, the acquisition rate is limited by the maximum affordable data throughput rate, that is 300 MByte/s. In ATLAS, the mean event size is $\sim$ 1.5 MByte, entailing a maximum allowed acquisition rate of $\sim$ 200 Hz. Moreover, the cross sections of the interesting events at the LHC are highly suppressed compared to the total inelastic pp cross section (Fig. 2.22). As an example, the leptonic W decay (an interesting process for precise Electro-Weak measurements and for detector calibrations) is suppressed by a factor larger than 10^6 with respect to the total proton-proton cross section (σ_{tot}), and the Higgs Boson production (for $m_H = 100$ GeV/c) is expected to be suppressed by a factor greater than 10^9. Such environment requires a trigger system with high selection efficiency.

The ATLAS Trigger System is organised in three levels, each one refining the hypothesis formed at the previous one. The Level-1 (LVL1) is implemented in custom programmable electronics, directly connected to the front-end of calorimeters and muon detectors. It uses coarse granularity data from trigger chambers and has to reduce the event rate from the initial $\sim$1 GHz to $\sim$100 kHz (which corresponds to the input bandwidth of the Level-2 system) within a latency of 2.5 μs. At this stage Regions Of Interest (RoIs) are defined, i.e. regions of the detector where some significant activity is present. Only data fragments from the RoIs are passed to the Level-2 (LVL2), thus reducing drastically the processing time. The second (LVL2) and third (EF) trigger levels are implemented via sequences of software algorithms running on dedicated computing farms. They are usually referred to as High Level

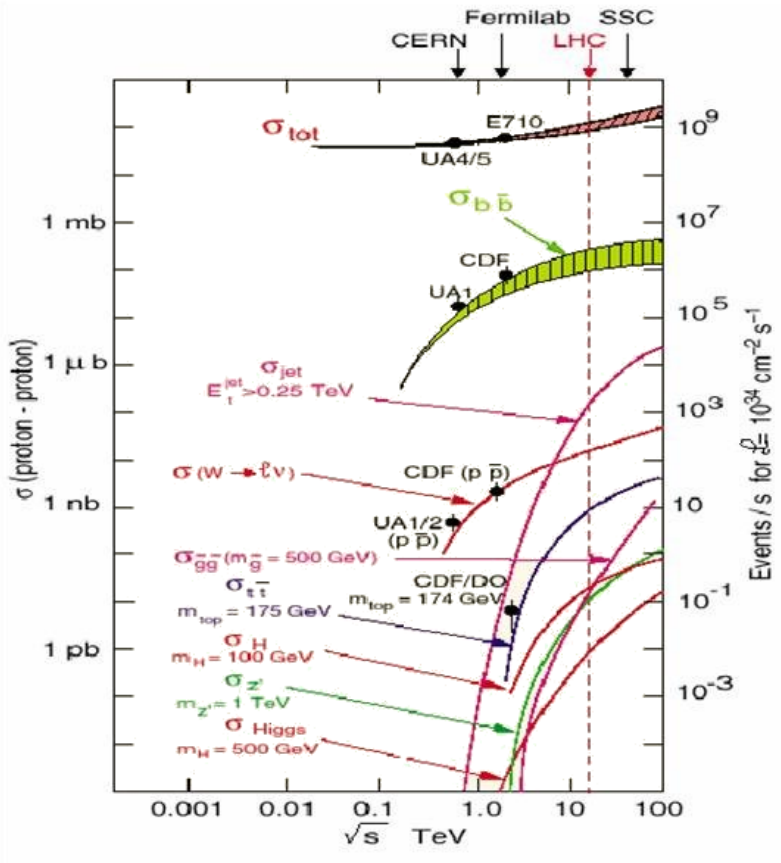

Figure 2.22. *Production cross section as a function of the centre of mass energy*

Trigger (HLT). At LVL2 full granularity data, inside the RoI identified at the previous level, are available. The LVL2 selection reduces the event rate from 100 kHz to 2 kHz, with a latency time of 10 ms. The last trigger level, called Event Filter (EF), has the ability to access the entire detector data as it runs after the Event Building. The total latency of the EF is ∼2s, therefore rather sofisticated algorithms can be executed in order to refine the selection and reduce the data throughput to 200 Hz. The EF algorithms can be seeded from LVL2 (or LVL1) or they can run blindly over the whole event.

The decision by each trigger level is based on combinations of objects required in coincidence or veto. These combinations are grouped together and are usually called "trigger menus". They are subject to continuous optimisations and updates up to and during the experiment. There are inclusive menus that allow the selection of events from unexpected new physics and menus for known processes, e.g. jet triggers used to measure jet cross-section and to study QCD processes. The thresholds in the physics trigger menus are chosen to give the best compromise between efficiency and acceptable trigger rate.

There are many sources of uncertainty on the estimated trigger rates. For these reasons the target output rates of each trigger level are set to values lower than the maximum allowable. The main sources of uncertainty are: the uncertainty of the pp inelastic cross-section, estimated to be $\sim 30\%$, the uncertainty on background processes, like low-p_T jet production and $b/c \rightarrow \mu X$ events, and the uncertainty due to estimates obtained using Monte Carlo techniques.

Trigger rates higher than acceptable values can be managed increasing the threshold values and using prescaling factors. The complete menus envisaged for data taking will include special detector monitoring and calibration triggers and a range of thresholds and prescale factors for each object type. These special triggers will be used to understand the detector and trigger efficiencies. The trigger commissioning will also require some combinations of prescaling and pass through strategies, specifically used for the trigger commissioning and algorithm optimisation. The ATLAS trigger data flow is sketched in Fig. 2.3. The data coming from the LVL1 trigger chambers are passed to the Central Trigger Processor (CTP) which makes the LVL1 decision based on trigger menu. The CTP passes the decision to the Timing

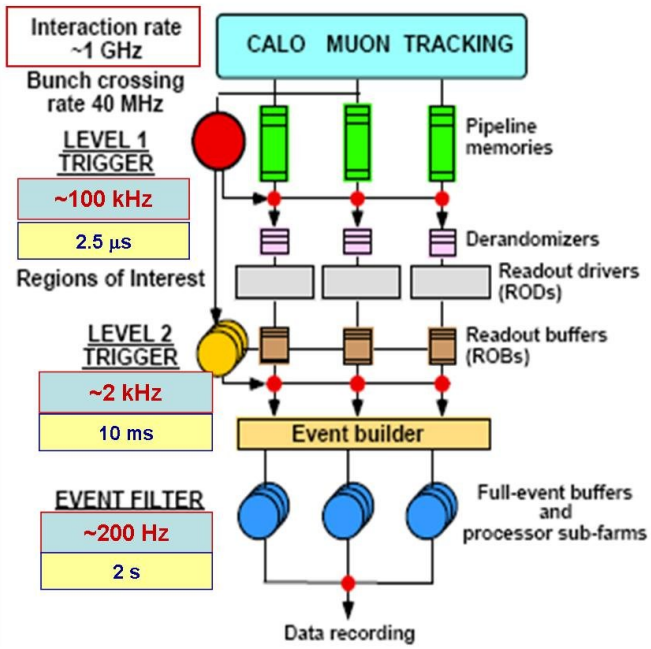

Figure 2.23. *Schematic view of the ATLAS trigger data flow.*

Trigger Control (TTC) which redistributes it to the front-end system and detector elements. At this stage the data, stored in pipelined memories on the detectors are sent to the Read Out Drivers (RODs) then to the Read Out Buffers (ROBs) where they are kept until LVL2 rejects or accepts the event. If the event is accepted these data are passed to the Event Builder (EB) which reconstructs the entire event before passing it to the Event Filter.

2.3.1 The LVL1 Trigger

The LVL1 trigger makes initial selection based on reduced granularity data from a subset of detectors. The muon trigger uses dedicate trigger detectors, i.e. RPCs in the barrel TGCs in the endcaps to identify high-rapidity muons. The calorimeter trigger uses all of the ATLAS calorimeters, but with reduced

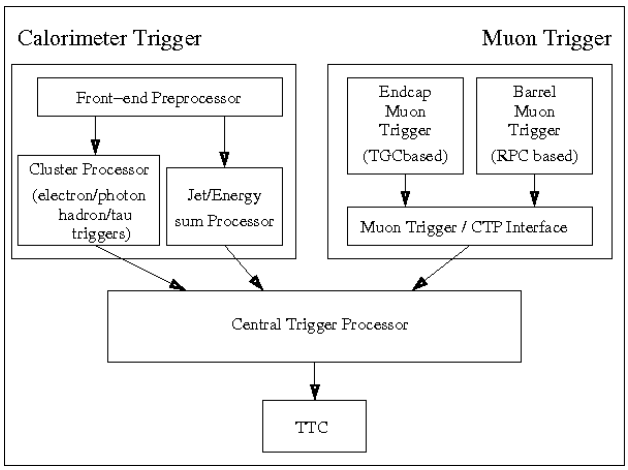

Figure 2.24. *Schematic view of the LVL1 trigger.*

granularity. The calorimeter trigger searches for electromagnetic clusters, jets and large missing and total transverse energy. Electromagnetic clusters are characteristic of high-p_T electrons and photons. An isolation cut can be required for electromagnetic clusters. For all objects a number of p_T thresholds can be defined.

The data from subdetectors are passed to the processors of the muon and calorimeter triggers. These are purpose-built hardware processors, with a fixed set of algorithms with programmable parameters. The processors work independently and in parallel to summarise the event in terms of the objects previously mentioned.

The features from the muon and calorimeter processors are passed to the central trigger processor which is responsible for the overall trigger decision based on the trigger menu. As previously mentioned, at this stage Regions Of Interest are identified and used to seed the LVL2 algorithms. The size of the LVL1 menu (i.e. the list of all possible LVL1 trigger items) is limited to 1024 because the LVL1 decision is written in a 1024 bit word.

The HLT front-end is designed to accept 75 kHz of LVL1 triggers with the possibility to reach 100 kHz in the scenario of a relaxed requirement on the LVL2 dead time. The target rate of LVL1 triggers is 40 kHz, allowing a safety factor of 2 with respect to the design output rate. It will be dominated by background physics processes such as jet faking isolated $e/\gamma/\tau$, and muons from $b/c \rightarrow \mu X$ or decay in flight of light mesons.

An important requirement on the LVL1 trigger is the ability to identify the bunch crossing of interest. This is particularly challenging due to the short bunch crossing period (25 ns). For the muon detector, because of its size, the time for a muon to traverse the whole detector is of the order of the bunch crossing period. For the calorimeter detector, the challenging comes from the possibility that pulse extends over several bunch crossings. The latency time taken to form and distribute the LVL1 trigger decision should be kept to a minimum in order to keep the length of the pipeline memories as short as possible, reducing costs and increasing reliability. The maximum allowed LVL1 latency is 2.5 μs and the target latency is 2.0 μs that ensures a 500 ns safety margin.

In addition to the detector data arriving and decision messages leaving the LVL1 trigger, there are several signals related to the accelerator which are used by the LVL1 system. The LVL1 trigger processors are synchronous with the 40 MHz LHC clock. Another signal coming from the machine system is the bunch-zero signal. This identifies one bunch in the machine and is set every time that the bunch completes one turn of the machine (88 μs period). The bunch-zero signal is used to identify the bunch crossing number in the machine.

2.3.2 The High Level Trigger

The High Level Trigger system [64, 65, 66] is composed by the LVL2 trigger and the Event Filter. Although they will both be built using farms of standard PCs interconnected by Ethernet networks, they differ in several important aspects. The LVL2 is designed to allow high rejection power using fast and limited precision algorithms which require modest computing power. Higher precision algorithms using more extensive computing power and with lower rejection power operate at the EF level.
The overall framework of the Event Selection Software (ESS) in which they operate has been designed in such a way that all the algorithms may be developed in the same offline development environment and have the same data-interface definitions. This approach has the major advantage of having a high degree of development commonality and flexibility of scope across the spectrum of HLT and the offline, as well as facilitating performance comparison.

LVL2

The LVL2 trigger uses RoI information, provided by LVL1 via the RoI Builder (RoIB), to request relevant event fragments from the Read Out System (ROS). Using these data, it produces a decision on the event and delivers the decision, together with data it has produced during its algorithmic processing, back to the Data Flow Manager (DFM). The RoIB receives LVL1 information for each LVL1 trigger, for this reason it runs at the rate of LVL1 trigger. The RoIB allocates a LVL2 Supervisor (L2SV) which assigns a LVL2 Processor (L2P) to process the event and forwards the LVL1 information provided by the RoIB to a LVL2 processing unit (L2PU). The L2PU, using LVL1 information, requests event fragments from the ROS, processes the RoI data,

and makes a decision to accept or reject the event. The L2PU can flag for accepting events that have been in fact rejected by the algorithm processing. This would be done in order to monitor the LVL2 selection process. The L2PU may also effect any required prescaling of selected channels. The final accept/reject decision is sent back to the L2SV. If an event is rejected, the decision is passed to the ROS via the DFM in order to remove the event from the ROBs. If an event is accepted, the decision is forwarded to the DFM, which then initiates the event-building operation for the event.
When the LVL2 system is not in use, for example during a detector calibration run, the DFM provides a LVL2-bypass mechanism. It is informed when new events are available for building directly by LVL1 CTP or the Local Trigger Processor of the detector being calibrated, via the TTC network.

Event Builder.

Events accepted (or flagged as accepted by a "Forced Accepted" request) by LVL2 are fully assembled and formatted in the Event Builder destination nodes, the Sub Farm Inputs (SFIs). For each accepted event the DFM, according to load-balancing algorithm and other selective allocation considerations, allocate an SFI. The SFI requests and receives the event data from the ROS then builds and formats the event in its memory. It notifies the DFM when a complete event has been built correctly or otherwise when expected event fragments are missing. In the latter case, the SFI attempts corrective actions, by trying re-access the missing fragments. The SFI can build more than one event in parallel. A switching network, the Event Builder Network (EBN) component, links ROSs, SFIs and the DFM. The network enables the building of events concurrently into all SFIs at an overall rate of a few kHz.

Event Filter.

The EF comprises a large farm of processors, the Event Filter Processor (EFP) components. Each EFP deals with complete events served by the SFIs, as opposed to the selected event data used by LVL2 trigger. From the architectural point of view the EF is a general computing tool for the analysis of complete events.
Each EFP runs an EF data flow control program (EFD) that receives built events from the SFIs. Several independent Processing Tasks (PTs) continuously process events allocated to them on demand by EFD. Using offline-like event reconstruction and selection algorithms, the PT processes the event and produces a final trigger decision. When a given PT has completed the processing of an event, it requests a new one to be transferred from an SFI via the EFD. If the event is accepted, the data generated by the PTs during processing are appended to the complete raw event by the EFD. Accepted events are classified and moved to respective Sub Farm Output buffers (SFOs), where they are written into local disk files. Completed files are accessed by a mass storage system for permanent storage. The EFDs may also send events to one of several parallel SFO output streams for further dedicated analysis, e.g. express analysis, calibration, or debugging.

HLT algorithms

The task of the HLT algorithms is to analyse Raw Data and reconstruct parts of the event according to the guidance from LVL1. The LVL1 RoI-based approach implies data-driven event reconstruction. Any HLT algorithm can be executed several times per event, once for each RoI. The first task of the HLT algorithms is the **Data Preparation**, which converts the Raw Data into objects that are used as input to reconstruction. Raw Data are converted in

Raw Data Objects (RDOs) and Reconstruction Input Objects (RIOs). The second type of HLT algorithms are the **Feature Extraction Algorithms** (FEX), which process abstract Features and Trigger Related Data, producing new types of Features, just like happens in the offline reconstruction. However, in the trigger, RoI objects are used to restrict the processing to geometrical regions of the detector (in average about 10% of the full event data are processed). The FEX use the RIOs, but in some cases, like for the Muon Spectrometer chambers, it was found an expedient to use in part RDOs as input for the HLT muon-selection. In the HLT the reconstruction is implemented using the so called 'seeding mechanism'. The seeding mechanism is driven by the Steering, which uses abstract objects called Trigger Elements (TEs). **Hypothesis Algorithms** can be inserted after each FEX, they validate the physics interpretation by the label of the TE based on the reconstructed Feature. Each FEX creates an output TE, which is linked to the input TE by a 'seeded by' relation. The Steering allows the TEs navigation, so that all the algorithms that process the RoI can access to the data used at the previous steps.

Computing resources.

LVL2 and EF processors will be normal rack-mounted PCs (4.0 GHz of CPU clock and 8 Gbyte of RAM memory) running Linux. It is estimated that there will be ∼500 LVL2 processors and ∼1600 EF processors in the final system, but initial setups during commissioning and for the initial data taking will be much smaller. Computing performance are more important than Input/Output (I/O) capacity in the EF nodes.
The EB requires a large CPU capacity to handle the I/O load and the event assembly. Roughly 90 rack-mounted PCs running Linux and provided with a

second Gigabit Ethernet interface that connects the SFI to the EF network are envisaged for the final EB system. About 30 PCs with large disk space (larger than 1 Tbyte) will be used as SFOs.

Chapter 3

Muon Identification and Trigger

3.1 Muon identification and measurement

The Muon Spectrometer [35] of the ATLAS experiment provides a standalone muon identification and measurement with typically three tracking stations in the toroidal magnetic field.

The global efficiency is close to 1, with the exception of the very high-p_T region (above 500 GeV/c) where catastrophic energy loss and muon showering can disturb the pattern recognition and lead to an efficiency of 95% approximately. Below 6 GeV/c, the muon energy loss in the calorimeter is of the order of its initial energy so that frequently the muon track is not sampled by all the three measurement stations of the Muon Spectrometer. In general, the reconstructed muon can be backtracked to the interaction region through the calorimeter, corrected for its estimated or measured energy loss, and combined with its inner detector track in order to improve the momentum resolution for p_T below 50 GeV/c.

The off-line packages Muon Object Oriented REconstruction (*MOORE*) [67] and MuonIdentification (*MuId*) [68] have been developed in ATHENA, the official software framework of the ATLAS experiment for the purposes of standalone and combined muon reconstruction and identification, fully compliant with common Event Data Model (EDM) prescriptions which aim to make as homogeneous and general as possible the set of reconstruction objects used by all tracking softwares in the experiment. The latest version of MOORE is able to incorporate different pattern recognition approaches thanks to a high degree of code modularity and the use of common EDM classes and reconstruction steps. These two packages, developed in the ATLAS offline environment, have been adopted ad optimised to work inside the trigger framework (at the Event Filter) as will be discussed in Sec. 3.3.

3.1.1 MOORE

The MOORE (Muon Object Oriented REconstruction) algorithm reconstructs tracks inside the Muon Spectrometer, starting with a search for regions of activity within the detector, and subsequently performing pattern recognition and track fitting. The final reconstructed objects are tracks whose parameters are expressed at the first measured point inside the Muon Spectrometer. The bending power of the toroidal magnetic field in the (x, y) plane is negligible almost everywhere in the detector, so a track can be approximated to a straight line in the plane transverse to the beam line plane, allowing the construction of patterns, that are essentially vectors of digits measuring all the same ϕ coordinate within resolution. The tracks crossing the ATLAS Muon Spectrometer bend in the (r, z) plane. Nevertheless in this plane a crude pattern recognition can be applied locally (in every station) assuming the tracks to be straight lines and approximating the precision mea-

surements, e.g. for a Monitored Drift Tube (MDT) module the tube centre is used to approximate the hit position at the early stage of pattern recognition. These approximations allow to construct track segments in (r, z) using the same procedure that is used to construct patterns in the (x, y) view, i.e. by looking for clusters of hits at approximately the same value of θ, the polar angle. The (r, z) patterns are subsequently refined by later phases of the pattern recognition. The refinement is restricted only to patterns that have a corresponding element in the (x, y) plane in order to optimise the time latency of the algorithm. For each precision hit a drift circle is defined, with radius equal to the drift distance. For each pair of precision hits (one in each multilayer), the four tangential lines are found. Then, a track segment is built adding one by one all the hits having a residual distance from the line smaller than a given cut. The selected precision hits are fitted linearly and the segment is kept if it is successfully fitted, if it has a number of hits above a cut and if it points to the interaction vertex. This track segment is referred as a road. The use of hit information coming from the trigger chambers in order to guide the reconstruction in the precision chambers allows the restriction of the number of track segment candidates in the high background environment of the precision chambers. The tracks produced by MOORE have the parameters expressed at their first measured point (hit on the track) in terms of perigee parameters. In the final step of the fitting procedure, a looping procedure over all the roads, allows to assign to each road the hits from layers without trigger chambers. After having assigned hits from all the muon layers to a track, the track fit takes into account energy loss and Coulomb scattering effects. Finally, a cleaning procedure is performed to remove hits with high residuals.

3.1.2 Muid

The MuId (Muon Identification) package associates tracks reconstructed by MOORE in the Muon Spectrometer with the corresponding Inner Detector tracks as well as with calorimeter information. The final objects are identified muons whose track parameters are expressed at the interaction point. The purpose of MuId is to identify muons among the Inner Detector tracks, to obtain improved parameter resolutions at moderate momenta from 20 GeV/c up to 100 GeV/c, and to clip the tails of badly measured high momentum muons (such as those resulting from catastrophic bremsstrahlung and the pattern recognition errors caused by showering in the Muon Spectrometer). The first step (**MuId Standalone**) is to extrapolate the Muon Spectrometer track up to the beam line and to express its parameters at the production vertex. The traversed calorimeters are represented by five additional parameters, namely two scattering angles (each in the longitudinal and transverse plane) and an energy loss parameter. Two scatterers are sufficient to give deflected position and direction distributions (plus correlations) at the Muon Spectrometer entrance consistent with the simulation. The energy loss measurement (with error) is obtained either from the observed calorimeter energy deposition or from a parametrisation. In the next step (**MuId Combined**), tracks are matched by forming a χ^2 with five degrees of freedom from the difference between the five track parameters of the track and their summed covariance matrix. The Inner Detector and standalone fits are used for this. To obtain the optimum track parameters, combined fits are performed to all matches with χ^2 probability above 10^{-4}. A combined fit is a refit to all the measurements and scatterers from the Inner Detector, calorimeter, and Muon Spectrometer systems. When no matches satisfy the above criterion, a combined fit is attempted for the best match within a road around the

standalone track. Finally, all matches to the Inner Detector giving a satisfactory combined fit are retained as identified muons. The MOORE/MuId procedures provides the optimal track-parameter measurement expressed at the interaction region as well as the probability representing the compatibility of the track combination with a muon hypothesis. Ambiguities and low-probability matches are retained such that harder cuts can be applied as appropriate during physics analysis.

3.2 The Muon Trigger System

The Muon Trigger data flow is sketched in Fig. 3.1. The LVL1 emulation has been essential, in the past, in order to define the Coincidence Windows (discussed later in 3.2.1) and to optimise the logic to be implemented in the LVL1 electronics. Nowadays it is used to assess the expected trigger efficiencies and resolution and to study non-standard trigger configurations (like cosmics or very low-p_T triggers). The LVL2 has two different operating modes: for "high-p_T physics" and for "B-physics triggers" (as shown in Fig. 3.1). The LVL2 algorithms use data from the Muon Spectrometer, the Inner Detector and the Calorimeters.

The Event Filter performs its selection starting from the muon reconstructed in the MS, then the Calorimeters measurement is used to correct for the energy loss and propagate back to the Impact Point (IP), where a matching with a reconstructed ID track is required.

The LVL1 and LVL2 Muon Trigger Levels will be analysed in next subsections. The Muon Event Filter is described in more detail in Section 3.3.

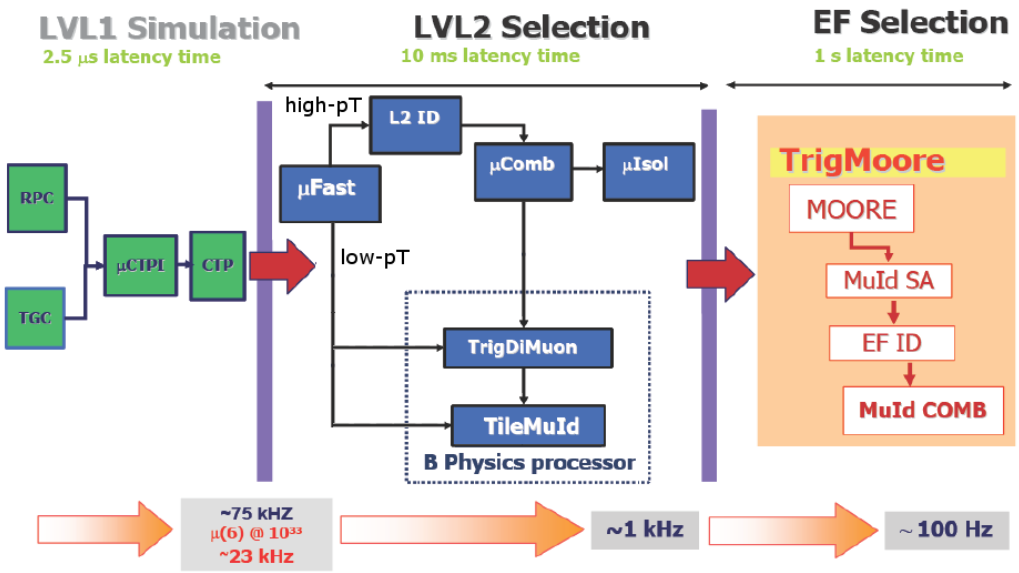

Figure 3.1. *Block diagram of the muon trigger structure, reporting algorithms/packages for each one of the three levels. In particular are represented the LVL1 simulation, the main FEX algorithms and the requirements in terms of rate reduction and latency time.*

3.2.1 The Level-1 Muon Trigger

Barrel. The Level-1 muon trigger in the barrel ($|\eta| < 1.05$) region of the ATLAS Muon Spectrometer is based on the use of Resistive Plate Chambers (RPC) as trigger detectors. The basic principle of the Level-1-RPC algorithm is the selection of events with muons having a large p_T coming from the interaction vertex. The algorithm works in the following way: If a hit is found on the second RPC layer (RPC2, *pivot plane*) a search for hits is made on the other layers (RPC1 and/or RPC3) within a geometrical road, named Coincidence Windows (CW), whose centre is defined by the line of conjunction of the hit in the RPC2 and the interaction vertex (see Fig. 3.2). Muon tracks are deflected under the action of the toroidal magnetic field thus

the track distance from the centre of the Coincidence Windows is mainly a function of the p_T. The higher is the p_T the smaller is the distance. In this way the algorithm selects only muons with a p_T greater than a certain value. The ATLAS physics benchmark [69] has suggested two threshold regimes for muon triggers:

- Low-p_T trigger: it analyses data coming only from the first two RPC stations (RPC1 and RPC2). In particular this regime maximises the B-physics trigger capabilities in the context of a possibly reduced initial Trigger and Data Acquisition (DAQ) system [70].

- High-p$_T$ trigger: it operates only in presence of a low-p_T trigger requiring the spatial coincidence with the RPC3 station. This regime is specialised for heavy objects search.

Although the algorithm is more selective in the bending plane the same selection scheme is also applied in the azimuthal plane to reduce accidental coincidences. Moreover to cope with background from low-energy particles in the experimental hall [71], a 3/4 or 4/4 majority coincidence of the four possible hits in the first two RPC doublets has to be required (low-p_T trigger) and 1/2 or 2/2 of the hits in the outer RPC station (high-p_T trigger). Only when trigger conditions are satisfied for both views, a valid trigger signal is generated. The basic module in the trigger logic electronics is the PAD. Signals coming from the first two RPC stations are sent to the low-p_T PAD boards. Almost all the relevant functions needed for the barrel trigger algorithm are performed by dedicated processors the Coincidence Matrix ASIC (CMA) [72].
The low-p$_T$ CMAs receive $(32 \times 2) \times (64 \times 2)$ input signals from four RPC layers (two from the pivot plane and two from the RPC1 plane). The CMA

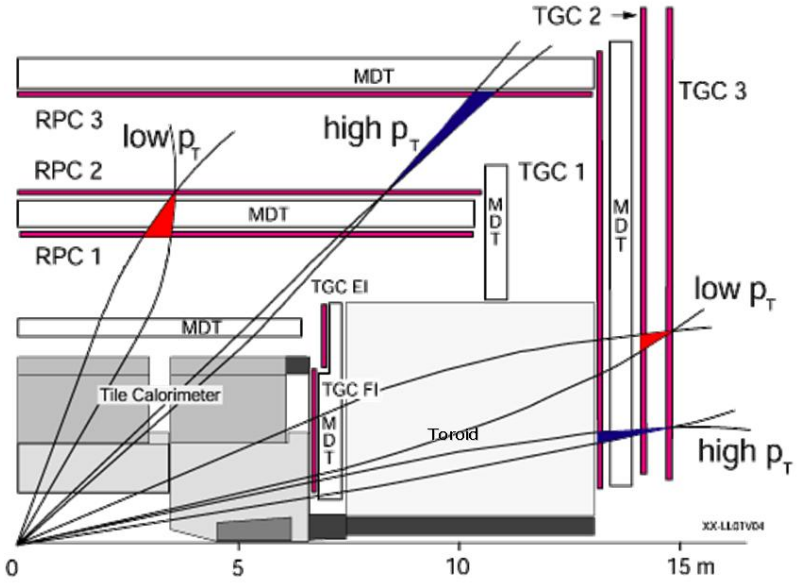

Figure 3.2. *Longitudinal view of the ATLAS trigger detector together with low-p_T and high-p_T trigger Coincidence Windows in barrel and endcap regions.*

boards align in time the RPC input signals, perform preprocessing logic (declustering algorithm, majority logic) and apply the geometric coincidence logic.

Data coming from four CMAs (two η-CMA and two ϕ-CMA) are collected in a single PAD board which performs the RoI logic defining the associated ROI as the overlap of the η and ϕ activated CMAs. These information are transferred to the corresponding high-p_T PAD boards which performs the high-p_T algorithm using the low-p_T trigger results and the signals coming from RPC3 station. The overall results are sent to the off-detector electronics via an optical link transmitter (Fig. 3.3).

End Cap. The technology of Thin Gap Chamber (TGC) is used for the level-1 muon trigger in the end-cap region ($1.05 < |\eta| < 2.4$), which has simi-

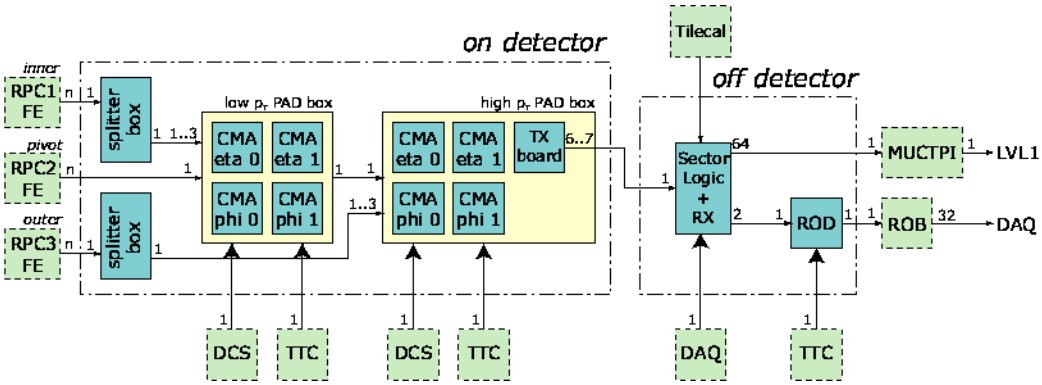

Figure 3.3. *LVL1 Trigger system: Front-end RPC signals go to the PAD boards (each one hosting four CMA).Trigger results and readout data are sent to the off-detector electronics via optical link for readout and trigger data processing.*

lar structure to MWPC with two-dimensional readout from anode wires and cathode strips to determine η and ϕ coordinate respectively. The chambers are assembled as three big wheels and one small wheel on each side. The detector layout is shown in Figure 3.4-(a). The schematic diagram of the trigger scheme is shown with red arrows in Figure 3.4-(b). The trigger logic is based on the hit coincidence between the triplet layer (M1), in the big wheel, closest to the IP, and both doublet layers (M2 and M3). The coincidence operation is taken at three points. The on board electronics (PS-board) implements, in a SLB ASIC, a 2/3 coincidence in the M1 station and, independently, a 3/4 coincidence with the M2 and M3 stations. Bunch-crossing-ID are assigned to wire and strip signals at this stage. Then, these information from SLB ASICs are sent to the High-p_T Boards and the coincidence between three stations is taken. Finally, the Sector Logic boards make a track by combining η and ϕ information from High-p_T boards, in time coincidence and estimate the p_T via look-up-tables. Two highest p_T tracks for each trigger sectors are selected and sent to MuCTPi as track candidates. The data from EI/FI stations are

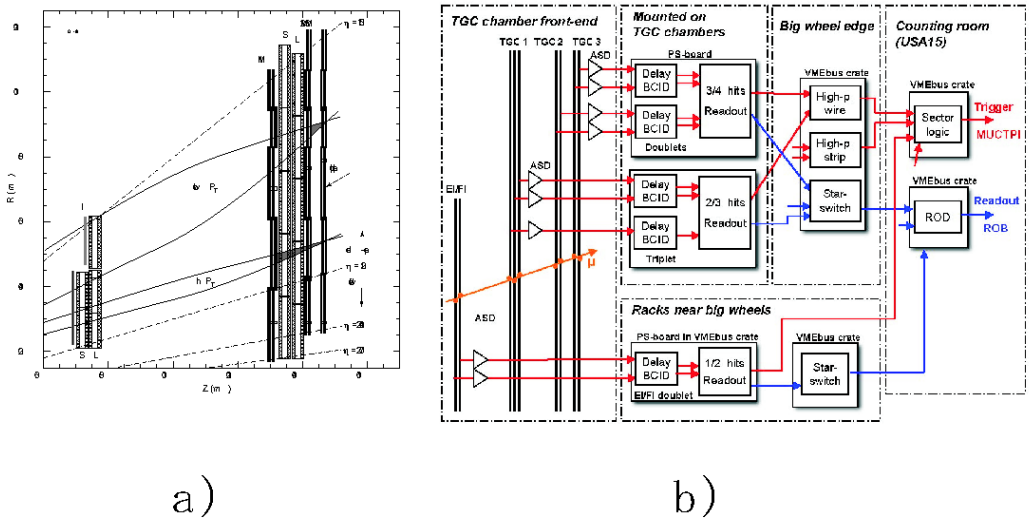

Figure 3.4. *(a) Longitudinal view of the TGC detector layout together with low-p_T and high-p_T trigger window. The M1 station is the triplet closest to interaction point and the M3 station is referred as pivot plane. (b) The overview of the TGC Level-1 trigger scheme.The red line shows data flow of trigger path and the blue one represents the readout path.*

also sent to the Sector Logic boards but are not used in the trigger decision. By default, **coincidence of three stations** is required in the muon end-cap trigger system even with low-p_T threshold.

The distance of the muon track from a straight line (the infinite momentum track) due to the bending magnet is related to the muon transverse momentum. The p_T estimate is done by look-up-table requested on the Sector Logic boards, and it is configurable according to the requirement of the physics target, run condition, etc. The window size for for each p_T threshold is defined according to simulations and the optimised table is prepared for each Region-of-Interest (RoI) whose size is $\delta\eta \times \delta\phi \sim 0.03 \times 0.03$. The narrow

size of RoI is due to non-uniform magnetic field in the end-cap region, which requires different optimal window size for each region.

3.2.2 The Level-2 Muon Trigger

The role of the Level-2 is to confirm muon candidates flagged by the Level-1 and to give precise physics quantities associated to the muon candidate (feature extraction). The muFast algorithm performs a standalone feature extraction using the MS data; the Hypothesis Algorithm associated to muFast provides the p_T-cuts for a first reduction of the Level-1 rate. The muFast Trigger Element is passed to muComb, which refines the measurement using the additional data provided by the Inner Detector. Also muComb is followed by an Hypothesis Algorithm which requires the p_T-cut.

MuFast in the barrel

For each RoI flagged by the RPC trigger, it performs first a global pattern recognition, then a loose track fit in each station and, finally, a fast p_T estimate.

The global pattern recognition is designed to select clusters in MDT chambers belonging to a muon track: the RPC pattern recognition is seeded by the LVL1 RoI, then the MDT pattern recognition starts from the track segment that connects the RPC clusters. Around each segment a muon road is opened and the hit tubes are collected according to the position of the sensitive wire (see Fig. 3.5). The roads opening ($\sim$ 20 cm) is optimised to guarantee 96% of efficiency for the hit finding. Background hits are removed using a contiguity algorithm: it computes recursively the mean position of the track cluster and removes the tubes having the highest deviation from

the mean.

The track fit approximates the muon track with straight line segments in each MDT chamber. Using the drift time measurement and an approximated space-time ($r - t$) relation, a track segment is built (see Fig. 3.6) if at least four MDT hits (two per MDT multilayer) can be used. The left-right ambiguity with respect to the sensitive wire is solved by computing all the possible combinations of segments and choosing the one with the best χ^2 . The fitted segments provide a precision measurement of the "super point" where the fitted line crosses the middle of the MDT chamber.

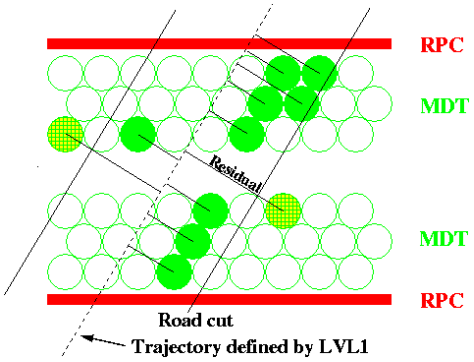

Figure 3.5. *Muon road defined around the LVL1 trajectory. The hit residual are used to discriminate signal hits against background.*

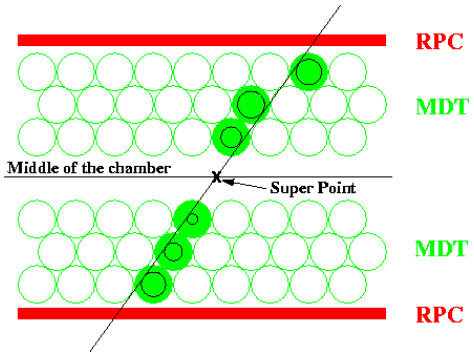

Figure 3.6. *Tracks inside the MDT chambers are fitted using the drift time measurement and an approximate space-time relation.*

The fast p_T estimate uses the track bending, measured through the sagitta (s_m) (Fig. 3.7, which is computed from the three super points. The muon transverse momentum is estimated using an inverse linear relationship between the measured sagitta and p_T : $s^{-1} = A_0 \cdot p_T + A_1$. This relation is valid for tracks originating at the nominal interaction point. The A_0 parameter is related to the setup of the spectrometer (magnetic field, lever arm) while the A_1 parameter takes into account the energy loss in the calorimeter.

This function has been mapped into a Look Up Table (LUT) by dividing the detector region in η and ϕ bins (Fig. 3.8).

MuFast in the end-caps

For RoIs flagged by the TGC in the Endcap regions, a different algorithm is employed due to the more complex magnetic field map. muFast, in this case, uses a global pattern recognition and a fast p_T estimate. The Global Pattern Recognition is initiated from the TGC pattern recognition in the middle station (TGC2 station). Then, the MDT pattern recognition in the middle station is performed using the TGC pattern-recognition result as a seed. The same algorithm used for the Barrel region is applied also here. When the muon road reaches the MDT outer station, the MDT pattern recognition is also performed in the outer MDT chambers. The track bending is measured through the angle α, which is defined as the angle between the direction of the track segment reconstructed in the muon chambers and the direction obtained by connecting the nominal interaction vertex and the mean hit position in the muon chambers. The muon transverse momentum is estimated using an inverse linear relationship between the measured α and p_T : $p_T^{-1} = A_0 \cdot \alpha + A_1$. This function has been mapped into a LUT by dividing the detector region in η and ϕ bins. To obtain the best estimate of α and hence p_T , the α variable is calculated using both middle and outer MDT stations whenever hits are found in the outer MDT station. If there is no hit found in the outer MDT station, first, α is calculated by using TGC pattern recognition in the middle station and p_T is calculated accordingly. Then, if p_T is found to be high enough, the MDT pattern recognition in the middle station is used to refine p_T calculation.

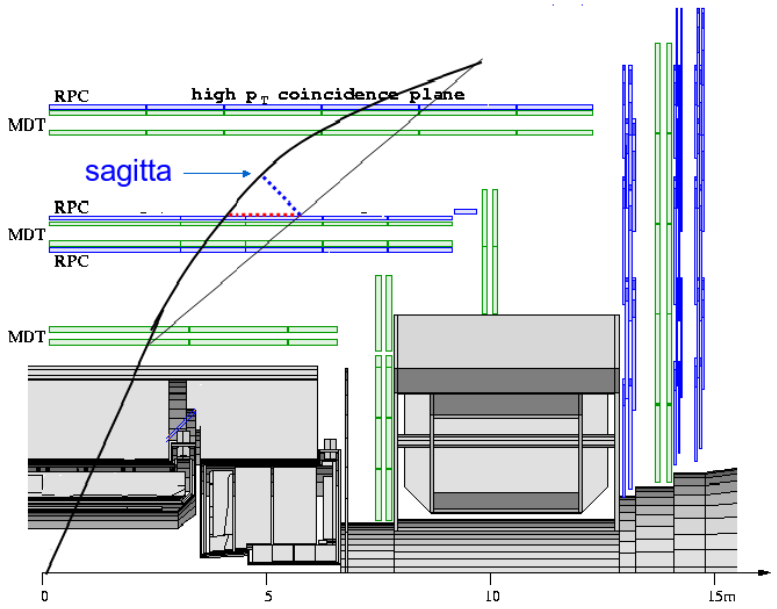

Figure 3.7. *The sagitta is measured using the track reconstructed from the three segments in the MDT chamber.*

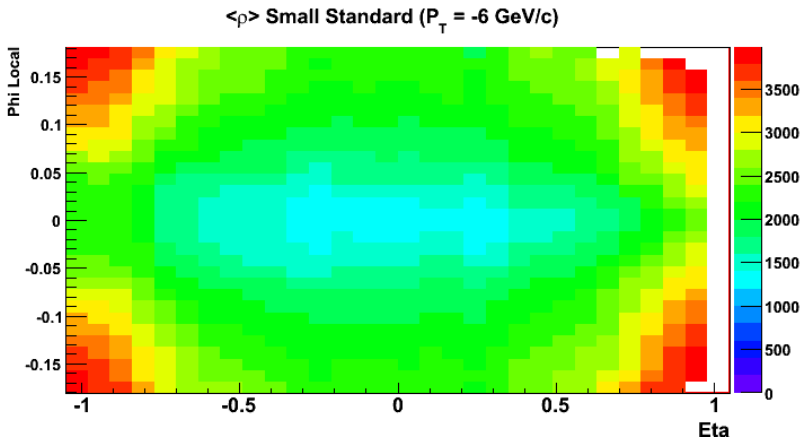

Figure 3.8. *Look Up Table obtained using muon samples of fixed transverse momentum $p_T = 6$ GeV.*

MuComb

The muComb algorithm matches the track seeded by muFast to Level-2 ID tracks. Firstly, it searches all the ID tracks with spatial matching, then selects the track with best p_T matching. In reconstructing the Level-2 ID tracks, TRT is not used due to the tight constraint on processing time.
The pre-selection utilises the differences in η and ϕ directions between muFast and ID tracks. Moreover, the difference in the z position at a radius of the Barrel Calorimeter surface extrapolated between from the muFast and ID tracks is used. Then, for each of the pre-selected ID tracks, a combined p_T is evaluated together with the information of the muFast track. The combined p_T is calculated as a resolution weighted average of the p_T measured in the two subdetectors. A χ^2 is calculated in this p_T combination, and the ID track which gives the minimum of such χ^2 is selected as the best matching candidate.

MuIso

The rejection of muons from heavy flavors and in-flight decay of light mesons at the second level of the Atlas trigger system cannot be efficiently achieved using standard trigger algorithms like muFast and muComb, because is characterised by real muons originating near the interaction point. Different signatures have then to be exploited in order to keep the background rates at an acceptable level. One of the most striking difference of muons from pions, kaons and b/c decays and muons coming from heavy object decays is that the former are mostly produced inside jets, while the latter are often not surrounded by other particles, except for those from pile-up collisions. This has motivated the development of criteria for discriminating between isolated and non-isolated LVL2 muon candidates, by looking at differences in the en-

ergy patterns released in the electromagnetic and hadronic calorimeters.
In order to get adequate rejection power and fulfil at the same time the constraints of available time and data bandwidth, the reconstruction of the calorimetric quantities and the rejection of unwanted events in the trigger chain should be as fast as possible $O(10)$ ms. To minimise the latency related to the muon combinatorics the LVL2 muon isolation algorithm (muIso) can be seeded either by trigger elements from the muFast algorithm, or from the ones provided by the muComb algorithm . At the same time access to the calorimetric information has been implemented by using the optimised fast access used by default in the LVL2 e/γ trigger slice.
The full algorithm consists of two consecutive logical steps: the feature extraction algorithm step (muIso), and the hypothesis algorithm step (MuisoHypo). The algorithm decodes LAr and Tile calorimeter quantities (i.e. transverse energy deposit or sums of calorimetric cells above a predefined energy threshold) in cones centred around the muon direction. The geometrical definition of these cones is given by the condition $\Delta R < \Delta R_{CONE}$, where $\Delta R = \sqrt{\Delta\eta^2 + \Delta\phi^2}$, and $\Delta\eta$, $\Delta\phi$ are the distances in pseudorapidity and azimuthal angle between the calorimetric cell and the cone axis. Since the muon itself contributes to the energy deposit inside the cone, to improve the discriminating power of the isolation algorithm, two different concentric cones are defined: an internal cone chosen to contain the energy deposit released by the muon itself, and an external one, supposed to include contributions only from detector noise, pile-up and jet particles if present. The reconstructed information are then stored in an IsoMuonFeature container.
The hypothesis algorithm, MuisoHypo, accesses the IsoMuon feature in the event record and applies selectable requirements on isolation based on various electromagnetic and hadronic calorimetric quantities. In the current

implementation of the algorithm it is possible to apply cuts on the transverse energy deposit in the inner cone and outer ring of the two calorimeters, on the energy sum of calorimetric cells in the inner cone and outer ring of the two calorimeters, and on the isolation variable defined as the ratio of the transverse energy released on the inner cone divided by the one released on outer cone. The isolation requirements can also be parametrised as functions of p_T and/or η, if needed, in order to guarantee a flat efficiency in transverse-momentum and pseudorapidity.

3.3 The Muon Event Filter (TrigMoore)

Algorithms functioning as Event Filter [73] should not operate only in a general purpose or exclusive mode, but they must retain the possibility of working in seeded mode, processing the trigger hypotheses formed at a previous stage in the triggering process. The HLT algorithms working in seeded mode typically need to access the event data that pertains to a region in ($\Delta\eta$, $\Delta\phi$) around the centre of a Region of Interest. For this need the algorithm must use the RegionSelector tool [74] that allow to select the Region to be accessed by the data. The software for the Event Filter has been implemented in the package TrigMoore [75] and allows the execution of Moore and MuId in the trigger environment. They can run in **full scan mode**, accessing the entire event, like the off-line package, or in **seeded mode**, accessing only the data inside the Region of Interest. In fact, in seeded mode the EF algorithms can access only the data from the chambers in the detector region provided by the RegionSelector.

The seeding in TrigMoore can be provided either from LVL1 or LVL2. In particular, the full chain: "LVL1 simulation → LVL2 → Event Filter" has

been integrated and tested within the HLT steering. In the sequence of the HLT, TrigMoore is called with a trigger element produced by the previous level as input parameter. From the trigger element it is possible to retrieve information about the Region of Interest. The RoI contains, among other information, its position in η and ϕ, and the algorithms use the RegionSelector to know the chambers that can be found in a certain region ($\Delta\eta$, $\Delta\phi$) around the centre of the RoI. The RegionSelector returns the list of detector elements that are contained within the region. Only these elements will be accessed from the seeded algorithms.

3.3.1 Muon Trigger configuration

The LVL1 signatures, or trigger items, are combinations of requirements (or trigger conditions) on the multiplicities of various kinds of candidate objects delivered by the muon triggers. There are several LVL1 items corresponding to different p_T thresholds that have been studied and are typically considered for the trigger menus:

- MU0, MU4, MU5, MU6, MU8, MU10 for the low-p_T selection;
- MU11, MU20, MU40 for the high-p_T selection.

The naming scheme indicates, along with the lepton selected, the nominal p_T threshold applied. The hardware LVL1 can implement a maximum of three low-p_T and three high-p_T thresholds. The "MU0" threshold represents a LVL1 configuration with completely opened coincidence windows; it is also called "Cosmic" threshold as it can be used for cosmic trigger during the detector commissioning phase. The opening of the Coincidence Window is limited by the cabling connectivity thus the MU0 threshold does not indicate

the real p_T cut applied, which is higher than zero. Muon High Level Trigger algorithms start from the RoI delivered by the LVL1 trigger and apply trigger decisions in a series of steps, each refining existing information by acquiring additional information from muon detectors. A list of physics signatures, implemented in the event reconstruction and selection algorithms, are used to build signature and sequence tables for all HLT steps. This stepwise and seeded processing of events is controlled by the HLT steering. FEX algorithms, typically, request detector data from within the RoI and attempt to identify muon features. After processing, each FEX algorithm updates the RoI position if it has been determined more accurately. Subsequently, a hypothesis algorithm determines whether the identified feature meets the criteria necessary to continue. Each signature is tested in this way. The decision to reject or keep the event is based on the validity of signatures, taking into account pre-scale and pass-through factors. Thus events can be rejected early after an intermediate step if no signatures remain viable. At present, three muon hypothesis algorithms are implemented in the HLT flow: **MufastHypo**, **MucombHypo**, and **TrigMuonHypo**.

For every LVL1 muon candidate passing the LVL1 selection, the muFast algorithm is run first followed by its hypothesis algorithm, MufastHypo. Then tracks are reconstructed around the muon in the Inner Detector with the SiTrack and IDSCAN algorithms. The tracks reconstructed separately by muFast and in the Inner Detector are combined by the muComb algorithm, followed by its hypothesis algorithm MucombHypo. When requested by the trigger menu, the LVL2 muon selection chain can be completed by more algorithms and hypothesis tests, as, for example, muIso.

The Event Filter processing starts by reconstructing tracks in the Muon Spectrometer around the muon found by the LVL2 algorithms. Separate instances of the TrigMoore algorithm, perform the reconstruction in the Muon Spectrometer and then reconstructed tracks are matched with the Inner Detector tracks reconstructed by iPatRec [76, 77] (as explained in more detail in Sec. 3.1.1).
The hypothesis algorithms include the definition of a set of HLT trigger thresholds, that will be treated in detail in Sec. 3.3.2. The definition of the effective trigger thresholds will be given in full detail in Sec. 4.2.2.
The results presented in this thesis, where not differently indicated, have been obtained using two different HLT configurations : the standard muon trigger chain, as defined for the Computing System Commissioning (CSC-06) and the special configuration for 900 GeV LHC operation (CSC-06-900GeV). In the standard configuration the trigger menu included the signature mu6l, mu6 and mu20. The HLT notation follows the LVL1 notation with the difference of using small letters for the items, instead of capital letters. The signature mu6l implements threshold cuts $p_T > 3$ GeV both at LVL2 and EF hypothesis algorithms (Fig. 4.17). The "900 GeV" configuration has a special LVL1 threshold set: MU6 and MU8 were replaced by MU0 (coincidence windows completely opened) and MU5. In this configuration the HLT signatures were set to mu0 (implementing threshold cuts as in mu6l) and mu5 ($p_T > 5$ GeV).

3.3.2 Event Filter Hypothesis Algorithms

The FEX algorithms, as described in Sec. 2.3.2, are designed to calculate the interesting physics quantities and not to operate the event selection. For this reason the trigger software allows the use of some special algorithms, the Hy-

pothesis Algorithms (HYPOs), which are deputed to the selection by means of the physics quantities provided by the FEX. Each HYPO introduces a decisional level in the trigger sequence, with the purpose of reducing as soon as possible the data to be processed by the following FEX. This strategy is particularly effective in reducing the overhead of the HLT.

The configuration of the muon trigger sequences and the implementation of the HYPOs at the Muon Event Filter has been performed in order to allow a fully functional selection. This effort in the trigger software development produced the ATHENA package *TrigMuonHypo*. Furthermore the TrigMoore package itself has required some development. It actually contains a single HLT Algorithm, MooHLTAlgo, which is directly run by the trigger steering. Originally MooHLTAlgo was running in sequence all the subalgorithms corresponding to the offline muon reconstruction in the MS (MOORE subalgorithm) and, later, the MuidSA and MuidCB algorithms. At that step a muon trigger element coming from LVL2 was directly leading to a final TE corresponding to combined muon tracks if validated by the entire EF chain. In order to introduce the probability to cut on reconstructed quantities, at each major step of the reconstruction (MS, SA, CB) a number of central flags have been introduced in order to allow the separate running of only some subalgorithms. Currently, the EF selection has been broken into three different steps, where each of the FEX is realised by a different instance of MOOHLTAlgo behaving according to the configuration. Moreover, the FEX configuration allows also to tune some parameters according to the trigger menu item being processed. For example, the geometrical opening of the RoIs have been configured differently for the 900 GeV trigger, aimed at maximising the acceptance at very low-p_T.

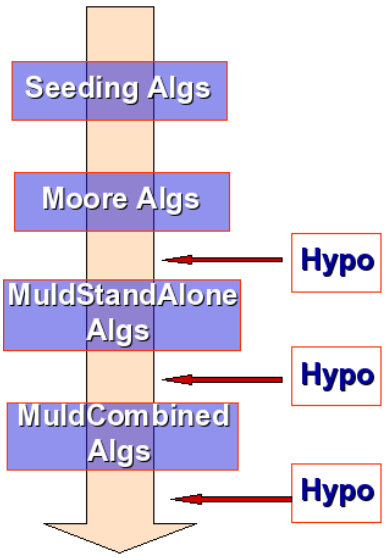

Figure 3.9. *Schematic view of FEX/HYPO structure of the muon Event Filter for the current implementation. The seeding algorithms can be chosen by the user. One Hypothesis algorithm follows each FEX algorithm.*

The physics program of ATLAS, in particular the search of new Physics, can benefit from "inclusive" triggers; for the muons they are mainly based on the search of high-p_T leptons which are expected from the decay of heavy particles. Thus, the first challenge of the Muon HYPOs is to cut on the muon p_T to isolate interesting events; furthermore track quality cuts can help to reject fake tracks from background hits.

The flexibility of the structure FEX/HYPO allows to add as many criteria as needed by the experimental environment and by the physics requirements. In the recent ATHENA releases (12.X.X, 13.X.X), the implementation of the HYPOs and the configuration of the trigger sequences at the EF is organised with the HYPOs applying p_T cuts after MuidSA and MuidCB.

In principle, after MOORE, the corresponding HYPO might operate a decision based on the quality of the MS tracks: the track χ^2, the hit multiplicity and the noise level inside the RoI, the number of precision hits of the track. The effect of such cuts is to reduce the fake track rate in high background conditions (which are described in more detail in Sec. 4.2.3). After MOORE, the track is extrapolated to the Interaction Point by MuidSA, the corre-

sponding HYPO can access its estimate of the transverse momentum and possibly apply a loose cut. The combination of the MS track with the ID track (MuidCB) guarantees a more sharp resolution on p_T and also the access to the χ^2 of the match between MS and ID tracks, and to the ID track parameters (e.g. the impact parameter and the number of hits for each layer of the ID). As will be shown in deeper detail later in Sec. 4.3.1, cuts on these quantities have been studied to reject the large physics background from light mesons in-flight decays and might be used in a more refined implementation of the hypothesis algorithm.

The exchange of information between FEX and HYPO algorithms and the possibility to re-run HYPOs during physics analyses for optimisation purposes require a correct implementation of the data model. In particular the FEX output quantities have to be served in the format of AODs (Analysis Object Data) designed to be controlled by the HLT steering (HLTInitialize, HLTExecute, etc.), while a standard offline ATHENA algorithm needs to implement the initialise, execute methods. At the moment, since the only cut applied at the level of hypothesis algorithm acts on the transverse momentum, a very light AOD object has been defined and used as output of each FEX step in the muon EF.

3.4 Muon Slice Validation

The maintenance of the software and its functionalities is crucial for the good operation of the trigger. Various and different configurations have been adopted by the Muon Slice during the past three years, requiring an extensive validation of the software functionality and performance. Three main validation strategies have been used:

- the *nightly* validation, which is based on the building of the entire ATLAS software and on some automatic tests performed every night;
- the extensive check of new software developments and of different slice configurations;
- the on-line monitoring, which is mainly designed to check the trigger operations on real data, but can be used on MC as a fast software validation tool.

The **nightly tests** are performed via a central facility, the *NICOS* (NIgthly COntrol Management) tool, which is a flexible tool for coordination of software development in large scale projects. It manages the multi-platform nightly builds based on the recent versions of software packages, identifies possible problems, and makes results immediately available to developers spread over different institutions and countries. The design strategy is driven by the requirements of flexibility, portability, and easiness of usage. NICOS performs nightly build processes in distinctive steps. Each step allows plug-ins and can be configured for particular use case. The compilation itself is one of the initial steps followed by tests, analysis of errors, and creation of web pages with build summaries. Developers are notified about problems with their packages via e-mail. Via this system it is possible to search for crashes and memory-leak, to make direct comparisons (with respect to the previous day results or to user defined reference files) of basic quantities (e.g. the number of triggered events for a given trigger item) after reconstruction of dedicated MC samples. An example of histogram produced during nightly tests is reported in Fig. 3.10.

Another automatic tool for validation which runs on a daily basis is the *Run Time Tester* (RTT). It is a Python-coded testing framework that can

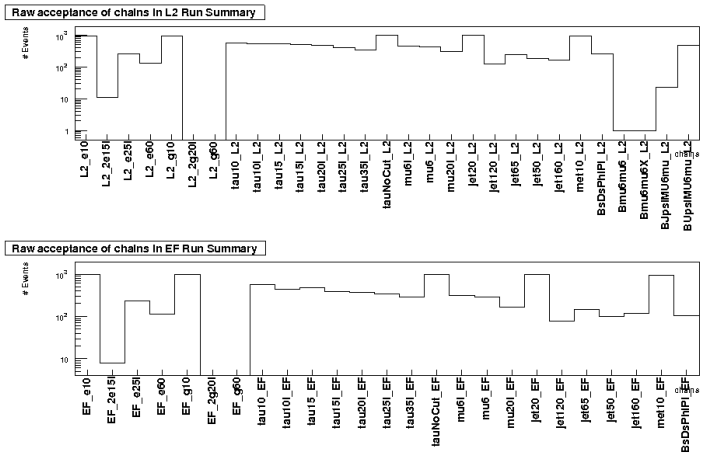

Figure 3.10. *Raw trigger acceptance evaluated for 1000 $t\bar{t}$ events using the monitoring tools. The entries of this histogram are checked in the nightly automatic tests to search eventual changes in the selection due to FEX modifications/errors.*

set up and run (both Athena and non-Athena) jobs in an automated manner, perform post-job actions and then report results to a web-accessible location. It can be run interactively on a Linux box (good for 1-2 short jobs), or automatically in batch. For example, it is possible to setup a job for running user defined trigger configuration, to automatically process the output of the job with analysis macros and extract summary results to be compared with some reference. It has some limitations in statistics because if a job is not completed in time is automatically killed.

In order to configure the Event Filter RTT jobs, some variables sensitive to trigger changes/errors have been identified:

- the trigger global efficiencies. They can be evaluated as a function of η or for the barrel and the endcaps separately, depending on the available statistics;

- the p_T resolutions (for single muons) for the EF algorithms as a function of η and ϕ;
- the χ^2 of the muon tracks for MOORE and MuidCB;

Extensive checks have been performed to study efficiencies, resolutions and track quality. They require high statistics and, as a consequence, huge efforts to run the trigger Muon Slice on data. They require also a good understanding of the Muon Slice and can benefit by cross checks with the offline reconstruction results. In Fig. 3.11 are reported resolution and efficiencies as a function of p_T for two different Athena releases.

They are mainly useful before and after a new release is built. Also data containing trigger results after reconstruction, centrally produced at CERN or using the GRID, are usually available before a new release is built. Furhermore private productions are also required to fully understand and study the implementation. An example of extensive study of the Event Filter in Athena release 12.0.6 is reported in Chap. 4.

The **on-line monitoring** is fundamental for the study of the selection on real data. It is based on the study of basic quantities, like track parameters and track quality. The variables monitored can be also useful to check "day by day" the software status and its new implementations. In Fig. 3.12 are shown the hit residuals for the different muon detector technologies, in Fig. 3.13 are reported the χ^2 for the EF tracks together with its probability, and in Fig. 3.14 the track parameters (η, ϕ, p_T) for each EF FEX

Some details on validated releases. During the last two years many new functionalities have been implemented in the Muon HLT. A short summary of these implementations, which have been extensively checked, will be presented.

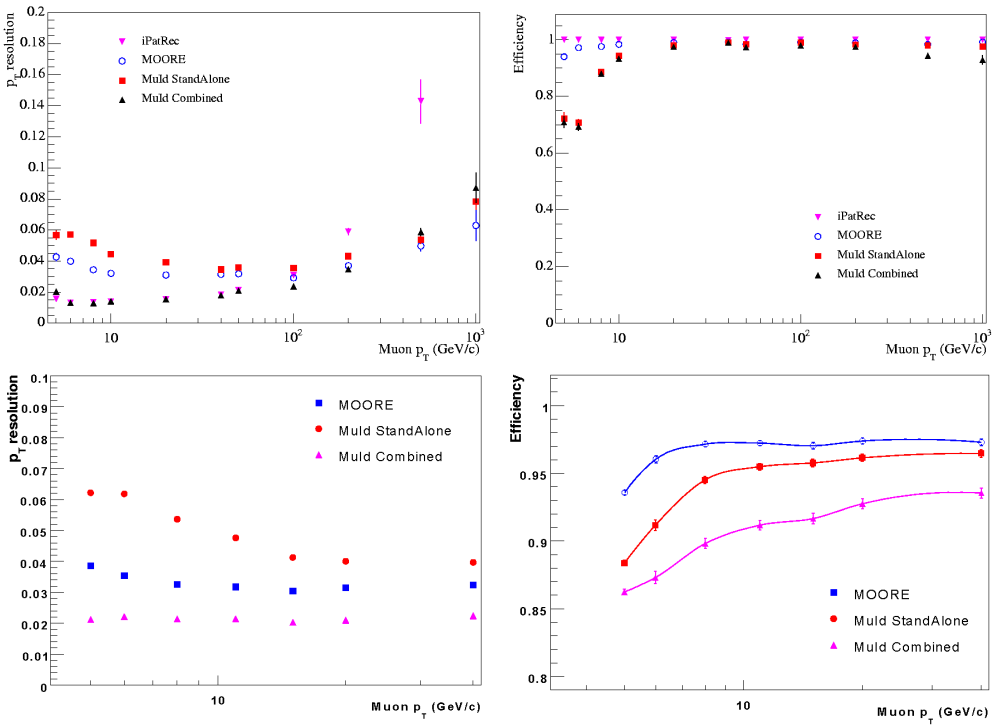

Figure 3.11. *EF resolution (left) and efficiency (right) as a function of the muon transverse momentum. Top plots were obtained using the Athena release 10.4.0 (only in the barrel region). Bottom plots, obtained with Athena release 12.0.3, are averaged over the entire η acceptance of the muon trigger ($|\eta| < 2.4$). Both releases used the EF seeded by the LVL1. MuidCB shows a loss of efficiency in release 12.0.3 that was in agreement with the offline results and was determined by tight cuts on the MS-ID track matching χ^2. These plots can be also compared with the performance results reported in Chapter 4 for the Athena release 12.0.6.*

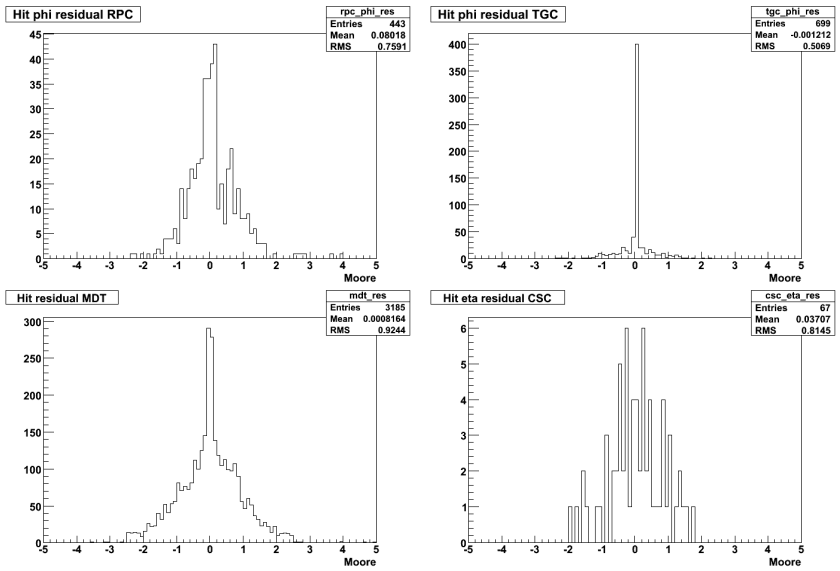

Figure 3.12. *Hit residual in presence of triggered tracks for different Muon Spectrometer detector technologies. These quantities are useful for the Monitoring and Data Quality purposes.*

In winter 2006 Athena **11.0.3** was released. Here the HLT selection was available only in the barrel region, with the Event Filter seeded by the LVL2 result. The Event Filter was completely functional, allowing the processing of the Trigger Elements up to the combined muon identification. In this release the EF FEX was run as three different instances of TrigMoore in the muon HLT sequences.

In release 12.0.3 (summer 2006) the Event Filter has been configured to run on the whole η acceptance, receiving the seeding from the LVL1. This is the first release which includes the possibility to run the FEX/HYPOS chain at the EF.

In the nightlies of release 12 the muComb algorithm has been integrated and tested over the full η acceptance, the menus for 900 GeV runs have been defined and the Event Data Model has been enhanced implementing the Athena

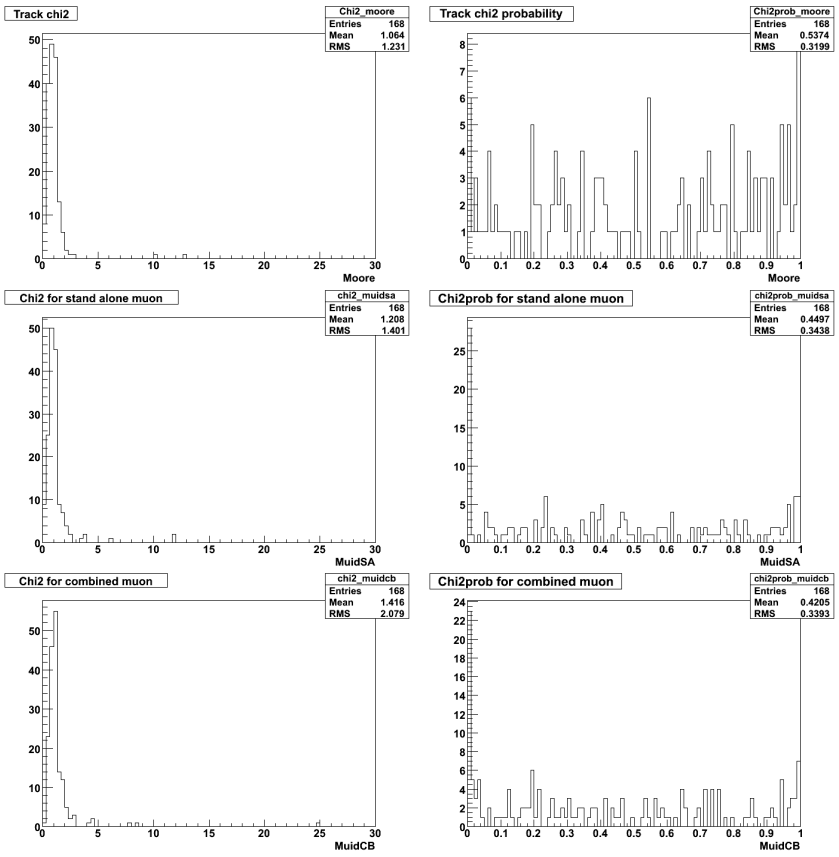

Figure 3.13. *Distribution of the track χ^2 (left) and its probability(right) for MOORE (top), MuidSA (middle) and MuidCB (bottom).*

Aware Ntuples (AANT) and a first version of Analysis Object Data (AOD) and Event Summary Data (ESD).

From release 12.0.4 the AOD have been used as input of the hypothesis algorithms in order to allow the rerunning of the p_T selection during Physics analysis, the software for the default reconstruction in the ID has changed (*iPatRec* has been replaced by *newTracking*) and misaligned data have been introduced as standard input data. More details on release 12.0.6 (summer 2007) are also available in Chap. 4. The possibility to defining monitoring variables has been also introduced in this release. A first realistic trigger

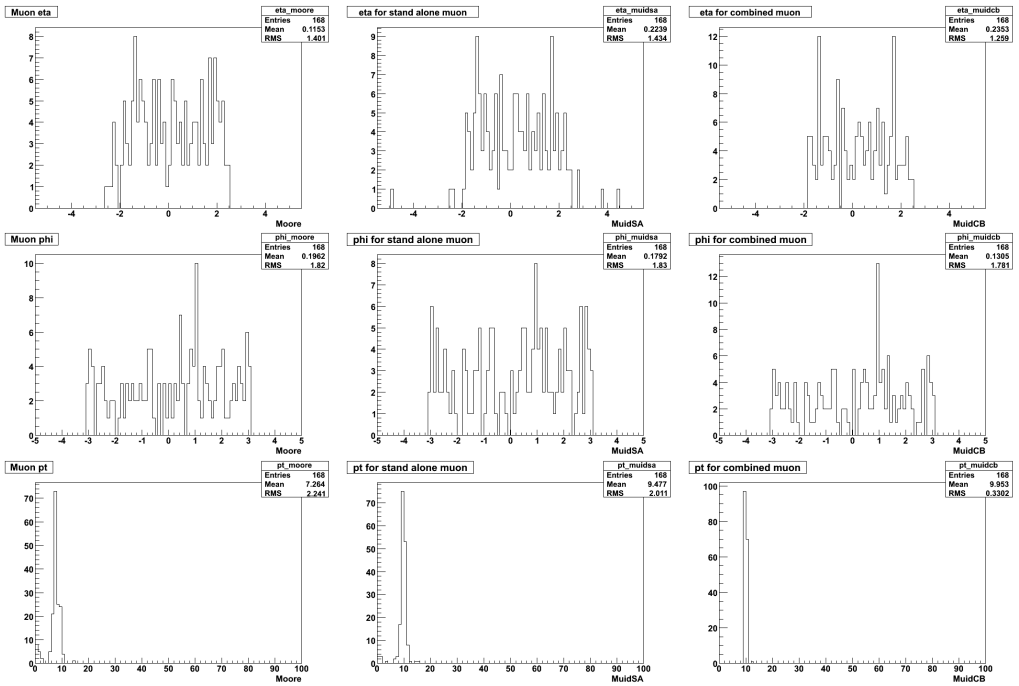

Figure 3.14. *Distribution for MOORE (left column), MuidSA (centre) and MuidCB (right) of η (top), ϕ (middle), p_T (bottom).*

menu has been implemented in release 13, as an outcome of the results that will be discussed in details in Sec.4.3.3.

Chapter 4

Muon Event Filter performance

4.1 Introduction

As seen in previous chapters, there are several reasons to require the best performance from the Muon Trigger. The entire ATLAS Physics program is highly influenced by the ability of efficiently identifying and selecting muons of high-p_T and low-p_T. Furthermore, the very harsh environment of the LHC puts very tight requirements on the rejection capability of the Trigger System. In this chapter will be analysed the performance of the muon selection operated by the High Level Trigger, with particular attention to the Event Filter.

In this section a summary of the expected muon trigger performance will be reported. The results presented have been obtained within the context of the ATLAS **Computing System Commissioning** (CSC). The CSC is the latest ATLAS data challenge before data taking and it was carefully planned in order to allow realistic MC studies of the physics potential of the ATLAS data and of detector system and performance with a very detailed simulation of the detector and a close-to-final emulation of the data preparation process

(decoding, calibrations, alignment). In particular, the Monte Carlo simulation adopted have some special features, like misalignment in the detector, full access to the calibration databases, realistic configuration of the trigger chains. To allow realistic physics analysis studies, which account for efficiencies and biases, the simulated data have been processed not only with the full suite of offline reconstruction software in order to obtain a description of each event in terms of physics analysis objects (electrons, muons, missing energy, etc.) to be readily used by physics analysis, but also with the full software emulation of the LVL1 trigger and of the HLT software, configured according to a trigger menu, in order to flag events with the trigger output. In particular, two LVL1/HLT trigger configurations have been setup, denoted as "CSC-06" and "CSC-06-900GeV". They define the values of the 6 programmable thresholds of LVL1 and the p_T thresholds applied with hypothesis algorithms of the HLT for a trigger menu that includes realistic muon signatures. CSC-06-900GeV has relaxed thresholds settings (Fig. 3.3.1) and FEX algorithms configuration (e.g. the RoI dimension) which are optimised for first LHC collisions, when energy and luminosity will be very low and the event rate will not be the main problem.

Depending on the physics community needs, the CSC samples have been processed with one of the shown trigger configurations. Typically, B-physics studies have requested some relaxed trigger configuration intended to explore the physics potential of early data at low luminosity, while physics involving heavy objects usually require the thresholds mu20 and mu40.

For the Computing System Commissioning the complete analysis model has been tested, using, in particular, the GRID [78] computing facility to simulate and reconstruct the CSC data, thus demonstrating the functionality of the overall computing model.

One item of the performance studies planned in the context of the ATLAS CSC was the Muon Slice. The aim of this item was to update coherently the efficiency and rate evaluations for all muon trigger levels with common high statistics MC productions and software suite. This Chapter will summarise the methods and the outcomes of these studies as far as EF performance is concerned. In particular, Sec. 4.1.2 will describe the special CSC MC samples produced for the seek of muon trigger studies and the special configuration of reconstruction job used for processing them.

4.1.1 Muon rates

The rate of particles in the muon spectrometer is the starting point for any attempt to design an inclusive muon trigger menu. The flux of muons originates from several sources: semileptonic decays of heavy particles (b, c, t, W, Z), Drell-Yan and J/ψ production, hadron decays (π, K), and punch-through particles from hadrons.

Since the transverse momentum spectrum is steeply falling at increasing p_T, particular care must be devoted to inclusive low p_T muon triggers that are expected to be run at low luminosity. More details on the methods used to estimate the muon cross sections presented here can be found in [79]. This work reported a breakdown of the total inclusive muon rate into the contributions of all the most relevant production channels in an wide interval of transverse momentum: from 3 to 50 GeV. The predictions for most of the physics production channels (heavy quarks and W/Z/top decays) were obtained with PYTHIA 5.7 with the parton distribution functions CTEQ2L and Peterson fragmentation function for heavy quarks. For the muon rate from light meson decays, the results of a simulation based on PDMJET-II was used. A study of muons from pion and kaon decays appeared short af-

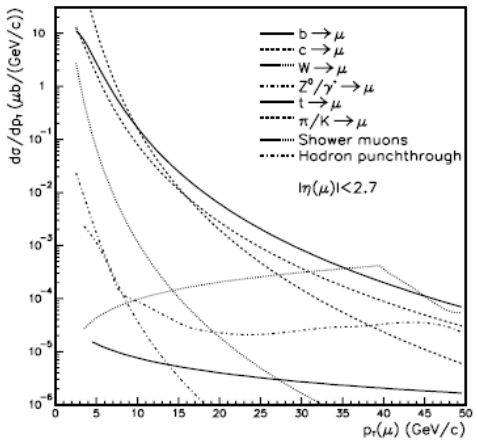

Figure 4.1. *Differential cross-section $d\sigma/dp_T$ for inclusive muon production at the LHC. The pseudo-rapidity range is $|\eta| < 2.7$.*

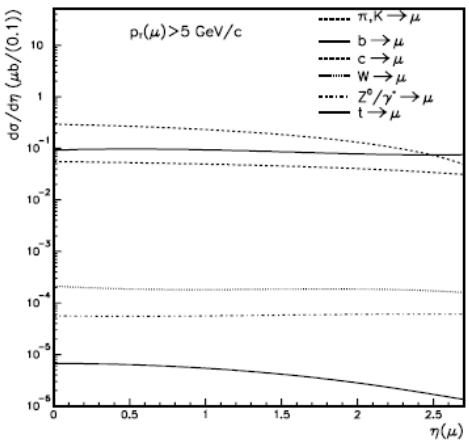

Figure 4.2. *Differential cross-section $d\sigma/d\eta$ for inclusive muon production at the LHC. The transverse momentum for the muons is greater than 5 GeV.*

ter where results from PYTHIA 5.7 and DPMJET-II were compared as a function of η and p_T of the secondary muon; these Monte Carlo predictions were used to produce parametrisation of the double differential cross section, $d^2N_\mu/dp_T d\eta$, predicted by the two generators which have been assumed in more recent muon trigger rates estimations, starting from [42] and in most of the subsequent studies, with a preference for the higher DPMJET cross section, leading to more conservative trigger rate estimations.

Fig. 4.1 shows the inclusive muon p_T spectrum. Hadron punch-through and shower leakage were estimated to be negligible for p_T above 3 GeV. The rate is dominated by π/K decays up to $p_T = 10$ GeV, and by b and c decays from 10 GeV to 30 GeV. At the LHC energies the majority of b-quark and c-quark production originates from higher-order processes: gluon splitting and flavor excitation. At large values of p_T, W and Z decays give sizeable contributions. Muon production from direct J/ψ is not included in Fig. 4.1;

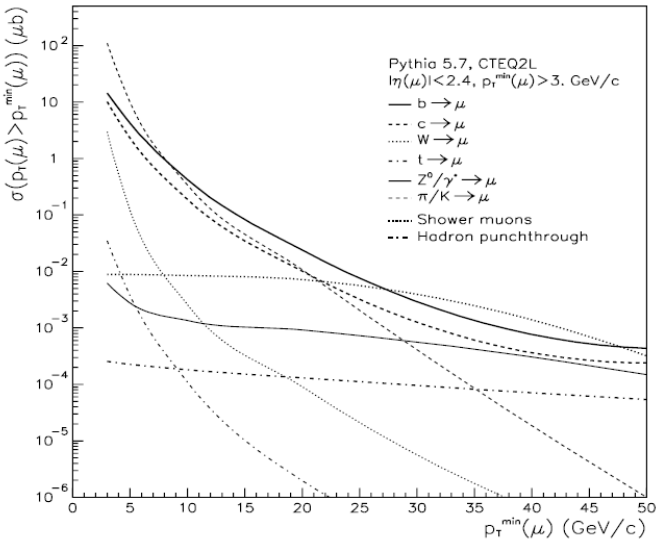

Figure 4.3. *Integrated cross-section for inclusive muon production at the LHC as a function of the p_T threshold. The pseudo-rapidity range of the muons is* $|\eta| < 2.4$.

the contribution is roughly two orders of magnitude less than that from b and c decays.

In Fig. 4.2 the pseudorapidity distribution is shown for muons with $p_T >$ 5 GeV. The distributions are flat in pseudorapidity with the exception of muons from top decay (heavy-mass particles are produced centrally), and muons from π/K decay. At fixed p_T, the probability for π/K decay in the volume up to the calorimeters is constant over the barrel region, where the path-length increases with increasing η is compensated by the increase in $\gamma c\tau$; however, in the endcap region, the ratio of path-length to $\gamma c\tau$ decreases with increasing η). Fig.4.3 shows the integrated cross-section. The trigger rate can be adjusted, without loss of efficiency for heavier objects, by moving the threshold over a wide range of low-p_T values.

Di-muon rates have been estimated in ATLAS through simulations of π/K,

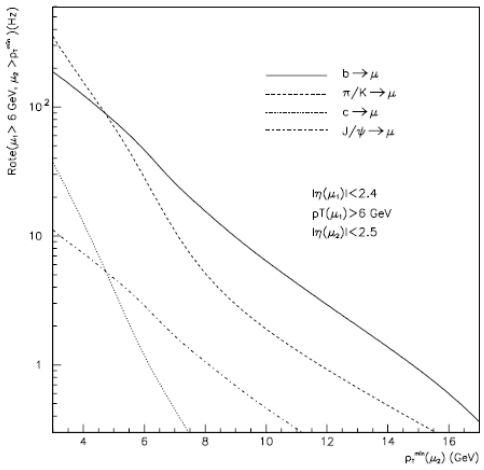

Figure 4.4. *Di-muon rates in ATLAS for* $10^{33} cm^{-2} s^{-1}$. *Dashed line: Contributions from* π/K *decays where* μ_1 *originates from* π/K, *b or c decays and* μ_2 *originates from a* π/K *decay. Solid line:* $b\bar{b}$ *decays, including cascade decays. Dotted line:* $c\bar{c}$ *decays. Dash-dotted line:* J/ψ *decays.*

$b\bar{b}$ and $c\bar{c}$ spectra. For direct J/ψ production a colour octet model was used, which is implemented in PYTHIA. π/K spectra were calculated from minimum bias events assuming a decay volume of length ± 340 cm along z and of radius 150 cm, which corresponds to the radius of the inner detector plus one additional interaction length. Estimated integrated rates are shown in Fig. 4.4 . For the first muon (μ_1) in the event, the rates have been integrated over $p_T > 6$ GeV. For the second muon (μ_2), the rates have been integrated over $p_T > p_T^{min}$, and are shown as a function of this threshold.

4.1.2 Samples and configuration

In the studies presented here the final trigger chain, as shown in Fig 3.1, has been configured to operate the muon selection over the full η acceptance of the detector, using the seeding strategy as in the real LHC running conditions.

The full trigger chain follows the schema reported in Fig. 3.1. The last three steps of the chain correspond to the EF algorithms, which have been extensively described in Sec. 3.3:

- the reconstruction in the Muon Spectrometer by MOORE, which computes all track parameters at the MS entrance;
- the extrapolation of the track reconstructed in the Muon Spectrometer to the interaction point by MuId standalone, which uses the calorimetric information (obtained from a parametrisation of the energy loss or from a direct measurement);
- the combination of the tracks found in the Muon Spectrometer and in the Inner Detector by MuId combined.

After each step, a TrigMoore hypothesis algorithm (see Sec. 3.3.1) might have been enabled to perform the trigger decision on the basis of kinematical and topological requirements.
In the special data processing tasks configured for muon trigger studies the HLT hypothesis have been, in fact, disabled. As a consequence a Trigger Element is validated at each step of the trigger sequence, provided a muon object is found, regardless of the measured p_T. This configuration allows to study the output of each trigger level without the bias of any hypothesis or to apply (and use) hypothesis cuts at the analysis stage.
Most of the results reported here have been obtained applying a p_T cut to the final trigger element processed at each level: at the EF, for example, only the standalone and combined muon tracks scrutinised with respect to a specific p_T hypothesis. More sofisticated selections can be applied for dedicated rejection, an example of these is described in Sec. 4.3.1. The results of such studies will be discussed in full detail in the following sub-sections. The

results presented in this Chapter were produced from data simulated using a full GEANT4 [80] based simulation of the ATLAS detector.
All the samples have been simulated with the ATLAS software, ATHENA, using release 12.0.3, and a special detector description version, indicated as ATLAS-CSC-01-02-00. This simulation takes into account several realistic effects, as muon chamber misalignment, obtained by tilting and shifting randomly the chambers according to a gaussian distribution with sigma of 1 mrad and 1 mm respectively. This allows to test the sensitivity of the muon identification algorithms to incomplete knowledge of the detector geometry. LVL1 Simulation and HLT reconstruction have been run within ATHENA release 12.0.6, using, mainly, for most of the performance studies the same geometry database used by simulation. A few analyses, involving rather new developments, have been done reprocessing simulated data within ATHENA release 13.0.X, where the X indicates different releases that have been used. A large sample of single prompt muons (few millions events) simulated uniformly in $\eta - \phi$ projections, with fixed p_T ranging from 2 GeV to 1 TeV, have been used to understand in great detail the performance of the muon trigger. A detailed list of the used datasets is shown in 4.5. The motivation of such large sample is two-fold: the need to have a reasonable estimate of the very low efficiency for the selection of low pt muons (10^{-4} for transverse momentum around 2 GeV at the nominal threshold of 4 GeV) and the necessity to refine the LVL2 Look Up Tables for some key p_T threshold (6, 20 and 40 GeV).
One of the main background for the Muon Trigger selection comes from in-flight decays of charged kaons and pions. This has been estimated using samples of minimum bias and single pions, with the mesons forced to decay inside the Inner Detector in order to facilitate the production of a sizable

sample of π/K in-flight decays. The list of the used datasets is shown in Fig. 4.6.

p_T (GeV)	Dataset	Events
2	caldigoff1_mc12.007200.singlepart_mu2.digit.RDO.v12003107	10^6
2.5	caldigoff1_mc12.007201.singlepart_mu2p5.digit.RDO.v12003107	10^6
3	caldigoff1_mc12.007202.singlepart_mu3.digit.RDO.v12003107	10^6
3.5	caldigoff1_mc12.007203.singlepart_mu3p5.digit.RDO.v12003107	10^6
4	caldigoff1_mc12.007204.singlepart_mu4.digit.RDO.v12003107	$5{\cdot}10^5$
4.5	caldigoff1_mc12.007205.singlepart_mu4p5.digit.RDO.v12003107	$5{\cdot}10^5$
5	misal1_mc12.007206.singlepart_mu5.digit.RDO.v12003107	$5{\cdot}10^5$
6	caldigoff1_mc12.007207.singlepart_mu6.digit.RDO.v12003107	$2{\cdot}10^6$
7	caldigoff1_mc12.007208.singlepart_mu7.digit.RDO.v12003107	$2{\cdot}10^5$
8	caldigoff1_mc12.007209.singlepart_mu8.digit.RDO.v12003107	$2{\cdot}10^5$
9	caldigoff1_mc12.007210.singlepart_mu9.digit.RDO.v12003107	$2{\cdot}10^5$
10	caldigoff1_mc12.007211.singlepart_mu10.digit.RDO.v12003107	$2{\cdot}10^5$
11	misal1_mc12.007212.singlepart_mu11.digit.RDO.v12003107	$2{\cdot}10^5$
13	caldigoff1_mc12.007261.singlepart_mu13.digit.RDO.v12003107	$2{\cdot}10^5$
14	caldigoff1_mc12.007262.singlepart_mu14.digit.RDO.v12003107	$2{\cdot}10^5$
15	caldigoff1_mc12.007213.singlepart_mu15.digit.RDO.v12003107	$2{\cdot}10^5$
16	caldigoff1_mc12.007214.singlepart_mu16.digit.RDO.v12003107	$2{\cdot}10^5$
17	caldigoff1_mc12.007215.singlepart_mu17.digit.RDO.v12003107	$2{\cdot}10^5$
18	caldigoff1_mc12.007216.singlepart_mu18.digit.RDO.v12003107	$2{\cdot}10^5$
19	caldigoff1_mc12.007217.singlepart_mu19.digit.RDO.v12003107	$2{\cdot}10^5$
19	misal1_mc12.007217.singlepart_mu19.digit.RDO.v12003107	$2{\cdot}10^5$
20	caldigoff1_mc12.007218.singlepart_mu20.digit.RDO.v12003107	$2{\cdot}10^6$
21	caldigoff1_mc12.007219.singlepart_mu21.digit.RDO.v12003107	$2{\cdot}10^5$
22	caldigoff1_mc12.007220.singlepart_mu22.digit.RDO.v12003107	$2{\cdot}10^5$
24	caldigoff1_mc12.007221.singlepart_mu24.digit.RDO.v12003107	$2{\cdot}10^5$
26	caldigoff1_mc12.007222.singlepart_mu26.digit.RDO.v12003107	$2{\cdot}10^5$
28	caldigoff1_mc12.007223.singlepart_mu28.digit.RDO.v12003107	$2{\cdot}10^5$
30	caldigoff1_mc12.007224.singlepart_mu30.digit.RDO.v12003107	$2{\cdot}10^5$
32	caldigoff1_mc12.007225.singlepart_mu32.digit.RDO.v12003107	$2{\cdot}10^5$
34	caldigoff1_mc12.007226.singlepart_mu34.digit.RDO.v12003107	$2{\cdot}10^5$
36	caldigoff1_mc12.007227.singlepart_mu36.digit.RDO.v12003107	$2{\cdot}10^5$
38	misal1_mc12.007228.singlepart_mu38.digit.RDO.v12003107	$2{\cdot}10^5$
40	caldigoff1_mc12.007229.singlepart_mu40.digit.RDO.v12003107	$2{\cdot}10^6$
45	caldigoff1_mc12.007230.singlepart_mu45.digit.RDO.v12003107	$2{\cdot}10^5$
50	caldigoff1_mc12.007231.singlepart_mu50.digit.RDO.v12003107	$2{\cdot}10^5$
75	caldigoff1_mc12.007232.singlepart_mu75.digit.RDO.v12003107	$2{\cdot}10^5$
100	misal1_mc12.007233.singlepart_mu100.digit.RDO.v12003107	$2{\cdot}10^5$
200	caldigoff1_mc12.007234.singlepart_mu200.digit.RDO.v12003107	$2{\cdot}10^5$
500	misal1_mc12.007235.singlepart_mu500.digit.RDO.v12003107	$2{\cdot}10^5$
1000	caldigoff1_mc12.007236.singlepart_mu1000.digit.RDO.v12003107	$2{\cdot}10^5$

Figure 4.5. *Monte Carlo single muons and number of events used in the analyses.*

Single $\pi \rightarrow \mu\nu$ datasets	
Dataset	Events
misal1_mc12.007160.singlePion_pTSlice_0_of_30.digit.v12000502	$100 \cdot 10^3$
misal1_mc12.007161.singlePion_pTSlice_1_of_30.digit.v12000502	$100 \cdot 10^3$
misal1_mc12.007162.singlePion_pTSlice_2_of_30.digit.v12000502	$80 \cdot 10^3$
misal1_mc12.007163.singlePion_pTSlice_3_of_30.digit.v12000502	$70 \cdot 10^3$
misal1_mc12.007164.singlePion_pTSlice_4_of_30.digit.v12000502	$60 \cdot 10^3$
misal1_mc12.007165.singlePion_pTSlice_5_of_30.digit.v12000502	$55 \cdot 10^3$
misal1_mc12.007166.singlePion_pTSlice_6_of_30.digit.v12000502	$50 \cdot 10^3$
misal1_mc12.007167.singlePion_pTSlice_7_of_30.digit.v12000502	$45 \cdot 10^3$
misal1_mc12.007168.singlePion_pTSlice_8_of_30.digit.v12000502	$40 \cdot 10^3$
misal1_mc12.007169.singlePion_pTSlice_9_of_30.digit.v12000502	$35 \cdot 10^3$
misal1_mc12.007170.singlePion_pTSlice_10_of_30.digit.v12000502	$30 \cdot 10^3$
misal1_mc12.007171.singlePion_pTSlice_11_of_30.digit.v12000502	$30 \cdot 10^3$
misal1_mc12.007172.singlePion_pTSlice_12_of_30.digit.v12000502	$25 \cdot 10^3$
misal1_mc12.007173.singlePion_pTSlice_13_of_30.digit.v12000502	$25 \cdot 10^3$
misal1_mc12.007174.singlePion_pTSlice_14_of_30.digit.v12000502	$20 \cdot 10^3$
misal1_mc12.007175.singlePion_pTSlice_15_of_30.digit.v12000502	$35 \cdot 10^3$
misal1_mc12.007176.singlePion_pTSlice_16_of_30.digit.v12000502	$30 \cdot 10^3$
misal1_mc12.007177.singlePion_pTSlice_17_of_30.digit.v12000502	$25 \cdot 10^3$
misal1_mc12.007178.singlePion_pTSlice_18_of_30.digit.v12000502	$25 \cdot 10^3$
misal1_mc12.007179.singlePion_pTSlice_19_of_30.digit.v12000502	$25 \cdot 10^3$
misal1_mc12.007180.singlePion_pTSlice_20_of_30.digit.v12000502	$25 \cdot 10^3$
misal1_mc12.007181.singlePion_pTSlice_21_of_30.digit.v12000502	$25 \cdot 10^3$
misal1_mc12.007182.singlePion_pTSlice_22_of_30.digit.v12000502	$25 \cdot 10^3$
misal1_mc12.007183.singlePion_pTSlice_23_of_30.digit.v12000502	$25 \cdot 10^3$
misal1_mc12.007184.singlePion_pTSlice_24_of_30.digit.v12000502	$20 \cdot 10^3$
misal1_mc12.007185.singlePion_pTSlice_25_of_30.digit.v12000502	$15 \cdot 10^3$
misal1_mc12.007186.singlePion_pTSlice_26_of_30.digit.v12000502	$5 \cdot 10^3$
misal1_mc12.007187.singlePion_pTSlice_27_of_30.digit.v12000502	$5 \cdot 10^3$
misal1_mc12.007188.singlePion_pTSlice_28_of_30.digit.v12000502	$5 \cdot 10^3$
misal1_mc12.007189.singlePion_pTSlice_29_of_30.digit.v12000502	$5 \cdot 10^3$
misal1_mc12.007190.singlePion_pTSlice_30_of_30.digit.v12000502	$5 \cdot 10^3$

Figure 4.6. *Monte Carlo single pions and number of events used in the analyses.*

4.2 Performance

4.2.1 Resolution

The transverse momentum resolution of the algorithms is very important because it determines the sharpness in p_T of the transition between rejection and selection of muon trigger candidates, once a given p_T threshold is requested by a trigger menu. As a matter of fact, an important figure of merit of a trigger algorithm is the efficiency curve vs p_T for the threshold of physical interest.

More generally, a first evaluation of the quality of the EF feature extraction algorithms must come from the comparison of the muon tracking performance with respect to the ATLAS offline software.

The resolutions have been evaluated as the sigma of a gaussian fit to the distribution of v^{rec}/v^{gen}, where v^{rec} and v^{gen} are the reconstructed and true values of the given quantity v. The high statistic single muon samples of fixed p_T have been used to quote p_T resolution averaged over the geometrical acceptance of the trigger. For a fixed p_T single muon sample the p_T resolution is also studied as a gaussian of the pseudorapidity by performing the analysis of the v^{rec}/v^{gen} distribution separately in various small bins of the muon pseudorapidity.

The distributions of measured p_T over true p_T for 6 GeV and 40 GeV muons, reconstructed in the EF with MuId combined, are shown in Fig. 4.7 for the barrel and endcap regions. The distributions are correctly centred around 1 and show very limited non gaussian tails. This ensures that the reconstruction procedure is not introducing biases in the p_T scale and the fluctuations can be described by a single gaussian approximation. In Fig. 4.8, the p_T resolution (averaged over the full η range) is shown as a function of p_T for

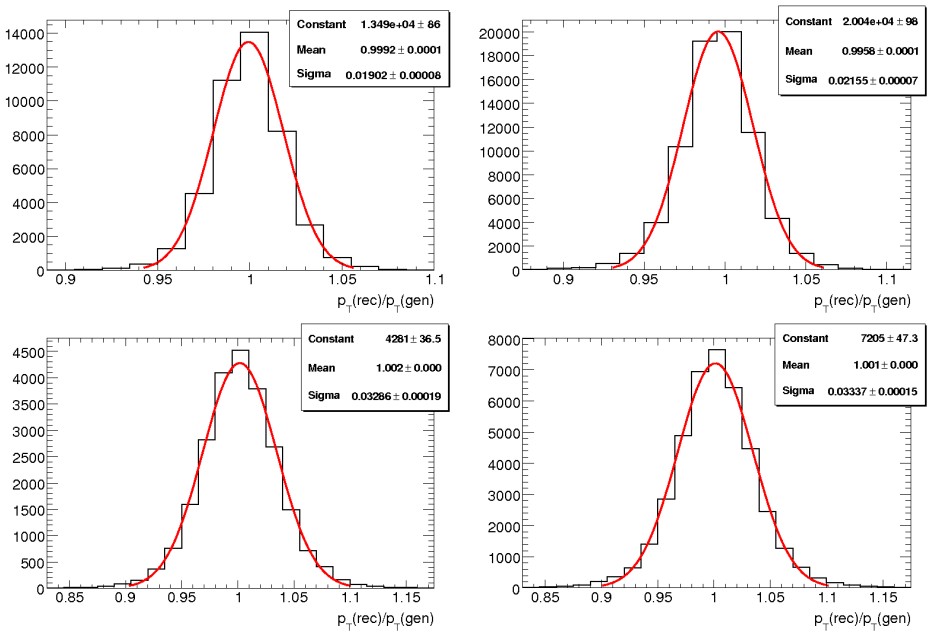

Figure 4.7. *MuId combined* $1/p_T$ *resolution for 6 GeV (left) and 40 GeV (right) muons in the barrel (up) and in the endcap (down) regions.*

all EF algorithms: the reconstruction of a muon with p_T below 50 GeV takes great advantage in combining the Muon Spectrometer measurement with the one from the Inner Detector, which is much more precise, while for p_T above 100 GeV, the Muon System dominates the measurement of the muon combined transverse momentum. Fig. 4.9 shows the results obtained separately for the different detector regions, where different detector technologies and magnetic field configurations are present. Results on ϕ and η resolutions are reported in Fig. 4.10 as obtained with MOORE, MuId standalone and MuId combined as a function of the muon transverse momentum. As expected, these resolutions deteriorate at low-p_T , owing to the multiple scattering effect. Remarkable improvements by MuId combined are evident with respect to the standalone muon reconstruction (up to two orders of magnitude). Transverse momentum resolution versus η is shown in Fig. 4.11 and 4.12 for

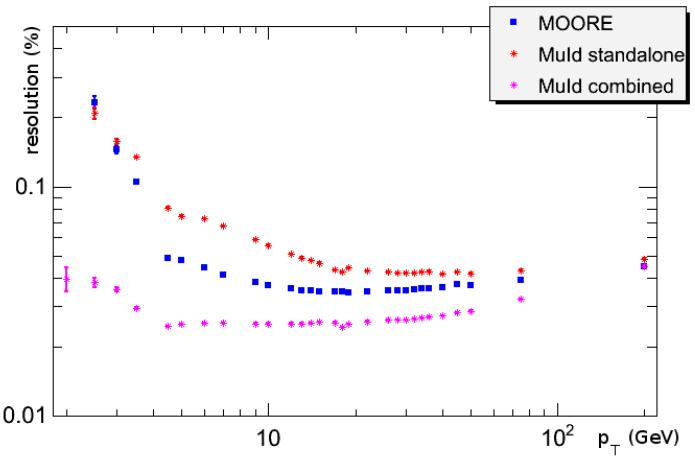

Figure 4.8. *Relative transverse momentum resolution as a function of p_T for MOORE, MuId standalone and MuId combined, averaged over η and ϕ.*

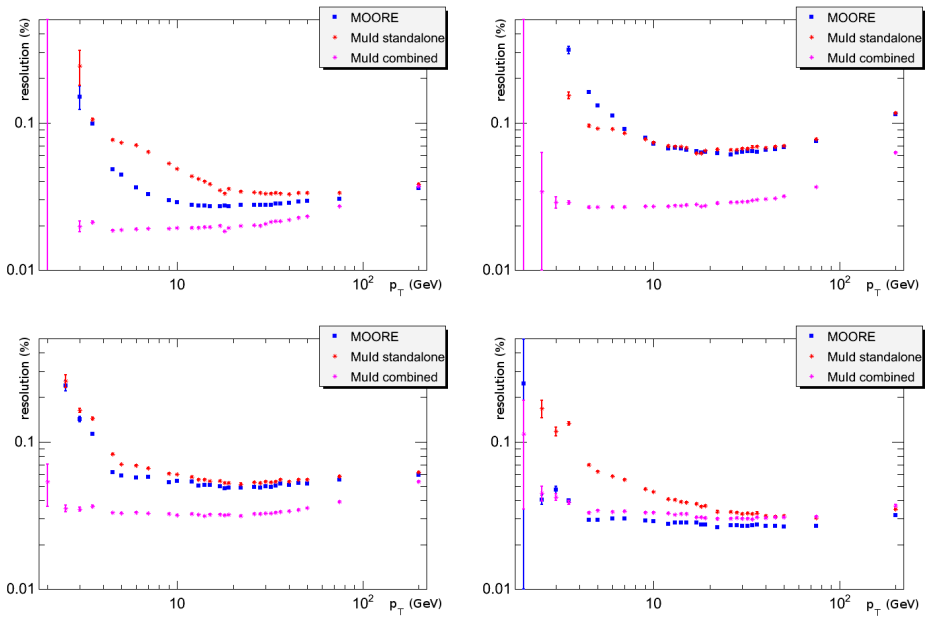

Figure 4.9. *Relative transverse momentum resolution as a function of p_T for MOORE, MuId Standalone and MuId Combined, averaged over ϕ and differentiated for various pseudorapidity regions: BAR (top-left), EC1 (top-right), EC2 (bottom-left) and EC3 (bottom-right).*

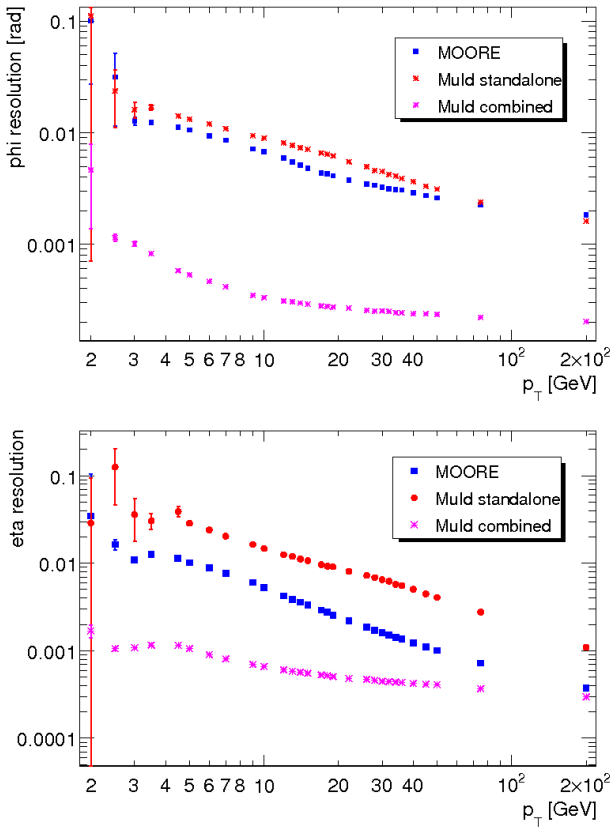

Figure 4.10. *Resolution (in rad) on azimuthal angle ϕ (top) and pseudorapidity η (bottom) as a function of muon p_T in the cases of MOORE, MuId standalone and MuId combined. All values are averaged over the full η range.*

single muons of p_T equal to $6, 8, 10$ GeV and $11, 20, 40$ GeV, respectively. The worsening of the resolution in the region $1.0 < |\eta| < 1.5$ is to be attributed to the highly inhomogeneous magnetic field in the barrel-endcap transition region of the toroidal field of the Muon Spectrometer. This effect is recovered by means of the combined reconstruction which exploits the Inner Detector performance driven by the uniform and solenoidal field.

As an obvious outcome of the fact that the muon EF algorithms are the same used in the offline reconstruction, performance results shown so far in

all the acceptance regions are in good agreement with those found in the offline tracking environment.
The presence of biases in the trigger selection has been considered studying the ratio p_T^{rec}/p_T^{gen} (Fig. 4.11 and 4.12). The ratio p_T^{rec}/p_T^{gen} is compatible with 1, demonstrating the absence of biases. In the figures are also reported the relative p_T resolution for single muons in a wide range of transverse momentum, in particular, for muons of fixed p_T equal to the value of the p_T thresholds for low-luminosity and high-luminosity menus.

To study the systematics introduced by detector geometrical distortions, were compared the results obtained using two different detector geometry configurations, ATLAS-CSC-01-00-00 and ATLAS-CSC-01-02-00. For simplicity we will indicate the first one as "ideal" geometry and the second one as "misaligned". Data simulated with the ideal geometry were reconstructed coherently with the detector description, while data simulated with the misaligned geometry were reconstructed using both the ideal and misaligned detector descriptions. The results for single muons of fixed transverse momentum (p_T = 20 GeV), reported in Fig. 4.13, do not show significant systematic effects.

4.2.2 Efficiency

The trigger efficiency is a key topic for the proper functionality of the experiment. The high event rate determined by uninteresting SM processes and by fake muon tracks can have a strong impact on the Muon Trigger System and risk to saturate the output bandwidth in case of not properly tuned selections. On the other side, the ability to select efficiently all the events that can have significance for discovery of new physics requires a careful balance of efficiency maximisation and affordability of the trigger output rate. A han-

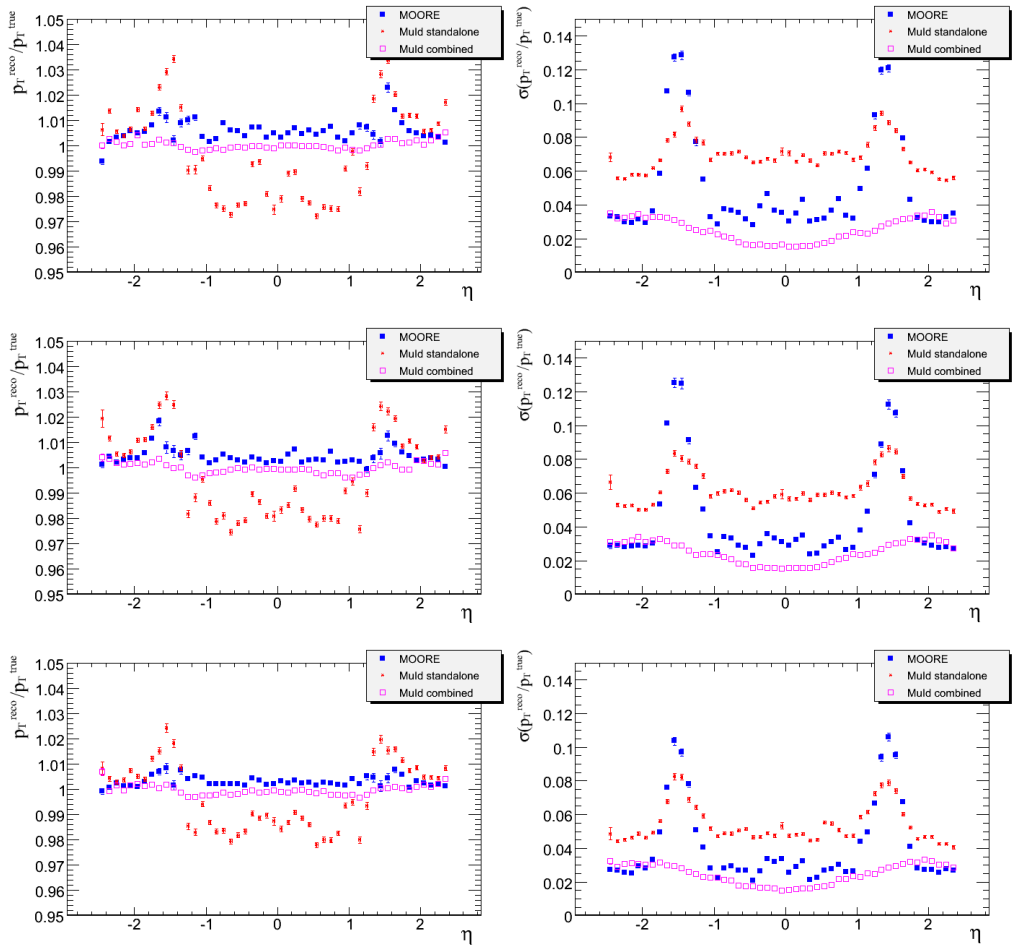

Figure 4.11. *Ratio p_T^{rec}/p_T^{gen} (left) and resolution on p_T (right) as a function of the generated muon pseudorapidity in the cases of MOORE, MuidSA and MuidCB for single muons with $p_T = 6$ GeV (upper plots), 8 GeV (central plots), 10 GeV (lower plots).*

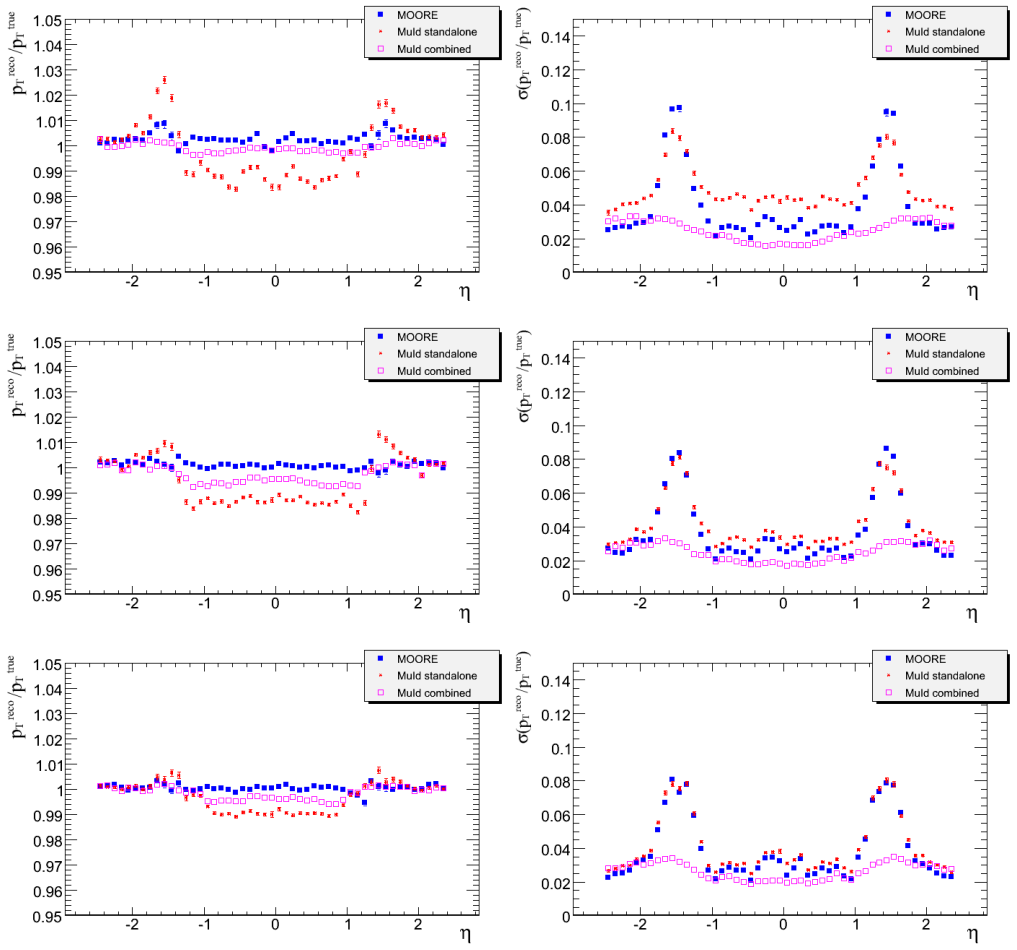

Figure 4.12. *Ratio p_T^{rec}/p_T^{gen} (left) and resolution on p_T (right) as a function of the generated muon pseudorapidity in the cases of MOORE, MuidSA and MuidCB for single muons with $p_T = 11$ GeV (upper plots), 20 GeV (central plots), 40 GeV (lower plots).*

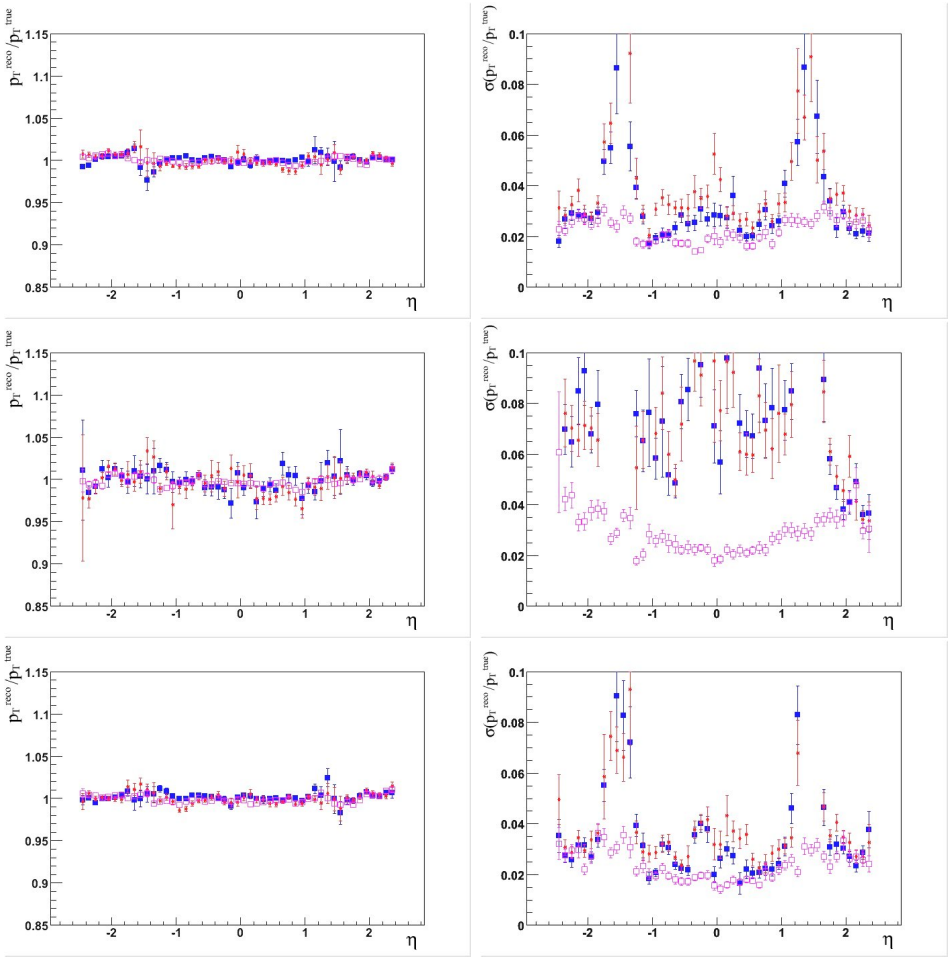

Figure 4.13. *Reconstructed p_T over generated p_T (mean value on the left, standard deviation on the right) for single muon samples of $p_T = 20$ GeV. Values obtained using: the nominal detector geometry (ATLAS-CSC-01-00-00) for both simulation and reconstruction (top); the misaligned detector geometry (ATLAS-CSC-01-02-00) for the simulation and the nominal geometry for the reconstruction (middle); the misaligned detector geometry for both simulation and reconstruction.*

dle eventually available to fulfil these opposite requirements is the prescale mechanism, which allows to accept for store only a certain fraction of the validated trigger elements. It can be selectively applied to some items in the trigger menu in order to reduce in a well controlled and unbiased manner the rate of events accepted by such triggers.

The efficiency studies are performed using simulated single muon Monte Carlo samples. Furthermore simulated data samples containing expected processes, which can be interesting for physics, have been analysed to cross-check the results with respect to the single muon selection, and to understand eventual problems not identified with other techniques.

Efficiency in single muon events is defined as the ratio of events with a reconstructed track at the EF level after the execution of each algorithm to all events which have passed selection by both LVL1 and LVL2, including the LVL2 hypothesis algorithm. The EF efficiency with respect to LVL2, as a function of p_T, is shown in Fig. 4.14 for all three EF algorithms (without executing the EF hypothesis algorithms). The efficiencies drop in the range p_T between 3 and 6 GeV due to multiple scattering and energy loss fluctuation effects. Moreover, in the case of MuId combined, at very high momentum region the increasing probability of muon showering is responsible of a small loss in efficiency. In fact the drastical energy loss decreases the probability of successful combination between MS and ID tracks.

As shown in Fig. 4.15 and 4.16 for 6 GeV and 40 GeV muons, the efficiencies versus η and ϕ (with respect to LVL2 and without executing the EF hypothesis algorithms) show a structure, more evident at low momentum, explainable with a residual dependence on the muon spectrometer geometrical acceptance both in η and ϕ. In particular is evidenced the loss of efficiency in the region $1.0 < |\eta| < 1.2$ due to the inhomogeneities of the toroidal field

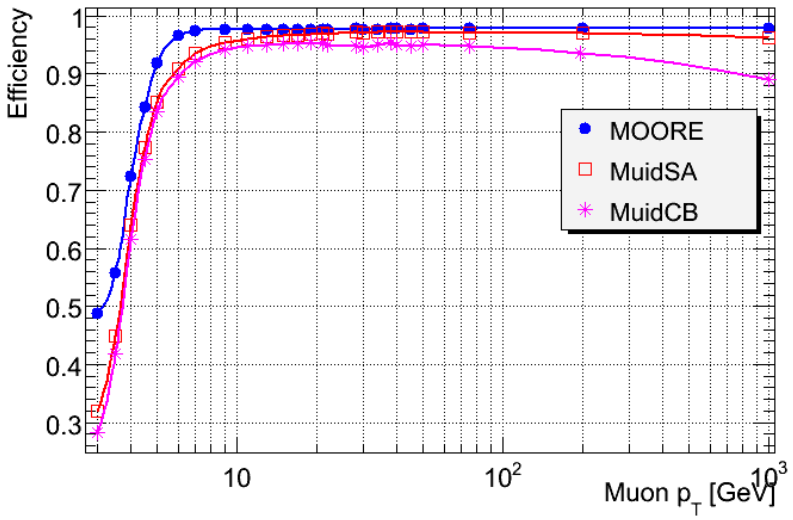

Figure 4.14. *Reconstruction efficiency of MOORE, MuidSA and MuidCB algorithms run in the EF without applying any requirement on the p_T.*

(overlap of the barrel and endcap magnetic fields). The efficiency is defined here on an event basis, and counts only once events having LVL2 muon-feature or EF track multiplicity greater than 1. The LVL1 p_T thresholds, defined by the Coincidence Window opening, are such that the efficiency at a given p_T threshold (e.g. 6 GeV or 40 GeV) is 90% for single muons with p_T equal to the nominal threshold value. In practice, at LVL1 the final efficiency can be a bit higher because of the rough granularity of the trigger chambers. The HLT values of p_T thresholds (p_T^{thr}) are normalised to the ones of LVL1 and defined as follows, starting from Monte Carlo samples of single muons with p_T equal to the thresholds under study. For a given threshold of interest, a histogram is filled with the value of the reconstructed p_T (one for each algorithm of the HLT chain). Given these distributions, the integral is computed summing over the bins from 0 to a certain value such that the integral equals 10% of the total number of accepted muons without any p_T

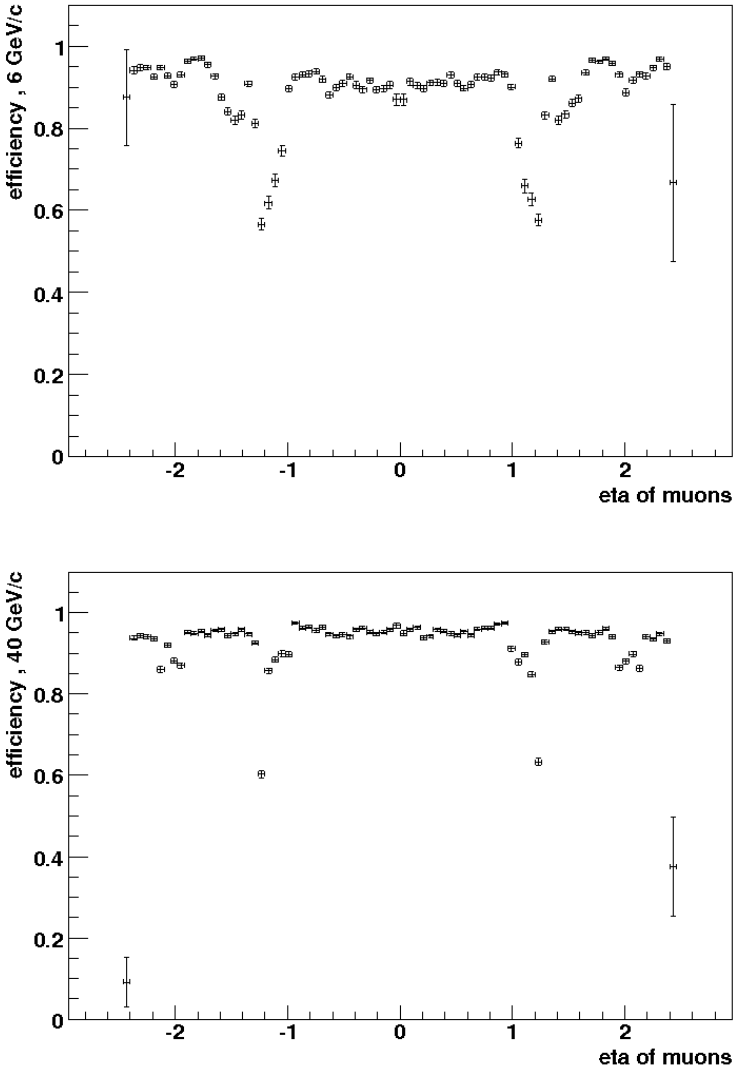

Figure 4.15. *Efficiency vs. η of MuId combined for 6 GeV (top) and 40 GeV (bottom) muons.*

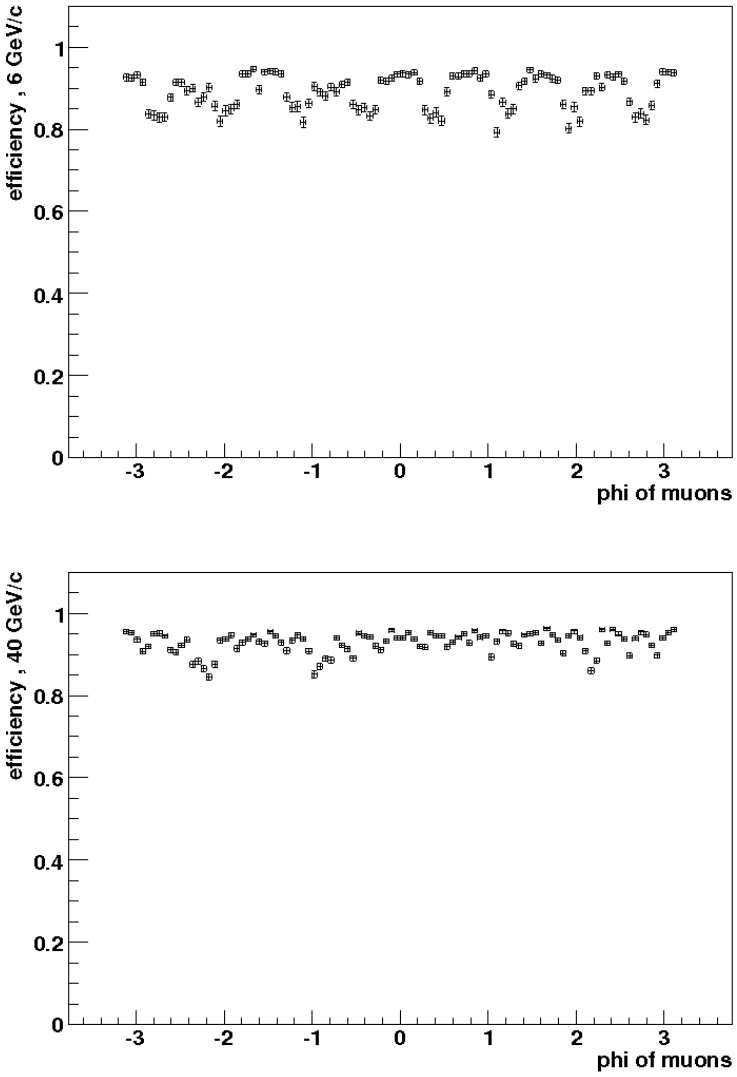

Figure 4.16. *Efficiency vs. ϕ of MuId combined for 6 GeV (top) and 40 GeV (bottom) muons.*

cut applied. In order to get the best possible estimate of the threshold value p_T^{thr}, a linear interpolation is performed between the i-th bin (i.e. the first one at which the 10% of the integral is exceeded) and the previous one (i-1). In practice this value is obtained as

$$p_T^{thr} = p_T^{i-1} + \frac{10\% - \sum_{j=1}^{i-1} N_j}{N_i} \cdot \Delta p_T \tag{4.1}$$

where N_i is the content of the i-th bin normalised to 1 and Δp_T is the bin width. Actually this is only a first order approximation and a polynomial function would better be used for a more precise estimate of p_T^{thr}, since usually the p_T distribution increase quite rapidly just near the nominal threshold value. This procedure is applied for the algorithms muFast, muComb, MuidSA and MuidCB, normalising the total number of accepted muons to the one at the previous level.

The error on p_T^{thr} is mainly related to the size of the bins of the histogram, thus is directly related to the abundance of the sample used for the study. Using samples going from few hundred thousand to few million events, the error on the threshold is of the order of $10 \div 100$ MeV. The effective HLT thresholds, as calculated in ATHENA release 12.0.6 using the "CSC-06" and "CSC-06-900GeV" data samples, are reported in Fig. 4.17. The threshold indicated as "mu4" has not been estimated using this approach, and the values used for it are arbitrarily chosen to avoid the trigger rate to explode.

The ATLAS software allows the implementation of different thresholds for different η and ϕ intervals. In Fig. 4.17 are reported the values for the different detector regions in pseudo-rapidity; for the EF algorithms has been also estimated the effective threshold averaged over the full η acceptance.

The relative trigger efficiencies for the LVL1 software emulation (with respect to MC truth), for muComb (with respect to LVL1) and MuidCB (with respect to muComb) algorithms, after applying the relative hypothesis algo-

Algo / THR	mu 4	mu 5	mu 6	mu 8	mu 10	mu 11	mu 15	mu 20	mu 40
muFast									
bar	3.0	4.6	5.4	7.2	8.9	9.8	13.0	17.5	31.5
ec1	2.5	3.3	4.5	6.7	9.0	10.1	14.0	18.5	30.0
ec2	2.5	4.0	4.9	6.4	8.4	9.3	13.0	17.0	28.5
ec3	2.5	4.5	5.3	7.3	9.2	10.1	14.0	18.0	32.5
muComb									
bar	3.0	4.9	5.8	7.8	9.8	10.8	14.5	19.5	37.5
ec1	2.5	4.8	5.8	7.7	9.5	10.4	14.0	18.5	37.0
ec2	2.5	4.8	5.8	7.7	9.6	10.6	14.0	18.5	37.0
ec3	2.5	4.8	5.8	7.7	9.7	10.6	14.5	18.5	35.0
MuidSA	**3.00**	**4.50**	**5.38**	**7.31**	**9.21**	**10.10**	**14.20**	**18.81**	**37.72**
bar	3.00	4.40	5.28	7.22	9.17	10.15	14.06	18.83	37.96
ec1	3.00	4.59	5.39	7.24	9.09	9.94	13.57	18.10	36.70
ec2	3.00	4.64	5.55	7.42	9.49	10.29	14.04	18.66	37.35
ec3	3.00	4.65	5.57	7.47	9.39	10.37	14.34	18.95	37.90
MuidCB	**3.00**	**4.90**	**5.87**	**7.80**	**9.77**	**10.76**	**14.58**	**19.54**	**38.66**
bar	3.00	4.93	5.91	7.81	9.84	10.80	14.67	19.53	39.30
ec1	3.00	4.86	5.84	7.78	9.64	10.62	14.45	19.27	38.86
ec2	3.00	4.88	5.86	7.77	9.70	10.69	14.45	19.28	38.59
ec3	3.00	4.90	5.84	7.95	9.69	10.72	14.53	19.24	38.81

Figure 4.17. *Effective HLT thresholds, defined to obtain a 90% selection efficiency at the nominal threshold.*

rithm, are reported for all the η regions and for two different thresholds in Fig. 4.18, 4.19, 4.20, 4.21, 4.22 and 4.23.

The efficiency of MuId combined versus p_T will be shown as a function of the p_T thresholds applied in the TrigMoore hypothesis algorithms. Efficiency is defined in this case as the ratio of events with a reconstructed track from MuId combined exceeding a given p_T threshold to all events with a muon passing the LVL2 trigger (Fig. 4.24).

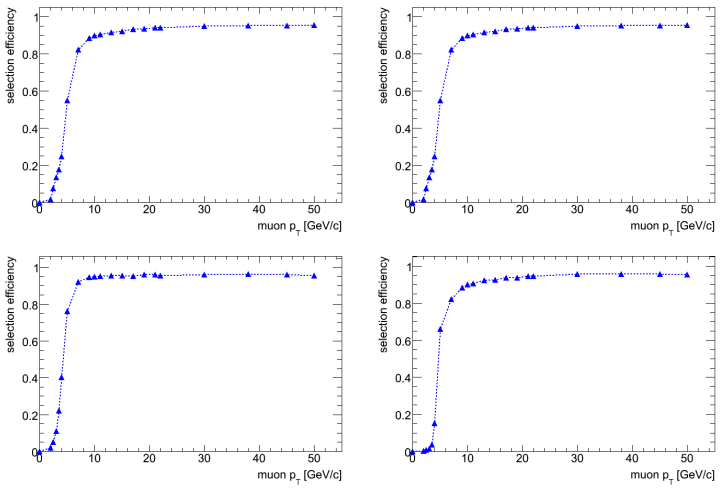

Figure 4.18. *Efficiency vs. p_T of LVL1 with respect to Monte Carlo truth for the 6 GeV threshold. Results are reported separately for different pseudorapidity regions: BAR (top-left), EC1 (top-right), EC2 (bottom-left) and EC3 (bottom-right).*

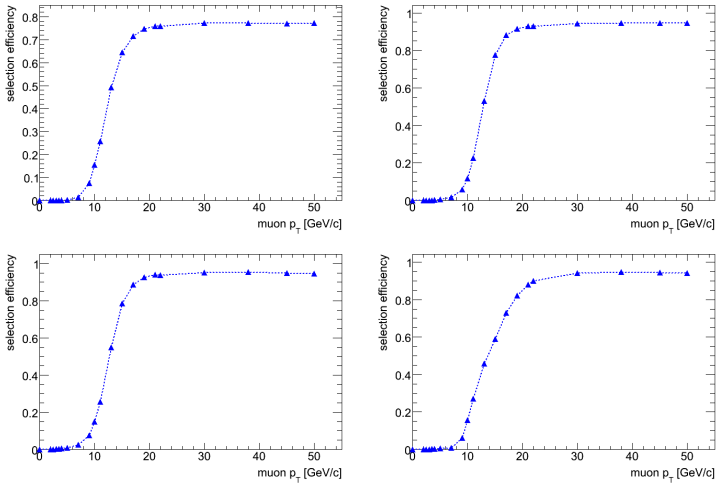

Figure 4.19. *Efficiency vs. p_T of LVL1 with respect to Monte Carlo truth for the 20 GeV threshold. Results are reported separately for different pseudorapidity regions: BAR (top-left), EC1 (top-right), EC2 (bottom-left) and EC3 (bottom-right).*

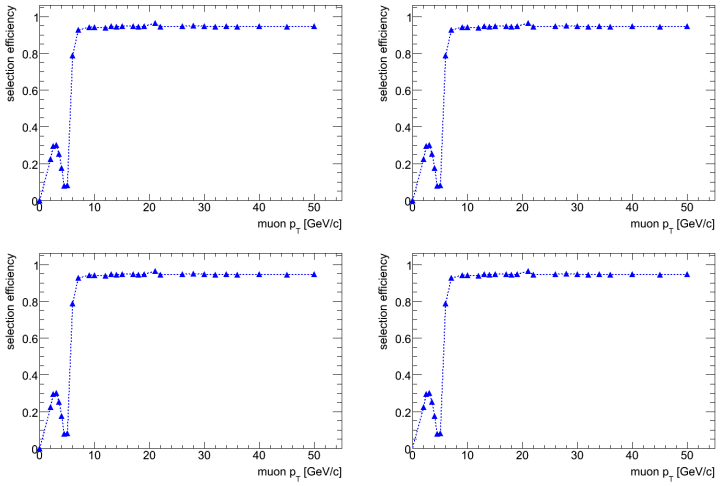

Figure 4.20. *Efficiency vs. p_T of muComb with respect to LVL1 for the 6 GeV threshold. Results are reported separately for different pseudorapidity regions: BAR (top-left), EC1 (top-right), EC2 (bottom-left) and EC3 (bottom-right).*

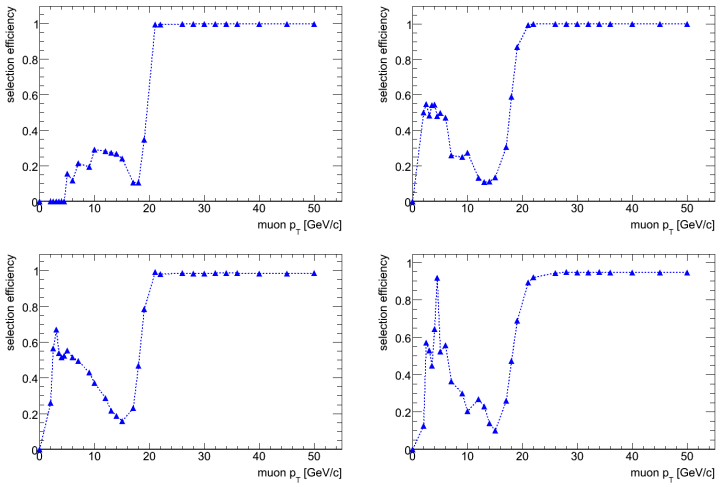

Figure 4.21. *Efficiency vs. p_T of muComb with respect to LVL1 for the 20 GeV threshold. Results are reported separately for different pseudorapidity regions: BAR (top-left), EC1 (top-right), EC2 (bottom-left) and EC3 (bottom-right).*

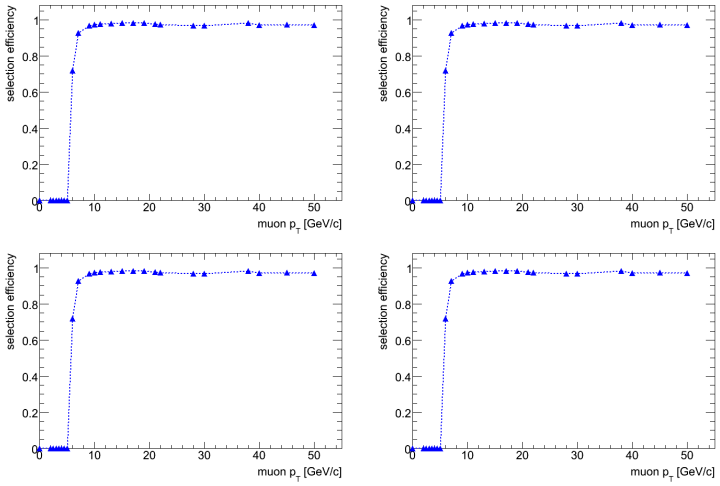

Figure 4.22. *Efficiency vs. p_T of MuidCB with respect to muComb for the 6 GeV threshold. Results are reported separately for different pseudorapidity regions: BAR (top-left), EC1 (top-right), EC2 (bottom-left) and EC3 (bottom-right).*

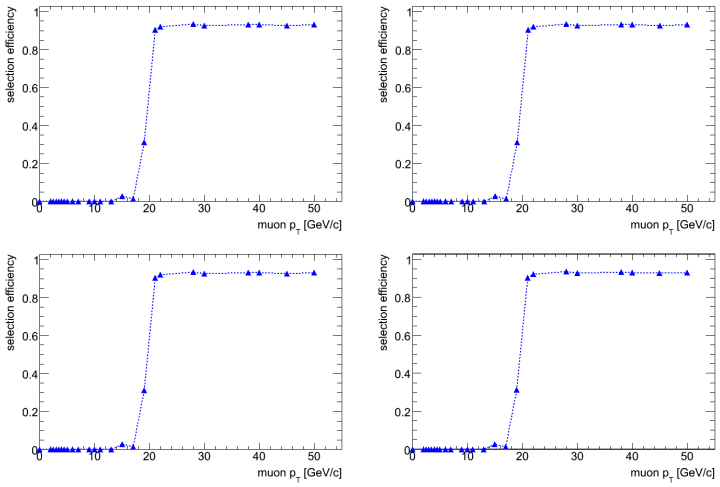

Figure 4.23. *Efficiency vs. p_T of MuidCB with respect to muComb for the 20 GeV threshold. Results are reported separately for different pseudorapidity regions: BAR (top-left), EC1 (top-right), EC2 (bottom-left) and EC3 (bottom-right).*

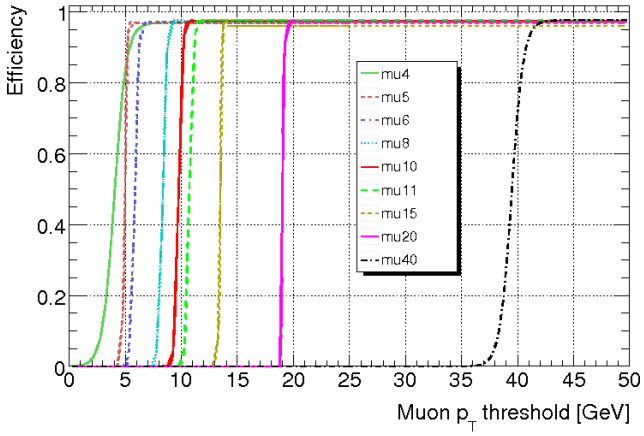

Figure 4.24. *MuId combined efficiencies with respect to LVL2 for nine different p_T thresholds: $p_T = 4, 5, 6, 8, 10, 11, 15, 20, 40$ GeV.*

4.2.3 Cavern background

The radiation generated by *pp* collisions interacts with the detector and the collider activating their material. Particles released by the materials, mainly neutrons, produce secondary time-uncorrelated photons that subsequently produce electrons, diffusing in the apparatus like a gas (a very detailed discussion of the radiation background can be found in [81]). This particle flux can contribute to the muon trigger rate by accidental coincidence of hits produced by background particles in the trigger detectors [82]. Thus, to have a conservative estimate of the physics and trigger performance, Monte Carlo simulations are done superimposing interesting physics processes with background levels, that can be multiplied by safety factors to account the large uncertainty on its estimate.

The EF performance in realistic conditions has been studied using simulated single muon samples with superimposed background, i.e. the pile-up due to the luminosity scenario and the cavern background. These kind of studies

have been extensively done on G3 samples using Athena release 8.3.0, and then repeated more recently on G4 samples with release 11.0.3. For this reason the results obtained are not directly comparable with the one shown in previous sections for single muons without noise (performed in Athena release 12.0.6). Nevertheless, they can give useful indications on the Muon Trigger performance in case of high luminosity or high cavern background. Furthermore, new G4 samples have been simulated but not yet extensively analysed due to the higher pressure on low-luminosity strategies coming from the LHC schedule. The results presented here have been obtained using the EF seeded from the LVL1 result; at the time of this study the LVL2 algorithms were not yet fully integrated in the Athena software framework.
A dedicated effort has been devoted to generate and reconstruct about $2 \cdot 10^6$ events with G3 and Athena 8.3.0, covering the muon p_T spectrum from 6 GeV/c to 1 TeV/c. In Fig. 4.25 the MOORE efficiency with respect to LVL1 (discussed in previous sections) is displayed in black when no background is added, and also the scenarios are considered in which pile-up is simulated (according to an instant luminosity of $10^{34} cm^{-2} s^{-1}$) together with cavern background (with safety factors 2, 5 and 10 with respect to the nominally expected particle flux, in red, green and blue, respectively). In Fig. 4.26 a similar plot is given for MuId Standalone: a worse degradation of the efficiency is observed in higher background environments. No relevant effects are visible on p_T, η and ϕ "core" resolution, but a gradual increase of population in the tails of pull distributions can be noticed. In Fig. 4.27 the χ^2 of MOORE tracks is shown for the four scenarios described above: a degradation of the track quality as the safety factor becomes higher is observed. Fake tracks are defined here as reconstructed tracks that satisfy the usual requirement on MOORE χ^2 (< 3) and that have been successfully extrapo-

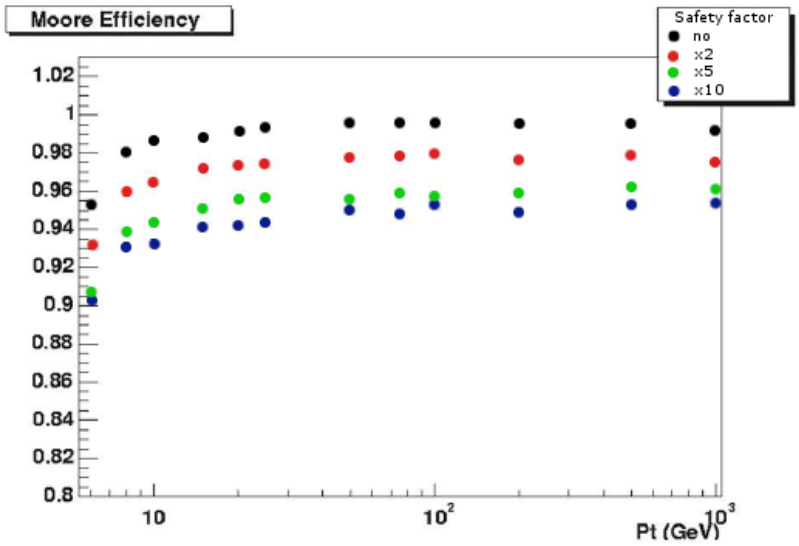

Figure 4.25. *MOORE efficiency with respect to LVL1 as a function of the muon p_T for no background (black), safety factor 2 (red), 5 (green) and 10 (blue) at $\mathscr{L} = 10^{34} cm^{-2} s^{-1}$ (Athena 8.3.0).*

lated to the vertex by MuId, but that are found outside a $5\sigma(\eta, \phi)$ acceptance cone around the true muon. fake tracks can be separated into two categories: ghost tracks determined by uncorrelated noise and real tracks due mainly to low-energy charged minimum bias particles entering the Muon System. Most of these fake tracks are short, have high χ^2 and low-p_T: this is evident from Fig. 4.28, where their p_T spectrum is shown for different single muon p_T's and for different safety factors (left), and their number of MDT+RPC hits is plotted (right) as a function of the track χ^2 (in blue), compared to 25 GeV/c good muon tracks (in red). The probability to reconstruct fake tracks in a single muon event is represented in Fig. 4.29 as a function of the muon p_T for no background and for safety factors 2, 5 and 10 at $\mathscr{L} = 10^{34} cm^{-2} s^{-1}$: a weak dependency on p_T (higher fake probability above 80-100 GeV/c) can be mainly explained as related to muon showering. Up to a safety factor 5, fake

tracks occur with a probability of few percent. Similar studies on background have been performed also on a dedicated muon background G4 production, processed with the EF in Athena release 11.0.3. The pile-up simulation

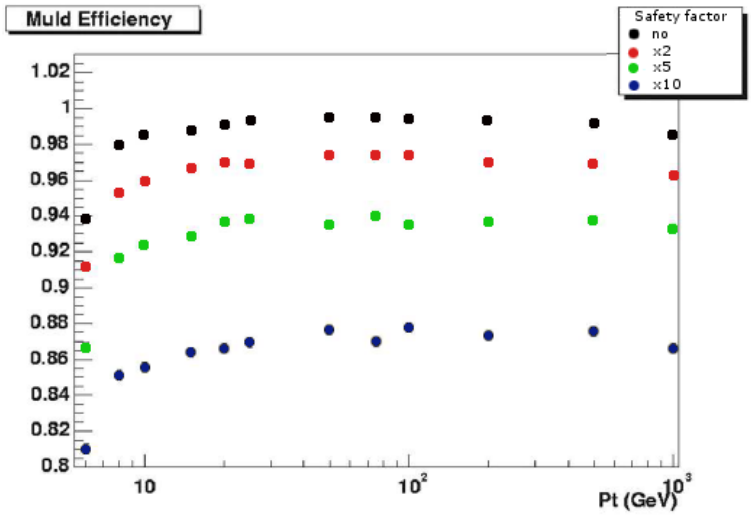

Figure 4.26. *MuId Standalone efficiency with respect to LVL1 vs. muon p_T for no background (black), safety factor 2 (red), 5 (green) and 10 (blue) at $\mathscr{L} = 10^{34} cm^{-2} s^{-1}$.*

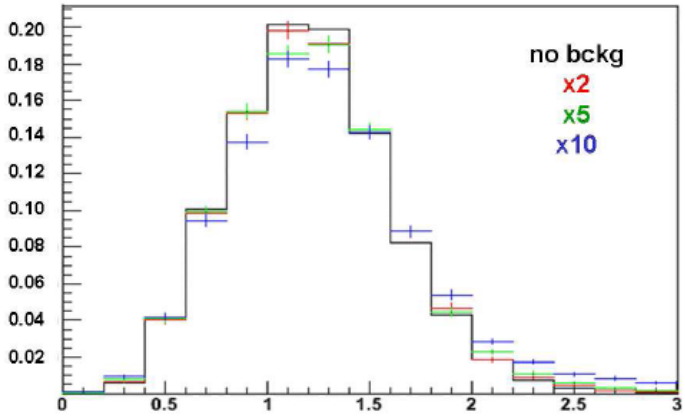

Figure 4.27. *χ^2 of MOORE tracks for no background (black), safety factor 2 (red), 5 (green) and 10 (blue) at $\mathscr{L} = 10^{34} cm^{-2} s^{-1}$.*

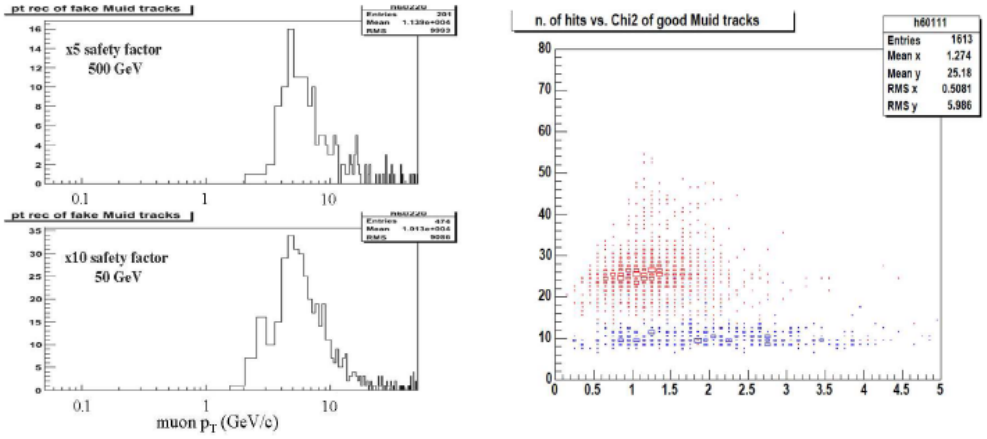

Figure 4.28. *Left: two distributions of the measured fake tracks' p_T for different safety factors when the simulated background is added to 500 GeV/c (top) and 50 GeV/c (bottom) single muons. Right: number of MDT+RPC hits vs. track χ^2 for good tracks (red) and fake tracks (blue).*

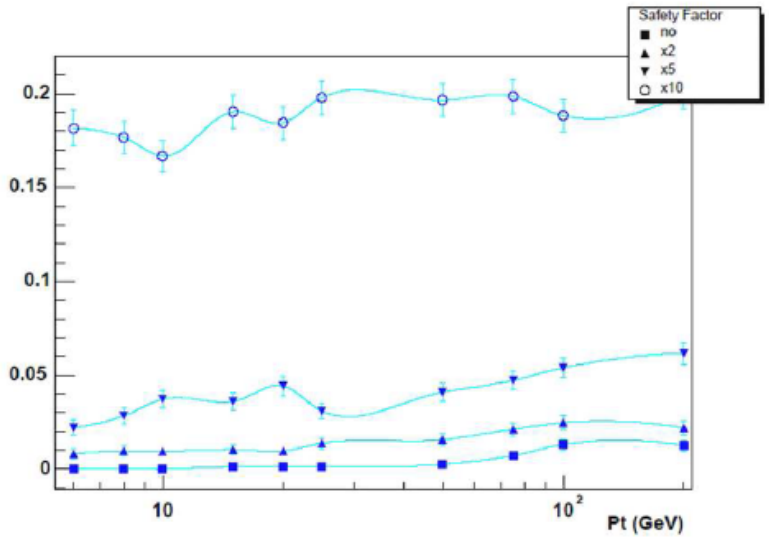

Figure 4.29. *Fake track probability in single muon events vs. muon p_T for no background and for safety factors 2, 5 and 10 at $\mathscr{L} = 10^{34} cm^{-2} s^{-1}$.*

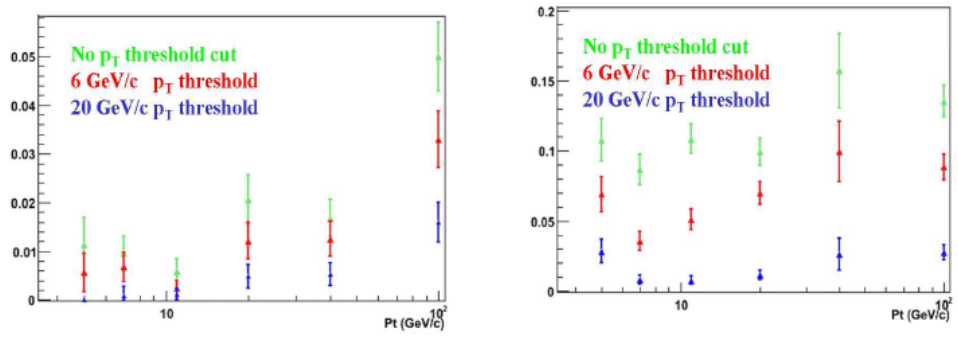

Figure 4.30. *Fake track probabilities as functions of the generated muon p_T when no cut is applied (green), and when a p_T threshold is applied (red for 6 GeV/c and blue for 20 GeV/c): pile-up is simulated for $\mathscr{L} = 10^{33} cm^{-2} s^{-1}$ and safety factors 1 and 5 are shown on the left and on the right, respectively (Athena 11.0.3).*

corresponds to a luminosity of $10^{33} cm^{-2} s^{-1}$, wile the cavern background is superimposed to the event at the nominal abundance or at a rate 5 times larger than expected. Fig. 4.30 shows the fake probability in both scenarios: the green points correspond to no cut applied on the reconstructed tracks, while the red (blue) points refer to fakes passing the 6 (20) GeV/c p_T threshold. These studies are non conclusive because the simulation of pile-up and cavern background are affected by large systematic uncertainties arising from the cavern background simulation procedure [1]. Moreover, the estimates of the trigger rate induced by fake muons in background conditions needs to be addressed in order to understand how critically the muon trigger depends on the conditions expected at high-luminosity LHC operation.

[1] G3 and G4 simulations are not fully consistent

4.3 Background rejection and rates

4.3.1 Muons from in-flight decay of π/K

From the muon flux discussed in section 4.1.1 the indication that decays in flight of light mesons are the dominant source of muons at low transverse momenta, from a few GeV up to $\sim$ 8 GeV, emerged; in the region of intermediate p_T, heavy quarks were shown to be the most important production channel. Although the rate and relative importance of the low-p_T muons is affected by very large theoretical uncertainties, it is clear that decays in flight of pions and kaons are an important source of fake single muon trigger rate at low transverse momentum and, therefore, deserve the study of a dedicated rejection strategy.

Data samples and their validation. The most suitable simulations to perform such studies would be minimum bias samples; however the probability that pions or kaons produced in low and moderate p_T QCD scattering would decay before interacting hadronically in the calorimeters is low, between 0.1% and 1% depending on the meson momentum. In order to estimate the trigger efficiency under the threshold at 3% level, where it can be of the order of 10^{-4} at the Event Filter, a sample of thousand triggering muons is required. As a consequence 10^9 events containing a light meson would be required.

In order to produce simulations with an enhanced production of charged pion and kaon decays, a dedicated tool, hereafter indicated as *PionDecayer*, has been developed. The *PionDecayer* is a procedure that can be enabled in the ATLAS implementation of Geant4 [80]. It operates on the list of charged pions and kaons with p_T above an adjustable threshold produced by the event

generator: one of these mesons, randomly chosen, is flagged with a specific value of the status code (a Monte Carlo property of each simulated particle holding information about the stability of the type of interaction that the particle is due to undergo) and it is assigned a proper time t_{decay}, defined in the particle centre of mass frame, when it is due to artificially decay. The value of t_{decay} is extracted randomly from a uniform distribution with boundaries zero and an upper value corresponding to the maximum path length of the meson inside the inner detector cavity[2], determined by its direction. The meson flagged to artificially decay is passed to the Geant4 simulation, along with all other generated particles unaffected by the *PionDecayer*, and the simulation operates on the flagged meson in an unbiased way, except for the constraint that it is not allowed to propagate in the detector longer than its artificially set life path. As a consequence, it can happen that, before decaying, the meson undergoes a hadronic interaction, leading to energy degradation and eventually to the production of new particles out of an inelastic collision. In addition, PDG [22] branching fractions are used to determine the decay mode also in case of a decay induced by the *PionDecayer*. The simulation of events without any charged meson above a defined transverse momentum threshold is aborted. The value of this p_T threshold, typically 2 GeV, defines the retained fraction of the original cross section predicted by the event generator for the input event sample.

The *PionDecayer* has been used for the production of specific samples, described below, intended to provide high statistics of light meson decays in flight for the study of the rejection power of the trigger against this kind of background as a function of the transverse momentum of the secondary muon:

[2]A cylinder of half length 350 cm and radius 115 cm

- a sample of 10^6 single pions of $p_T > 2.5$ GeV forced to decay. Their kinematics ($p_T \times \eta$) is generated according to a double differential cross section of primary pions in minimum bias events, evaluated using previous PYTHIA simulations. This sample is intended for fast processing and precise efficiency determination: the properties of the decay of interest are fully preserved while using a very simplified overall event;

- a sample of about 10^5 minimum bias events, generated with PYTHIA 6.323 and simulated with the *PionDecayer*, configured in order to select only one charged π or K with $p_T > 2$ GeV per event. This simulation provides a statistically enriched sample of decays embedded in the full complexity of a minimum bias event, where muon production can also occur naturally.

A special care must be pained when using the above samples in order to estimate accepted cross sections or trigger rates, since the abundance of forced decays needs to be reweighted for the meson decay probability, on an event by event basis. In particular, the weight to be assigned to a specific forced decay is

$$w(p_T, \eta) = R \cdot m_{\pi^\pm, K^\pm} / (p \cdot c \cdot \tau_{\pi^\pm, K^\pm})$$

where R is the distance travelled by a meson ($\pi^\pm, K^\pm$) emitted from the interaction point in the η direction before producing a hadronic shower in the calorimeters, p is the total momentum of the charged pion or kaon, m and τ are the rest frame mass and life time and c is the speed of light. In addition to the above samples, standard minimum bias, generated with PYTHIA 6.323 and 6.4 in the context of the ATLAS Computing System Commissioning effort, have been used as a valuable reference to cross check the results obtained from the dedicated productions. The transverse momentum spectra of

muons observed in minimum bias events simulated with the *PionDecayer* and single pions forced to decay are observed to be consistent, after appropriate reweighting, with each other and in agreement with previous predictions[3]. In order to make the comparison between the samples more explicit, table 4.31 summaries the cross sections predicted for $p_T > 4$ and 6 GeV in the pseudo-rapidity acceptance of the muon LVL1 trigger. The cross sections estimated from the minimum bias sample with the *PionDecayer* consist of two contributions, corresponding to events with natural decays and with forced decays. The statistical error is dominated by the huge uncertainty on the first contribution, estimated with about 30 events selected over the whole statistics, which turns out to be of the same order of the forced decay component. It has to be noticed that, apparently, the contribution of forced decays appears to be somewhat underestimated compared to the unbiased contribution. In particular, if only forced decays are used in order to extract the fraction of $\pi^{\pm}, K^{\pm}$ with $p_T > 2$ GeV decaying into muons of $p_T > 4$ GeV as a function of p_T, by reweigthing this meson spectrum for this efficiency and for the decay probability inside the ID boundaries (even adding one extra interaction length to the meson mean path), the resulting rate of muons above 4 GeV in the trigger acceptance ($|\eta| < 2.4$) is lower than the result in Fig. 4.31 by about 30%. Nevertheless, in spite of the large statistical uncertainties and of any systematic biases induced by the treatment of forced decays, the discrepancies observed are below the large statistical uncertainties on the low p_T physics underlying this kind of processes and, therefore, they can be considered of minor importance for the purposes of trigger studies.

[3]Depending on the $p_T \times \eta$, region the various predictions differ by no more than a factor of two. No systematic trends are clearly visible that might point to specific systematic effects.

$\sigma(\mu b)$	PYTHIA 5.7		DPMJET-II		PYTHIA 6		PYTHIA 6+*PD*	
	$\pi^{\pm}$	K	$\pi^{\pm}$	K	$\pi^{\pm}$	$K^{\pm}$	$\pi^{\pm}$	$K^{\pm}$
$p_{T\mu} > 4$GeV/c	5.7	4.1	9.1	8.2	5.4± 1.2	8.9 ± 1.5	5.7 ± 1.0	5.4 ± 1.1
$p_{T\mu} > 6$GeV/c	0.79	0.61	1.16	1.03	0.8± 0.5	1.3 ± 0.6	1.2 ± 0.6	1.9 ± 0.6

Figure 4.31. *A comparison of predictions for muon production cross sections from decays in flight of light mesons within kinematic regions of interest for the muon trigger (a cut to $|\eta_\mu| < 2.4$ is applied). A normalisation of 80 mb is assumed, in all cases, for the total inelastic minimum bias cross section. The first and second columns report the results obtained by integrating the parametrisations of the double differential cross section historically used to estimate muon trigger rates. The cross section observed on limited statistics of standard CSC minimum bias simulation, by event counting, is reported in column three. Finally, the predictions from the sample of minimum bias events simulated with the PionDecayer are also shown.*

Rejection strategy at the Event Filter The fraction of fake muons retained at the EF, normalised to the LVL2 accepted events, for the 6 GeV threshold, has been measured as a function of the muon transverse momentum by processing the single pion sample with the standard LVL1 and HLT emulation chain. The result, reported in Figure 4.32, shows a very poor rejection capability for muons coming from pion decays, which demonstrates that the standard muon identification procedures are not very sensitive, as expected, to the small kink between the pion and muon tracks. The kinematics of charged kaon two-body decays, which are the dominating kaon contribution to the muon rate, is much more favourable to an easier rejection, due to the larger average value of the angle between the kaon and the muon tracks. In order to improve the rejection capability, the more difficult background of muons from pion decays has been scrutinised, trying to identify additional measured parameters providing some discriminating power

between background and primary muons. The variables considered here are the following:

- the impact parameter d_0 of the track reconstructed in the inner tracker; the width of the distribution of such parameter depends on the resolution of the ID reconstruction; low quality reconstructed tracks,with hits produced before and after the decay kink, exhibit spoiled resolution on the impact parameter; moreover, in case only the hits associated to the muon track are actually used in the fit, the impact parameter would be an indirect measurement of the decay kink;

- as a consequence of the kink some hits in the ID, most probably those at the entrance of the inner tracker, might constribute with high residuals to the track and, therefore, they might be discarded by the fitting procedure; for this reason the number of hits associated to the track in the Pixel Detector, the existence of a hit in the pixel B-layer and,

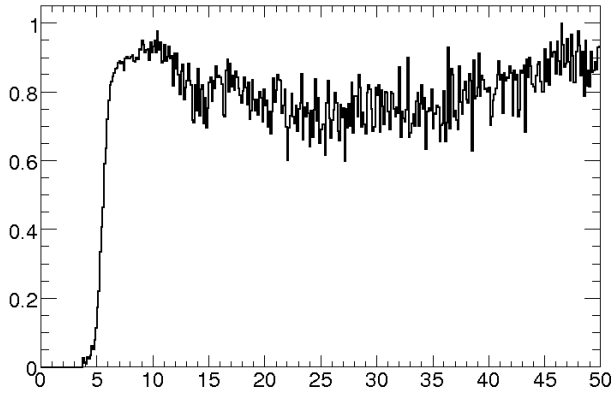

Figure 4.32. *Event Filter efficiency, as a function of the muon* p_T*, with respect to LVL2 accepted events for the transverse momentum threshold of* 6 *GeV measured for muons coming from decays in flight of pions.*

finally, the number of associated hits in the Silicon Tracker have been studied in single muons samples and in muons from pion decays;

- the ratio between the transverse momentum reconstructed in the inner tracker and in the muon spectrometer, after back-extrapolation to the interaction point and correction for the measured energy loss in the calorimeters, is ideally symmetrically distributed around 1; in case of fake muons from pions, in addition to a degradation of the resolution in the inner tracker, the kinematic mismatch of transverse momentum between the decaying meson and the muon can lead to a tail at high values; due to the steeply falling p_T spectrum of charged particles in minimum bias events, this behaviour is enhanced at high transverse momentum;

- the matching χ^2 between the tracks reconstructed in the muon spectrometer and the track reconstructed in the inner tracker is clearly a valuable discriminating variable, in case the ID track is mostly built out of hits produced by the decaying meson.

The discrimination power of each variable has been studied by measuring the fraction of accepted events as a function of the cut applied, for isolated muons and for fake muons above a given transverse momentum threshold. The results, shown in Figure 4.33, are based on the simulations of single muons and single pions with forced decays. For each variable, the fraction of events retained after the cut is normalised to the statistics of events passing the EF reconstruction, before the application of any hypothesis algorithm. In addition, only events with a single muon reconstructed at the EF and a single track in the ID are considered in the reference sample. These simplifying analysis conditions, which leave almost unaffected the single muon

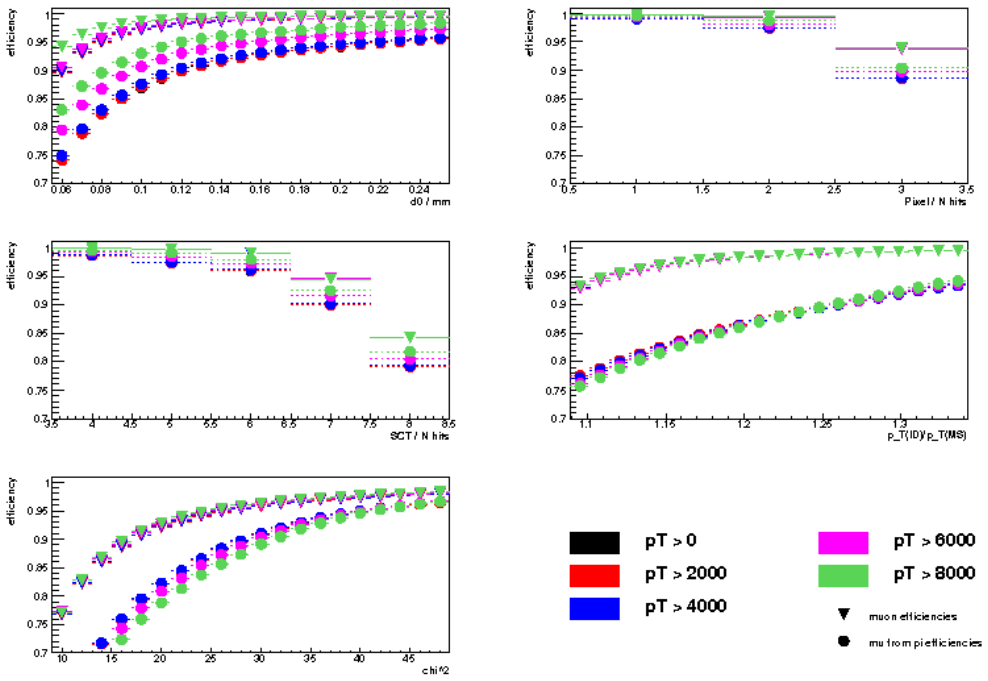

Figure 4.33. *Efficiency for direct muons (indicated by tringles) and muons from pion decays (indicated by circles) as a function of the cut on some discriminating variables. In clockwise order, from the top left: efficiency as a function of* d_0*, number of Pixel hits,* $p_T(ID)/p_T(MS)$*, matching* χ^2*, number of SCT hits.*

sample, are considered to affect the result of the study in the direction of a more conservative estimate of the rejection power for fake muons. From the analysis the exclusive rejection power of the individual variables, a set of cuts, listed below, has been defined, trying to contain the loss of efficiency for single muons while reducing the fraction of accepted background:

- $|\mathrm{d_0}| < 0.15$ mm, $\mathrm{N_{hits}(B_{layer})} \geq 1$, $\mathrm{N_{hits}(Pixel)} \geq 3$, $N_{hits}(SCT) \geq 6$,
- $\mathrm{p_{TID}/p_{TMS}} > 1.25$, $\chi^2_{\mathrm{matching}} \leq 26$.

In particular, these values have been chosen by considering efficiency and rejection at $\mathrm{p_T} = 4$ GeV, in the assumption that a different choice of the

cuts might be optimised for each muon trigger element in the trigger menu.

From the application of these cuts on the reference sample of events accepted at the EF, the efficiency for primary muons and fake muons (from decays in flight of charged pions) shown in Figure 4.34 have been obtained. A loss of efficiency contained between 25% at the threshold (4 GeV) and 10% at 20 GeV allows to reduce the acceptance for the most difficult background source to 60% at the threshold and 80% at high transverse momentum. Since the expected rejection of muons from charged kaon decays is higher, this scenario might be worth for the seek of obtaining an affordable trigger rate at the very low threshold of 4 GeV by reducing mostly the rate from uninteresting events while preserving a reasonable efficiency for prompt muons. An optimisation of the cuts, with a specific tuning for each trigger element, might eventually improve the signal over background ratio.

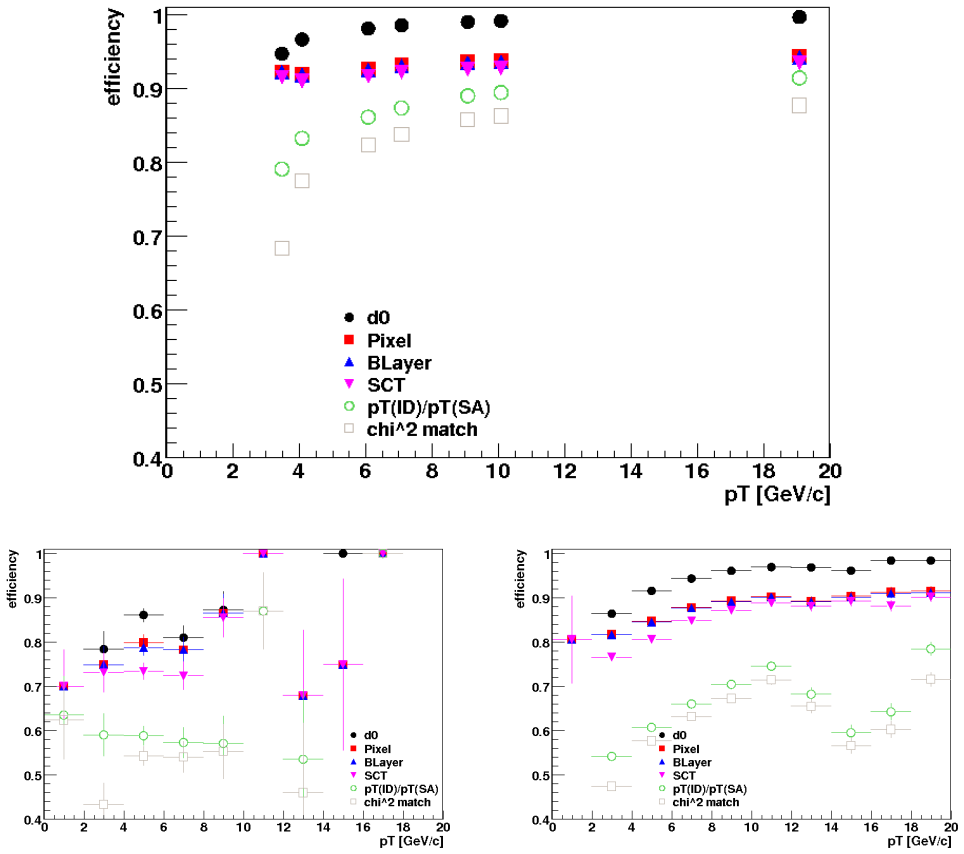

Figure 4.34. *Efficiency for muons passing the whole trigger selection up to the Event Filter, after the application of further cuts on variables discriminating fake muons from decays in flight of light mesons. Results on single muons are shown in the top plot, on minimum bias in bottom-left plot and on muons from pion decays in the bottom-right plot. Each efficiency curve shows the data reduction obtained by the addition of the corresponding cut to the whole selection procedure. The specific values of the cuts applied are discussed in the text.*

4.3.2 Rates

In the present work two different approaches have been used in order to estimate the single muon trigger rates from MC data samples: one is indicated as *convolution method*, the other one is referred as *counting method*.
The **convolution method** uses the estimate of the differential cross sections $d\sigma/dp_T$ for single muon production processes (as reported in Fig. 4.1 and 4.2) and of the muon trigger efficiencies (discussed in detail in Sec. 4.2.2). The expected output rate at the muon trigger can be written as:

$$R_i = \mathscr{L} \int_{p_T^{min}}^{p_T^{cutoff}} \frac{d\sigma}{dp_T} \varepsilon_i(p_T) dp_T \quad , \tag{4.2}$$

where $\mathscr{L}$ is the instantaneous luminosity, the index i indicates the i-th source of muons, p_T^{min} is the minimum p_T used for the parametrisation, p_T^{cutoff} is an upper limit (set to 50 GeV for the processes studied here) and ε_i is the efficiency for the i-th channel, which can be factorised in three terms , one for each trigger level with respect to the previous level:

$$\epsilon_i = \epsilon_i^{LVL1} \cdot \epsilon_i^{LVL2} \cdot \epsilon_i^{EF} \quad . \tag{4.3}$$

This method has the advantage of decoupling the knowledge on trigger (efficiency) and on physics (cross sections), and the disadvantage that trigger performance against non-prompt muons need accurate studies, like shown for the case of muons from in-flight decay of π/K. For these reasons, as a first estimate of the rates, a simplified approach can be followed, using only the *single muon efficiency* ($\varepsilon_{\mu_{single}}$) for all the production channels ($\forall i \quad \epsilon_i = \epsilon_{\mu_{single}}$).
A FORTRAN routine, named **muonrates**, has been adapted and used for the evaluation of the muon rates with the convolution method. The parametrisation used in muon rates for the differential cross sections are the same presented in [79]; trigger efficiency curves versus p_T can be separately defined for each muon production channel. The routine was provided with

Minimum bias datasets	
Dataset	Events
misal1_mc12.005001.pythia_minbias.digit.RDO.v12000701	$8{\cdot}10^5$

Table 4.1. *Minimum bias data samples used for the analyses.*

efficiencies for all the muon trigger levels, in particular LVL1 with respect to MC truth, muComb with respect to LVL1 and MuidCB with respect to muComb. These efficiencies were parametrised in η and p_T: for each η region (BAR, EC1, EC2 and EC3) the efficiency versus p_T (between 0.5 and 50 GeV) is evaluated by steps of 0.5 GeV.

A more general approach for the calculation of the trigger rates is based on the use of the definition:

$$R_i = \mathscr{L} \cdot \frac{N_i^{selected}}{N_i^{generated}} \cdot \sigma_{tot} \quad , \tag{4.4}$$

where $\mathscr{L}$ is the instantaneous luminosity, N_i is the number of muons (generated or selected) for the $i-$th production channel and σ_{tot} is the total cross section of the data sample used. This method is based on a **direct counting** and needs the simulation huge data samples inclusive of all the most relevant production processes, i.e. accurate minimum bias simulations. Dataset used for our studies are reported in Tab. 4.1.

The muon trigger rates estimated with this method using PYTHIA 6.4 simulations of minimum bias events and assuming a total inelastic cross section σ_{tot} of 80 mb will be presented in the next section.

Both methods discussed here give results which are highly dependent on the theoretical parametrisation of the physics processes involved. In the case

of [79] the predictions at the TEVATRON centre of mass energy, resulting from the same theoretical input used for the ATLAS muon trigger studies, have been shown to be in satisfactory agreement with $D\varnothing$ data (results from $D\varnothing$ collaboration can be found in [83]); however, the extrapolation to LHC energies introduces significant uncertainties. The estimated uncertainty in the pp inelastic cross-section is about 30%, while the total uncertainty on the main background processes could be as large as a factor of two (inclusive jet production at low-p_T) to five ($b, c \rightarrow \mu X$ events).

The use of recent event generators has shown a different behaviour for the production cross sections of muons from heavy flavors. In particular, in Fig. 4.35 is reported the comparison between the integrated cross sections as a function of p_T for the processes $b\bar{b} \rightarrow mu6X$ and $c\bar{c} \rightarrow mu6X$ as obtained from Pythia 6.403 (the most up-to-date estimation) and from Pythia 5.7 (used for the ATLAS Physics TDR). At present, the contribution to the muon cross-section given by b quarks is higher than from c quarks (in contrast with the values given in the ATLAS TDR and used until now), and also higher than the contribution from in-flight decays of light mesons. These recent results require a more accurate study and, probably, will influence the definition of the trigger menus for the low-luminosity runs.

Results

The rates obtained for some low and high-p_T thresholds in the barrel and in the endcaps after LVL1, muFast, muComb and EF selection are shown in Tables 4.2, 4.3, 4.4 and 4.5. For each considered p_T threshold, results are given normalised to different integrated luminosities, according to expected period of interest of the threshold during the ATLAS data taking.

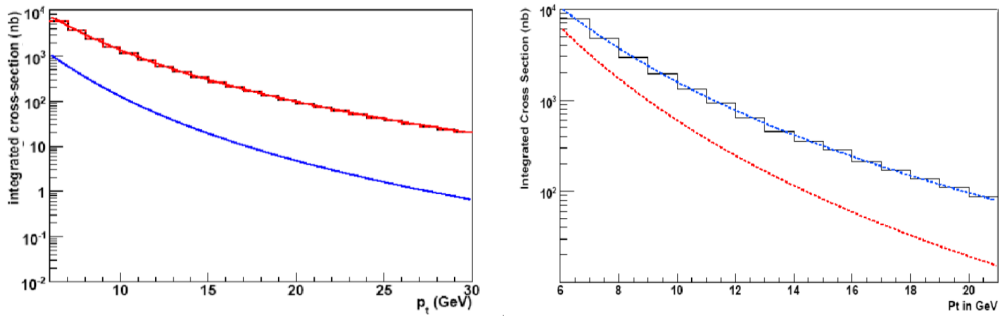

Figure 4.35. *Recent (and preliminary) results from B-physics groups which show the disagreement between the total cross sections for $b\bar{b} \rightarrow mu6X$ (left) and $c\bar{c} \rightarrow mu6X$ (right) with respect to previous results used until now to evaluate the trigger rates. In red is shown the parametrisation, as obtained using Pythia 6.403, while in blue is shown the parametrisation from Pythia 5.7 (used in the ATLAS Physics TDR [19]).*

Rate values reported in the tables are affected by statistical errors which range from 5 to 10%, while systematic uncertainties are dominated by the lack of knowledge of cross sections, as already discussed in Sec. 4.1.1. In Fig. 4.36 the total (barrel+endcaps) EF rates at $\mathscr{L} = 10^{31}$ cm^{-2} s^{-1} are reported as a function of the p_T threshold applied.

The convolution and counting methods described in the previous section give EF final rates in good agreement between themselves, within statistical errors due to the limited size of the minimum bias sample, starting from p_T threshold of 6 GeV/c. The values obtained with the counting for lower p_T thresholds (4 and 5 GeV/c) are smaller by a factor of $\sim$2 for muons from π/K decays with respect to the convolution (provided by DPMJET). To keep uniformity among the rate results, mostly provided by PYTHIA 6.403, the final EF rates quoted in tables for the 4 and 5 GeV/c thresholds are the ones obtained with the counting procedure.

Among the results other sources of single muon rates are not reported if considered negligible, such as the case of the top, whose contribution is significant (but anyway lower than the percent level) only in the highest p_T threshold (40 GeV/c) at the Event Filter.

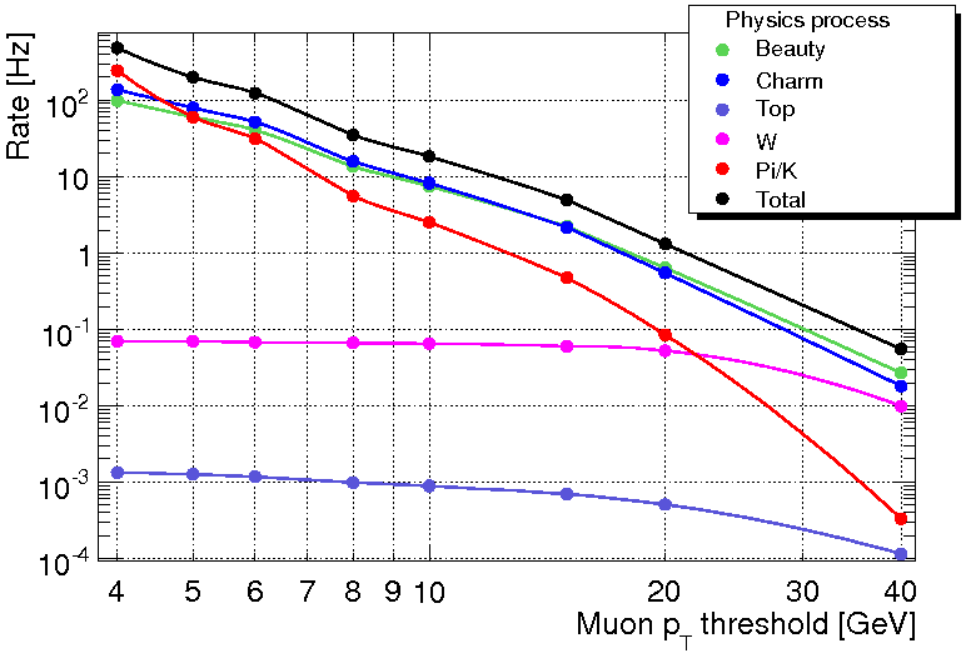

Figure 4.36. *Expected EF rates at* $\mathscr{L} = 10^{31}\ cm^{-2}\ s^{-1}$ *for single muon processes as functions of muon* p_T *threshold integrated over* $\eta < 2.4$.

LVL1 muon trigger rates				
$\mathscr{L} = 10^{31}$	"Cosmic"		5 GeV	
$cm^{-2}s^{-1}$	Barrel (Hz)	Endcaps (Hz)	Barrel (Hz)	Endcaps (Hz)
π/K	454	199	162	81
beauty	85	74	54	53
charm	124	104	76	73
W	0	0	0	0
TOTAL	663	377	292	207
$\mathscr{L} = 10^{33}$	6 GeV		8 GeV	
$cm^{-2}s^{-1}$	Barrel (Hz)	Endcaps (Hz)	Barrel (Hz)	Endcaps (Hz)
π/K	8600	5300	5200	2200
beauty	4400	5100	3300	2900
charm	6100	6900	4400	3800
W	3	4	3	4
TOTAL	19100	17300	12900	8900
$\mathscr{L} = 10^{34}$	20 GeV		40 GeV	
$cm^{-2}s^{-1}$	Barrel (Hz)	Endcaps (Hz)	Barrel (Hz)	Endcaps (Hz)
π/K	1100	3800	470	1900
beauty	2500	4000	1100	1300
charm	2800	4700	1200	1400
W	26	41	23	33
TOTAL	6400	12500	2800	4600

Table 4.2. *Single muon trigger rates as obtained at LVL1 , for different low and high-p_T thresholds, respectively at $\mathscr{L} = 10^{33}cm^{-2}s^{-1}$ and $\mathscr{L} = 10^{34}cm^{-2}s^{-1}$.*

LVL2 (muFast) muon trigger rates				
$\mathscr{L} = 10^{31}$	4 GeV		5 GeV	
$cm^{-2}s^{-1}$	Barrel (Hz)	Endcaps (Hz)	Barrel (Hz)	Endcaps (Hz)
π/K	190	140	82	120
beauty	50	67	37	59
charm	70	94	49	81
W	0	0	0	0
TOTAL	310	301	168	260
$\mathscr{L} = 10^{33}$	6 GeV		8 GeV	
$cm^{-2}s^{-1}$	Barrel (Hz)	Endcaps (Hz)	Barrel (Hz)	Endcaps (Hz)
π/K	4300	3700	840	1500
beauty	3000	3900	1000	2200
charm	4000	5200	1300	2900
W	3	4	3	4
TOTAL	11300	12800	3143	6604
$\mathscr{L} = 10^{34}$	20 GeV		40 GeV	
$cm^{-2}s^{-1}$	Barrel (Hz)	Endcaps (Hz)	Barrel (Hz)	Endcaps (Hz)
π/K	410	1800	200	690
beauty	540	1500	87	280
charm	520	1700	83	290
W	24	38	17	23
TOTAL	1494	5038	387	1283

Table 4.3. *Single muon trigger rates as obtained at LVL2 muon standalone, for different low and high-p_T thresholds, at $\mathscr{L} = 10^{31}cm^{-2}$, $\mathscr{L} = 10^{33}cm^{-2}s^{-1}$ and $\mathscr{L} = 10^{34}cm^{-2}s^{-1}$. The large expected rate in particular in the endcap region is caused by the relatively low rejection for low momentum muons. This is expected to improve with more recent (13.0.X) versions of the ATLAS trigger simulation and reconstruction programs.*

LVL2 (muComb) muon trigger rates				
$\mathscr{L} = 10^{31}$	4 GeV		5 GeV	
$cm^{-2}s^{-1}$	Barrel (Hz)	Endcaps (Hz)	Barrel (Hz)	Endcaps (Hz)
π/K	130	124	44	55
beauty	48	66	31	45
charm	66	91	41	61
W	0	0	0	0
TOTAL	244	281	116	161
$\mathscr{L} = 10^{33}$	6 GeV		8 GeV	
$cm^{-2}s^{-1}$	Barrel (Hz)	Endcaps (Hz)	Barrel (Hz)	Endcaps (Hz)
π/K	3500	2600	400	530
beauty	2700	3400	660	1100
charm	3800	4400	780	1300
W	3	4	3	4
TOTAL	10000	11000	1840	2900
$\mathscr{L} = 10^{34}$	20 GeV		40 GeV	
$cm^{-2}s^{-1}$	Barrel (Hz)	Endcaps (Hz)	Barrel (Hz)	Endcaps (Hz)
π/K	68	890	6	310
beauty	320	830	31	92
charm	280	840	26	99
W	22	4	7	12
TOTAL	690	2560	70	513

Table 4.4. *Single muon trigger rates as obtained at LVL2 muon combined, for different low and high-p_T thresholds, respectively at $\mathscr{L} = 10^{31}cm^{-2}s^{-1}$, $\mathscr{L} = 10^{33}cm^{-2}s^{-1}$ and $\mathscr{L} = 10^{34}cm^{-2}s^{-1}$.*

Event Filter muon trigger rates (Muid Combined)				
$\mathscr{L} = 10^{31}$	4 GeV		5 GeV	
$cm^{-2}s^{-1}$	Barrel (Hz)	Endcaps (Hz)	Barrel (Hz)	Endcaps (Hz)
π/K	125	119	36	25
beauty	44	56	27	33
charm	60	76	36	43
W	0	0	0	0
TOTAL	229	251	99	101
$\mathscr{L} = 10^{33}$	6 GeV		8 GeV	
$cm^{-2}s^{-1}$	Barrel (Hz)	Endcaps (Hz)	Barrel (Hz)	Endcaps (Hz)
π/K	1900	1200	290	260
beauty	1900	2200	550	800
charm	2400	2800	640	930
W	3	4	3	4
TOTAL	6200	6200	1480	1990
$\mathscr{L} = 10^{34}$	20 GeV		40 GeV	
$cm^{-2}s^{-1}$	Barrel (Hz)	Endcaps (Hz)	Barrel (Hz)	Endcaps (Hz)
π/K	50	40	0.1	0.2
beauty	220	380	10.5	16.3
charm	260	330	7.1	11.1
W	20	30	3.9	6.1
TOTAL	550	780	21.7	33.8

Table 4.5. *Single muon trigger rates as obtained at Event Filter (Muid Combined), for different low and high-p_T thresholds, at $\mathscr{L} = 10^{31}cm^{-2}s^{-1}$, $\mathscr{L} = 10^{33}cm^{-2}s^{-1}$ and $\mathscr{L} = 10^{34}cm^{-2}s^{-1}$.*

4.3.3 Trigger Menus

The purpose of the trigger menus is to maximise the collection of events with interesting signatures, simplify the commissioning and monitoring of the trigger, and allow an accurate detector calibration. We can distinguish between two main categories: *physics motivated triggers* and *specialised triggers*. Moreover, there are two kinds of sequences that can be configured:

- *active selections*, possibly randomly prescaled, intended for triggering on interesting events; when the rate of the corresponding signature exceeds the expected fraction of bandwidth, it is possible to randomly suppress some of the accepted events depending on a suitable "prescale" factor;

- *monitoring trigger sequences*, which typically correspond to standard HLT selections where the actual decision (evaluated in the hypothesis algorithms) is not applied. For a standard trigger sequence, a fraction of the events in input to a given trigger algorithm can be forced to pass any decision step in the rest of the trigger chain. Such events are "passing through" the selection being flagged for HLT monitoring purposes.

Different trigger menus are conceived for the different luminosity scenarios and physics studies. Physics-oriented trigger menus are determined by the best compromise between efficiency for physics channels and affordable trigger rate (see Sec. 4.3.2).
The menus reported in the following are based on Monte Carlo simulations and will be fine tuned using the first ATLAS data.
At the time of writing, the trigger strategy at low-luminosity is the best understood. At 10^{31} cm^{-2}s^{-1} and 10^{32} cm^{-2}s^{-1} luminosities, it will be very im-

portant to trigger at low-p_T for B-physics studies (the mu4 and mu6 thresholds) and to use special items to understand and debug the trigger selection. Furthermore, in addition to select data for physics and HLT commissioning, it is necessary to make sure that efficiency measurements, calibrations and monitoring procedures can be performed with the required statistics.

HLT commissioning requirements. The first phase of the HLT commissioning has to be performed before LHC collisions, requiring dedicated technical and cosmic-ray runs, mainly to check data access and data converters, and the muon detectors cabling maps. Furthermore the comparison with the offline will help to find dead or hot channels and eventual other problems by checking the monitoring histograms.
The second part of the HLT commissioning will be performed with collisions, running the selection in transparent mode (only flagging the events) and verifying the absence of eventual biases/errors by re-running the HLT algorithms in the offline environment. At the beginning, the selection will be configured with a very simple logic and with loose cuts and, in order to understand the acceptance of the selection, the muon HLT will run in standalone mode, without performing the combined reconstruction.
After the muon detectors are adequately understood, it will be possible to start the optimisation of the selection, requiring more stringent criteria and progressively increasing the complexity of the HLT chains. The commissioning and optimisation of the combined reconstruction will be performed at this stage, taking care of the alignment of the MS with the ID and also studying the isolation performance. It will be also possible to study the trigger efficiency using unbiased triggers (e.g. jet triggers).

Efficiency, monitoring and calibration requirements. Another important requirement to be satisfied is the possibility to evaluate the trigger efficiency and to collect an adequate amount of data to monitor the selection and calibrate the detectors. It is possible to measure the muon trigger efficiency using the decay $Z \rightarrow \mu\mu$, which can be easily triggered using the item mu20. To reach a statistical uncertainty of the order of 1%, 1500 $Z \rightarrow \mu\mu$ events (1 pb^{-1}) are required. At 10^{33} cm^{-2}s^{-1} luminosity, considering standard trigger efficiency, the $Z\mu\mu$ rate is $\sim$ 0.6 Hz. Moreover, to monitor the Event Filter using standard Data Quality tools, it is necessary to collect $\sim$ 10000 muon tracks (collected in $\sim$ 2 minutes at 50 Hz).
The calibration of the MDT chambers will require a large statistics of muons: the optimal rate for the calibration procedure is about 1 kHz. A special selection schema has been designed in order to output the minimal required amount of data in a dedicated data stream for events passing at LVL2 a low-p_T threshold. At very low luminosity, in order to reach the necessary statistics, it might be necessary to configure the LVL2 selection in pass-through mode.

Muon trigger menu at 10^{31} cm^{-2}s^{-1}. The menus table presented in Tab. 4.6 is the result of iterative refinements, balancing the affordable rate, the physics requirements and the technical aspects of the implementation.
As shown in the table, the item mu4, is prescaled at the EF in order to retain 1/30 of the accepted events (PS=30). Moreover, one over hundred of the events in input to LVL2 is flagged as "pass-through" (PT=100) and, therefore, it is accepted by the Level-2 and the EF, whatever the trigger decision is. The mu4 output will contain events with very low-p_T for B-physics, will allow the MDT calibration and the monitoring of the HLT selection.

Muon Trigger Menu at $L = 10^{31}\text{cm}^{-2}\text{s}^{-1}$						
Item	LVL1	rate(Hz)	LVL2		EF	rate(Hz)
mu4	PS=1	~ 1000	PS=1	PT=1000	PS=30	20
mu6	PS=1	224	PS=1	PT=200	PS=3	17
mu10	PS=1	112	PS=1	PT=100	PS=1	8
mu15	PS=1	19	PS=1	PT=20	PS=1	2
mu20	PS=1	14	PS=1	PT=0	PS=1	< 1
mu20_passHLT	PS=1	14	PS=1	PT=1	PS=1	14
mu40	PS=1	8	PS=1	PT=1	PS=1	8
2mu4	PS=5	4	PS=1	PT=1	PS=1	4
2mu6	PS=1	4	PS=1	PT=1	PS=1	4
2mu10	PS=1	< 1	PS=1	PT=0	PS=1	< 1
2mu20	PS=1	< 1	PS=1	PT=1	PS=1	< 1

Table 4.6. *Table showing the muon trigger menu for L=10^{31} $cm^{-2}s^{-1}$. PS indicates the "Prescale" factor applied, PT the "Pass-Through" factor (1/PS and 1/PT are the fraction of events collected).*

The mu6 item has PS=3 at the EF level to limit the output rate, while conserving the potential for B-physics, and a PT=200 at LVL2, that will allow to collect data for the HLT monitoring at a rate of 1 Hz.
The other items in the table are not prescaled because they give rise to affordable rates. For mu10 and mu15 the PT factors 100 and 200, respectively, allow further trigger studies. Finally, the item mu20_passHLT is designed to accept all the MU20 Level-1 triggers at the HLT.

The trigger menu described here is only a first implementation, consistent with general physics and calibration requirements and with HLT constraint,

but it has to be considered as a starting point for further optimisations. However, before data taking, it is important to reach a proposal as flexible and redundant as possible in order to avoid changing trigger thresholds with time, being able to cope with real data taking conditions by adjusting prescale factors. Threshold stability is particularly important at Level-1, where the possible configurations are limited. On the other hand, the machine luminosity and the background conditions will actually change with time. Moreover, the HLT commissioning and optimisation will be complicated by initial problems of the detectors and possible instability of the DAQ system. Finally, even the Offline reconstruction and analysis (which should provide a benchmark for the trigger performance) will initially suffer of effects induced by miscalibrations and misalignments.

Conclusions

The ability to trigger efficiently muons is one of the challenges at the LHC, in fact high-p_T leptons are a clear signature of possible new physics at TeV scale and of Standard Model processes. The unprecedented event rate, the large amount of physics and accidental background and the high suppression of the cross sections of interesting processes puts tight requirements on the performance of the Muon Trigger.

In this thesis the main aspects of the ATLAS Muon Trigger have been presented and a detailed discussion of the selection at the Event Filter level is given. The results are updated to the most recent data challenge of ATLAS concerning the software suite, the configuration of the selection algorithms and the simulated data samples. After showing the ATLAS physics reach with emphasis to the channels with muons in the final state, the main sources of background muons have been discussed.

The study of the muon Event Filter performance and of the full muon Trigger chain with huge simulated data samples, in terms of resolutions and efficiencies, is used to define and estimate the expected trigger rate for various luminosity scenarios and for all the envisaged p_T thresholds.

During the first period of running the ATLAS community will start the commissioning of the detector with collision data and pursue a dedicated low-p_T physics program. For this reason the luminosity scenario $L = 10^{31}\text{cm}^{-2}\text{s}^{-1}$

has been included in the present study together to the standard 10^{33} and 10^{34}. The detailed evaluation of the muon rates will be used to optimise the trigger menus for these different scenarios.

Together with the main trigger selection strategies, which are extensively discussed, a detailed study for the rejection of muons from in-flight decay of light mesons is presented. The present study shows that the main physics requirements are satisfied by the muon trigger which, then, will be ready to provide data for physics analysis and detector optimisations as soon as proton beams will be available.

Bibliography

[1] H. Weyl, "Elektron und Gravitation.", Zeit f. Physik **56** (1929) 330.

[2] F. Halzen and A.D. Martin, "Quarks and Leptons: An Introductory Course in Modern Particle Physics.", John Wiley & Sons, 1984.

[3] D.H. Perkins, "Introduction to High Energy Physics.", Cambridge University Press, 4th edition, 2000.

[4] I.S. Hughes, "Elementary Particles.", Cambridge University Press, 3rd edition, 1991.

[5] S. Weinberg, "A Model of Leptons.", Phys. Rev. Lett. **19** (1967) 1264.

[6] S. Glashow, "Partial Symmetries Of Weak Interactions.", Nucl. Phys. B **22** (1961) 579.

[7] S. Glashow, J. Iliopulos and L. Maiani, "Weak Interactions with Lepton-Hadron Symmetry.", Phys. Rev. D **2** (1970) 1285.

[8] M. Kobayashi and T. Maskawa, "CP-Violation in the Renormalizable Theory of Weak Interaction.", Prog. Theor. Phys. **49** (1973) 652.

[9] N. Cabibbo, "Unitary Symmetry and Leptonic Decays.", Phys. Rev. Lett. **10** (1963) 531.

[10] The ALEPH Collaboration *et al.*, "Precision Electroweak Measurements on the Z Resonance.", Physics Reports **427** (2006) 257; **hep-ex/0509008v3**.

[11] F. Abe *et al.*, "Observation of Top Quark Production in $p\overline{p}$ Collisions with the Collider Detector at Fermilab .", Phys. Rev. Lett. **74** (1995) 2626.

[12] S. Abachi *et al.*, "Observation of the Top Quark.", Phys. Rev. Lett. **74** (1995) 2632.

[13] UA1 Collaboration, "Experimental observation of isolated large transverse energy electrons with associated missing energy at $\sqrt{s} = 540GeV$.", Phys. Lett.**122B** (1983) 403.

[14] P.W. Higgs, "Broken symmetries, massless particles and gauge fields.", Phys. Rev. Lett. **12** (1964) 132.
P.W. Higgs, "Spontaneous Symmetry Breakdown without Massless Bosons.", Phys. Rev. **145** (1966) 1156.

[15] LEP Higgs Working group, "Search for the Standard Model Higgs boson al LEP.", CERN-EP/2001-055 (2001).

[16] M. Spira, "QCD Effects in Higgs Physics.", CERN-TH/97-068, (1997).

[17] Asai S. *et al.*, "Prospect for the search of a standard model higgs boson in ATLAS using vector boson fusion.", SN-ATLAS-2003-024 (2003).

[18] S.P. Martin, "A supersymmetry primer.", **hep-ph/9709356**

[19] ATLAS Collaboration, "ATLAS Detector and Physics Performance Technical Design Report.", CERN/LHCC/99-15, CERN/LHCC/99-16 (1999).

[20] PYTHIA Web Page, http://www.thep.lu.se/∼torbjorn/Pythia.html

[21] NJETS Web Page, http://vircol.fnal.gov/MCdownload/njets.html

[22] W-M Yao *et al.*, J. Phys. G: Nucl. Part. Phys. **33** (2006) 518.

[23] S. George, "ATLAS B-physics - an overview.", Nucl. Instr. and Meth. A**446** (2000) 274.

[24] D. Barberis, "ATLAS Inner Detector Developments.", Nucl. Instr. and Meth. A**446** (2000) 331.

[25] I. Dunietz, "CP violation with self-tagging B_d modes.", Phys. Lett. B**270** (1991) 75.

[26] M. Smizanska, "ATLAS: helicity analyses in beauty hadron decays.", Nucl. Instr. and Meth. **446** (2000) 138.

[27] The LHC Study Group, "The Large Hadron Collider Conceptual Design.", CERN/AC/95-05 (1995).

[28] EAGLE (Experiment for Accurate Gamma, Lepton and Energy Measurements) Collaboration, "A Toroidal LHC ApparatuS, ATLAS.", CERN-ARCH-ATLAS-001 (1992).

[29] ATLAS Collaboration, "ATLAS: letter of intent for a general-purpose *pp* experiment at the large hadron collider at CERN.", CERN/LHCC/92-4; LHCC-I-2 (1992).

[30] ATLAS Collaboration, "Technical Proposal.", CERN/LHCC/94-43 (1994).

[31] ATLAS Collaboration, "ATLAS calorimeter performance: Technical Design Report.", ATLAS-TDR-001; CERN-LHCC-96-040 (1996)

[32] ATLAS Collaboration, *ATLAS tile calorimeter: Technical Design Report*, ATLAS-TDR-003; CERN-LHCC-96-042, CERN, Geneva (1996).

[33] ATLAS Collaboration, *ATLAS liquid-argon calorimeter: Technical Design Report*, ATLAS-TDR-002; CERN-LHCC-96-041, CERN, Geneva (1996).

[34] ATLAS Collaboration, "Inner Detector Technical Design Repor.", CERN/LHCC/97-16; CERN/LHCC/97-17 (1997).

[35] ATLAS Collaboration, "ATLAS Muon Spectrometer Technical Design Report.", CERN/LHCC/97-22 (1997).

[36] ATLAS Collaboration, "ATLAS magnet system: Technical Design Report.", ATLAS-TDR-006; CERN-LHCC-97-018 (1997).

[37] ATLAS Collaboration, "ATLAS barrel toroid: Technical Design Report.", ATLAS-TDR-007; CERN-LHCC-97-019 (1997).

[38] ATLAS Collaboration, "ATLAS end-cap toroids: Technical Design Report.", ATLAS-TDR-008; CERN-LHCC-97-020 (1997).

[39] ATLAS Collaboration, "ATLAS central solenoid : Technical Design Report.", ATLAS-TDR-009 ; CERN-LHCC-97-021 (1997).

[40] ATLAS Collaboration, "ATLAS level-1 trigger: Technical Design Report.", ATLAS-TDR-012; CERN-LHCC-98-014 (1998).

[41] ATLAS Collaboration, "ATLAS pixel detector: Technical Design Report.", ATLAS-TDR-011; CERN-LHCC-98-013, (1998).

[42] ATLAS Collaboration, "ATLAS high-level trigger, data-acquisition and controls: Technical Design Report.", ATLAS-TDR-016; CERN-LHCC-2003-022 (2003).

[43] ATLAS Collaboration, "ATLAS computing: Technical Design Report.", ATLAS-TDR-017; CERN-LHCC-2005-022 (2005).

[44] S. W. Snow, "The case for equipping the Inner Detector with some NMR probes.", ATL-INDET-2000-010 (2000).

[45] A. Yamamoto *et al.*, "The ATLAS Central Solenoid.", Nucl. Inst. Meth. A*584* (2008) 53.

[46] S. Mizumura *et al.*, "Fabrication and Mechanical Performance of the ATLAS Central Solenoid.", IEEE Tr. Appl. Superconductivity **12** (2002) 416.

[47] R. Ruber *et al.*, "Quench Characteristics of the ATLAS Central Solenoid.", IEEE Tr. Appl. Superconductivity **16** (2006) 533.

[48] R.Ruber, "Ultimate performance of the ATLAS Superconducting Solenoid.", IEEE Tr. Appl. Superconductivity **17** (2007) 1201.

[49] P. Vedrine *et al.*, "Manufacturing and integration progress of the ATLAS barrel toroid magnet at CERN.", IEEE Tr. Appl. Superconductivity **14**(2) (2004) 491-494.

[50] J. M. Rey *et al.*, "Cold mass integration of the ATLAS Barrel Toroid Magnets at CERN.", IEEE Tr. Appl. Superconductivity **16** (2006) 553.

[51] P. Miele *et al.*, "The ATLAS magnet test facility at CERN.", IEEE Tr. Appl. Superconductivity **11** (2000) 1713.

[52] A. Dudarev *et al.*, "First full-size ATLAS barrel toroid coil successfully tested up to 22 kA at 4 T.", IEEE Tr. Appl. Superconductivity **15**(2) (2005) 1271-1275.

[53] A. Foussat et al., "Assembly Concept and Technology of the ATLAS Barrel Toroid.", IEEE Tr. Appl. Superconductivity **16** (2006) 565.

[54] D. E. Baynham et al., "Engineering Status of the End Cap Toroid Magnets for the ATLAS Experiment.", IEEE Tr. Appl. Superconductivity **10** (2000) 357.

[55] D. E. Baynham et al., "ATLAS End Cap Toroid Cold Mass and Cryostat Integration.", IEEE Tr. Appl. Superconductivity **16** (2006) 537.

[56] D. E. Baynham et al., "ATLAS End Cap Toroid Integration and Test.", IEEE Tr. Appl. Superconductivity **17** (2007) 1197.

[57] V.L.Ginzburg und I.M.Frank, JETP **16** (1946) 15.

[58] M. Aharrouche et al., "Response Uniformity of the ATLAS liquid argon electromagnetic calorimeter.", NIM **582** (2007) 429-455.

[59] M. J. Woudstra, "Precision of the ATLAS muon spectrometer.", CERN-THESIS-2003-015 (2002).

[60] P. Giusti *et al.*, "RPC construction paper.", Nucl. Inst. Meth. A**888** (2007)

[61] G. Aielli *et al.*, "SF-6 quenched gas mixtures for streamer mode operation of RPCs at very low voltages.", Nucl. Inst. Meth. A**493** (2002) 137-145.

[62] G. Aielli *et al.*, "Electrical conduction properties of phenolic-melaminic laminates.", Nucl. Inst. Meth. A**533** (2004) 86-92.

[63] G. Aielli *et al.*, "A high-voltage test for the ATLAS RPC qualification.", Nucl. Inst. Meth. A**533** (2004) 199-202.

[64] The PESA Software Group (editor Markus Elsing), "Analysis and Conceptual Design of the HLT Selection Software.", ATLAS-TDAQ-2002-004 (2004).

[65] PESA Software Group (editor Simon George), "PESA High-Level Trigger Selection Software Requirements.", ATLAS-TDAQ-2001-005 (2001).

[66] Core Algorithms Group (editor Steve Armstrong), "Algorithms for the ATLAS High Level Trigger.", ATLAS-DAQ-2003-002 (2003).

[67] D. Adams *et al.*, "Track Reconstruction in the ATLAS Muon Spectrometer with MOORE.", ATL-SOFT-2003-007 (2003).

[68] T. Lagouri *et al.*, "A Muon Identification and Combined Reconstuction Procedure for the ATLAS detector at CERN LHC.", IEEE Trans. Nucl. Sci., **51** (2004) 3030-3033.

[69] ATLAS Collaboration, "ATLAS Detector and Physics Performance Technical Design Report." CERN/LHCC99-14/15 (1999).

[70] M.Smizanska *et al.*, "ATLAS: B Physics Reach." Eur. Phys. J., C **34** (2004) s385-s392.

[71] E. Gshwendtner *et al.*, "Benchmarking the Particle Background in the LHC Experiments.", CERN-THESIS-2002-001 (2000).

[72] V. Bocci *et al.*, "The Coincidence Matrix ASIC of the Level-1 Muon Barrel Trigger of the ATLAS Experiment.", IEEE Transactions on Nuclear Science, August 2003 Issue vol. 50, no. 4

[73] G.Cataldi *et al.*, "Muon identification with the event filter of the ATLAS experiment at CERN LHC.", IEEE Trans. Nucl. Sci. **53** (2006) 870-875.

[74] V. Boisvert *et al.*, "A New Implementation of the Region-of-Interest Strategy for the ATLAS Second Level Trigger.", ATL-DAQ-2003-034 (2003).

[75] D. Adams *et al.*, "MOORE as Event Filter in the ATLAS High Level Trigger.", ATL-SOFT-2003-008 (2003).

[76] iPatRec Web Page, http://atlas.web.cern.ch/Atlas/GROUPS/INNER_DETECTOR/inner_detector.html

[77] R.Clifft, A. Poppleton, "IPATREC: inner detector pattern-recognition and track-fitting.", ATL-SOFT-94-009; ATO-PN-9 (1994).

[78] LHC Computing Grid Web Page, http://lcg.web.cern.ch/LCG

[79] P. Eerola, "The inclusive muon cross-section in ATLAS.", PHYS-NO-120 (1998).

[80] GEANT4 Web Page, http://geant4.web.cern.ch/geant4.

[81] S. Baranov *et al.*, "Estimation of Radiation Background, Impact on Detectors, Activation and Shielding Optimization in ATLAS.", ATL-GEN-2005-001 (2005).

[82] A. Nisati, "Fake Level-1 Muon Trigger Rates in the ATLAS experiment.", ATL-DAQ-98-123 (1998).

[83] T. Stapelberg *et al.*, "Measurement of the Inclusive Muon Production Cross Section.", $D\varnothing$ note 4325, 2004-01-20;
S. Abachi *et al.*, "Inclusive and b-Quark Production CrossSections in $p\overline{p}$ Collisions at $\sqrt{s} = 1.8$ TeV.", Phys. Rev. Lett. **74** (1995) 3548.

[84] S. George *et al.*, "ATLAS Trigger Menus.", DAQ-NO-121; PHYS-NO-124 (1998).